[Doctoral thesis] Catalytic micro-device for methane combustion: a study on kinetics and fluid-dynamic

Original Citation:
F. Conti (2012). *Catalytic micro-device for methane combustion: a study on kinetics and fluid-dynamic.* PhD thesis

Availability:
This version is available at : `http://porto.polito.it/2588771/` since: February 2015

Published version:
DOI:10.6092/polito/porto/2588771

Politecnico di Torino: Scuola di dottorato XXIII ciclo

Catalytic micro-device for methane combustion: a study on kinetics and fluid-dynamic.

Candidato: Ing. Conti Fabio

Relatori : Prof. Specchia Vito,
Prof. Specchia Stefania
Controrelatore: PhD. Francesco Greco*

**Dottore in Fisica, PhD in Ingegneria Chimica; primo ricercatore CNR presso l'Istituto di Ricerche sulla Combustione (IRC) di Napoli.*

Index of contents

1. Introduction

The thesis here presented links various phases of the research and development starting from a real issue, describing briefly how that problem is usually solved and stressing on the weaknesses of the available technologies which are the new issues the scientific and technological progress have to solve.

In this case the thesis is focused on the generation of power in small scale system where a heat source is used to produce a low temperature utility (i.e. house heating).

At present the chemical energy stored in hydrocarbons is degraded to 60°C hot water and therefore the interposition of a top cycle in between combustion and the low temperature utility makes great sense.

Standard technologies such as internal or external combustion reciprocating engines are discussed stressing on the weight and on the complexity that affects all this kind of engines and requires a specific maintenance that end consumer isn't willing to deal with.

A very promising alternative technology is the one of thermoelectric cells which however are still in an early stage of development and need researching efforts to gain an efficiency comparable to a Stirling engine.

For these reasons the introductory part of this thesis describes the system outline of a thermoelectric generator and then exposes a short review about thermoelectric materials: at present the materials with the best efficiency cannot withstand to very high temperatures and so it arises the need to perform a catalytic oxidation of methane to keep the combustion temperature under 300°C.

In this thesis are reported the data about the screening, by means of temperature programmed combustion, of some catalysts that proved to be good candidates to oxidize methane at low temperature and, in order to get fundamental kinetics of methane oxidation, the catalysts were further tested in a high recirculation differential reactor.

Unfortunately both ceria–zirconia oxide and lanthanum manganite catalyst needed noble metal doping to reach a safely low combustion temperature that preserved the thermoelectric material.

The second part of this thesis focuses on the implementation of the kinetic mechanism of methane combustion in a sample monolith catalyzed with $Pd/Ce_{0,33}$-$Zr_{0,66}O_2$; the modelling was performed using Fluent© fluid dynamics code coupled with a user defined function to model a mars van Krevelen kinetics; the preliminary study was aimed firstly at numerical stability and then at assessing the impact of inlets and outlets zones on fluid dynamics (since they are relatively heavy to compute).

Finally this PhD thesis presents the results of a 3Dimentional model, which takes into account also the irradiative effects happening between insulator surface and furnace walls to better model thermal phenomena.

2. State of the art in heat recovery

The use of waste heat to produce electric energy is an interesting field of research because extra electric power can be harvested without having to burn more fuel; a possible application could be the production of auxiliary power from car exhaust which can recover part of the energy consumed by its electronic devices.

In a similar way a combined-heat-and-power system based on a burner coupled with a heat recovery system can produce some power while providing low enthalpy heat for a household.

The realization of such a system having small scale system in mind can be done using two technologies: Stirling engines which is a traditional approach based on the use of air as a working fluid and thermoelectric generators which converts thermal energy directly into electrical power without using moving parts.

For completeness the concepts and the schemes of Stirling engines are herein described

2.1. The Stirling engine as a heat recovery system.

Stirling engines are a very effective way to produce mechanical energy from temperature difference; originally conceived in 1816 as an industrial prime mover to rival the steam engines, their practical use was largely confined to low-power domestic applications for over a century.

These engines are currently exciting interest as the core component of micro-combined heat and power (CHP) units, in which they're more efficient and safer than a comparable steam engine.

Stirling engine is an external combustion device and because of this, its bearings and pistons are not placed in a very harsh environment.

For this reason Stirling engines are more reliable and require less maintenance than internal combustion engine.

The concept of separating heat production from the production of mechanical power allows the use of high efficiency- low pollution combustors such as fibrous burners that further increase the eco-compatibility of the system.

The so called ideal Stirling cycle consists of four phases:

1. Isochoric heating
2. Isothermal expansion (at Tmax)
3. isochoric cooling
4. isothermal cooling (at Tmin)

However it is widely known that real Stirling engines differ strongly from their ideal counterpart so both Clapeyron diagrams are reported (Figure 1 and 2)

Figure 3 illustrates the three basic configuration of Stirling engine: alfa, beta and gamma; a brief description of how they work is described below.

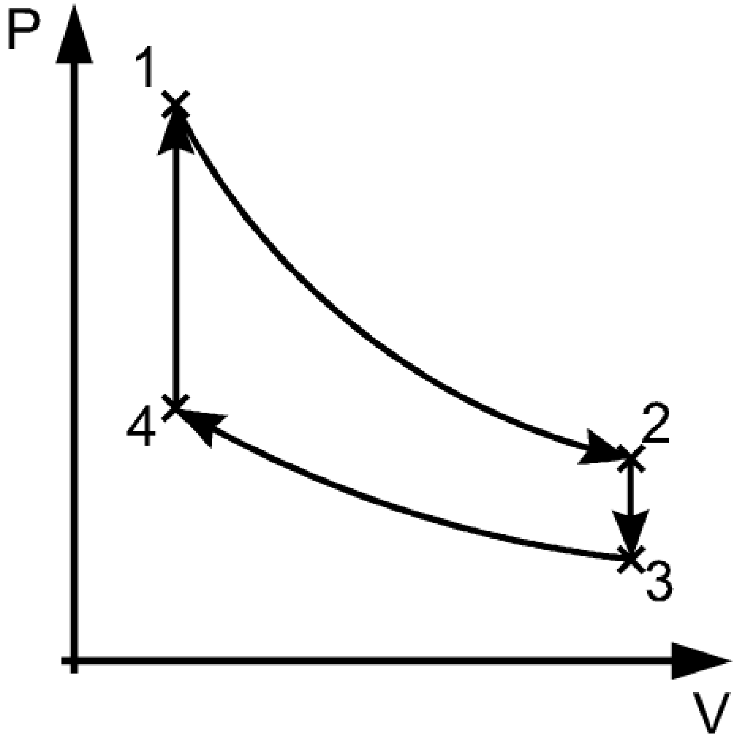

Figure 1: Diagram of Clapeyron of the ideal Stirling cycle

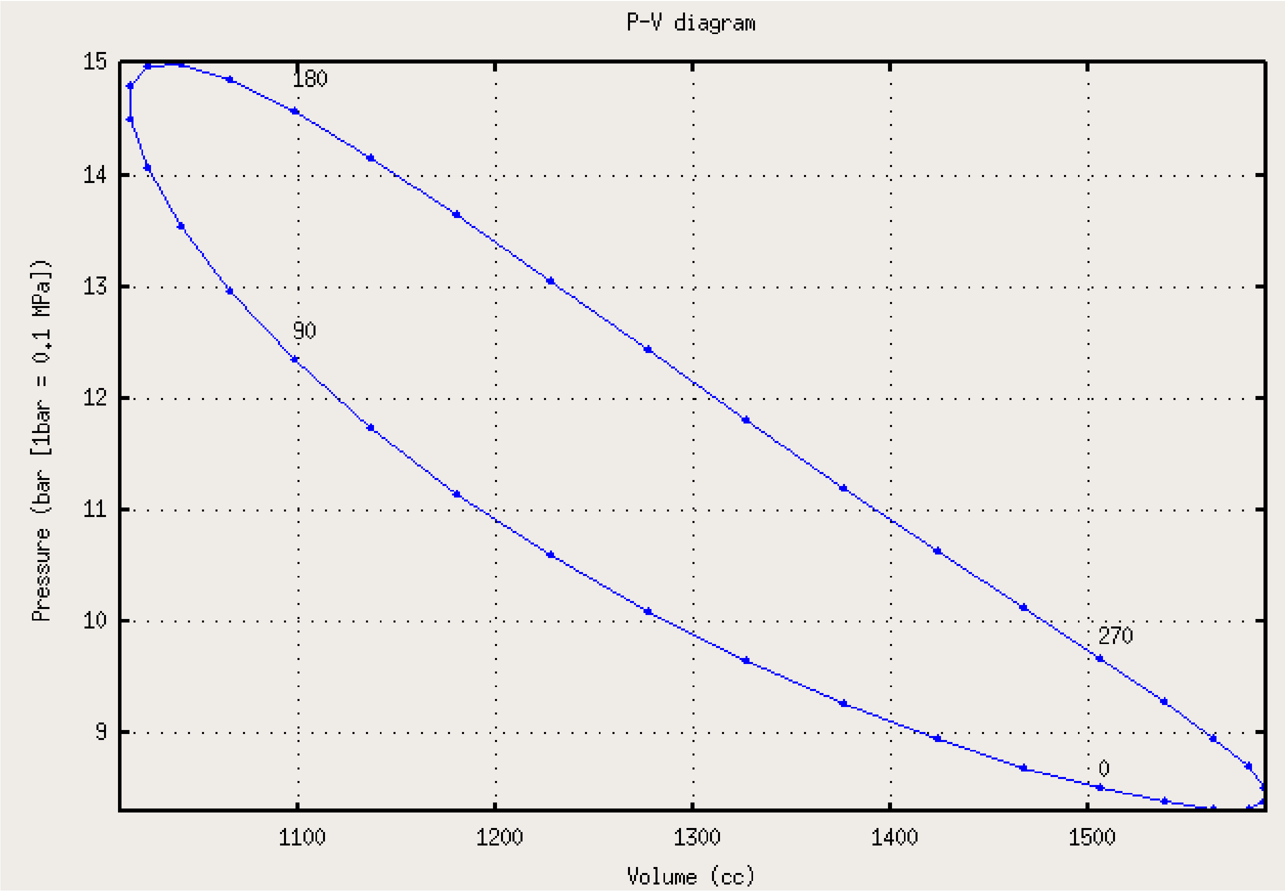

Figure 2: A Clapeyron diagram of a real Stirling engine

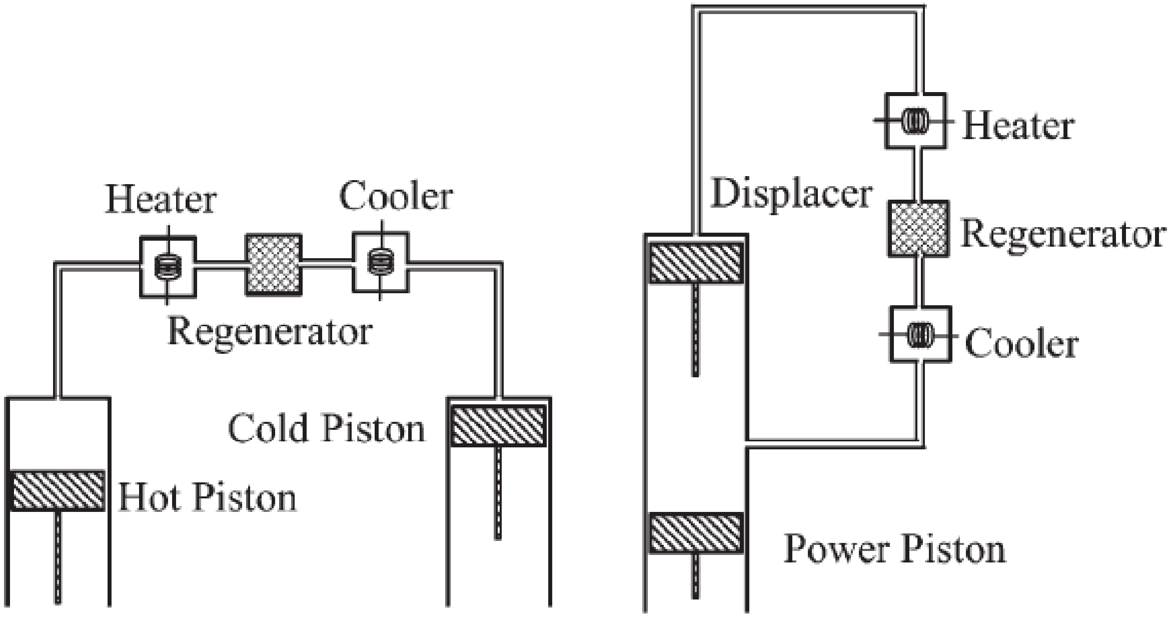

The Alpha-Configuration The Beta-Configuration

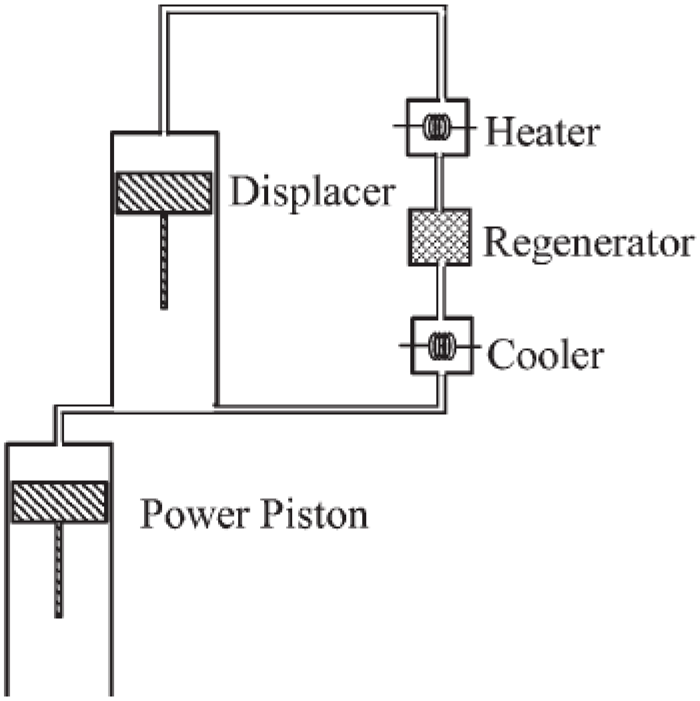

The Gamma-Configuration

Figure 3: Possible configuration of Stirling cycles

Alpha Stirling engine

Alpha Stirling engine is the configuration whose functioning is the easiest to understand: it contains two power pistons in separate cylinders, one hot and one cold.

The hot cylinder is situated inside the high temperature heat exchanger and the cold cylinder is situated inside the low temperature heat exchanger; often the two cylinders are configured in a 90° V shape .

Between the hot and cold heat exchangers a heat regenerator is often placed whose primary effect is to increase the thermal efficiency of the engine greatly by 'recycling' internal heat which would otherwise pass through the working fluid irreversibly.

This type of engine has a high power-to-volume ratio but has technical problems due to the usually high temperature of the hot piston and the durability of its seals [1].

In practice, this piston usually carries a large insulating head to move the seals away from the hot zone at the expense of some additional dead space.

Beta and gamma Stirling engine

With beta Stirling engine more compact designs are possible because a single power piston is present while within the same cylinder a displacer piston is moving. The displacer piston is a loose fit and does not extract any power from the expanding gas but only serves to shuttle the working gas from the hot heat exchanger to the cold heat exchanger.

When the working gas is pushed to the hot end of the cylinder it expands and pushes the power piston while when it is pushed to the cold end of the cylinder it contracts and the momentum of the machine, usually enhanced by a flywheel, pushes the power piston the other way to compress the gas.

Unlike the alpha type, the beta type avoids the technical problems of hot moving seals because only the cold end needs a sealing ring.

Many beta Stirling engines are simplified designs avoiding regenerator and external gas circuit.

Gamma Stirling engines are a derivation of the beta concept and they differ from it in the fact that they don’t feature the displacer and the power piston on the same axis.

2.2. Drawbacks of using Stirling engines

- Stirling engine designs require heat exchangers for heat input and for heat output, and these must contain the pressure of the working fluid, where the pressure is proportional to the engine power output. In addition, the expansion-side heat exchanger is often at very high temperature, so the materials must resist the corrosive effects of the heat source, and have low creep.

  Typically these material requirements substantially increase the cost of the engine. The materials and assembly costs for a high temperature heat exchanger typically accounts for 40% of the total engine cost [2].
- All thermodynamic cycles require large temperature differentials for efficient operation so, in an external combustion engine, the heater temperature always equals or exceeds the expansion temperature meaning that the metallurgical requirements for the heater material are very demanding.

  This issue is similar to the one encountered in a Gas turbine; on the other hand with an Otto or a Diesel engine, the expansion gas temperature can far exceed the metallurgical limit of the employed alloys because heat is generated inside the cylinder and peak temperature lasts for a fraction of a second, so internal combustion. engine materials operate closer to the average temperature of the working gas.

- A Stirling engine cannot start instantly but it needs a warm up period; it should be used as constant power because it is difficult to modify engine load.

3. Generation of energy without the intervention of mechanical parts: the Seebeck effect

The principal advantage of the employment of this innovative technique is that during electricity generation, no moving part is involved; another key factor is that the use of a thermoelectric generator allows to eliminate the need of a motor fluid so hot-side and cold side heat exchangers can be easily integrated by the two sides of the thermoelectric device

In addition to this benefit the Seebeck energy generator has no moving part so it can keep on working for very long times without losing performances, because the energy is supplied externally along with energy production.

J. Fairbanks published a detailed work explaining the potential application of thermoelectric materials in HP cogeneration and in solar thermal energy generation [3]

However to obtain satisfactory efficiencies pairs of materials constituting the thermoelectric device must be chosen carefully: the primary criterion for thermoelectric device viability is the figure of merit given by formula 1:

$$Z = \sigma \frac{S^2}{\kappa} \qquad (1)$$

which depends on the Seebeck coefficient, S, thermal conductivity, κ, and electrical conductivity, σ. Often the product (ZT) of Z and the use temperature, T, serves as a dimensionless parameter to evaluate the performance of a thermoelectric material.

Notably, in equation 1, thermal conductivity and electrical conductivity are typically intertwined being low thermal conductivity and high electrical conductivity wishable to obtain a high efficiency material.

Phonon-Glass, electron-crystal (PGEC) theory developed by G. A. Slack [4] proposes that in order to optimize the figure of merit, phonons which are responsible for thermal conductivity must experience the material as they would in a glass (experiencing a high degree of phonon scattering--lowering the thermal conductivity) while electrons must experience it as a crystal (experiencing very little scattering--maintaining the electrical conductivity).

A more detailed article concerning the parameters influencing the figure of merit and how can be improved is the one by Timothy Sands [5].

The efficiency of a thermoelectric device for electricity generation is given by η, defined as

$$\eta = \frac{\text{energy provided to the load}}{\text{heat energy absorbed at hot junction}} \qquad (2)$$

The maximum efficiency of a thermoelectric material is

$$\eta_{max} = \frac{T_H - T_C}{T_H} \frac{\sqrt{1 + Z\bar{T}} - 1}{\sqrt{1 + Z\bar{T}} + \frac{T_C}{T_H}} \qquad (3)$$

where T_H is the temperature at the hot junction and T_C is the temperature at the surface being cooled. $Z\bar{T}$ is the modified dimensionless figure of merit which now takes into consideration the thermoelectric capacity of both thermoelectric materials being used in the power generating device, and is defined as

$$Z\bar{T} = \frac{(S_p - S_n)^2\bar{T}}{[(\rho_n\kappa_n)^{1/2} + (\rho_p\kappa_p)^{1/2}]^2} \tag{4}$$

where ρ is the electrical resistivity, $\bar{T}$ is the average temperature between the hot and cold surfaces, κ is the thermal conductivity and the subscripts n and p denote properties related to the n- and p-type semiconducting thermoelectric materials, respectively.

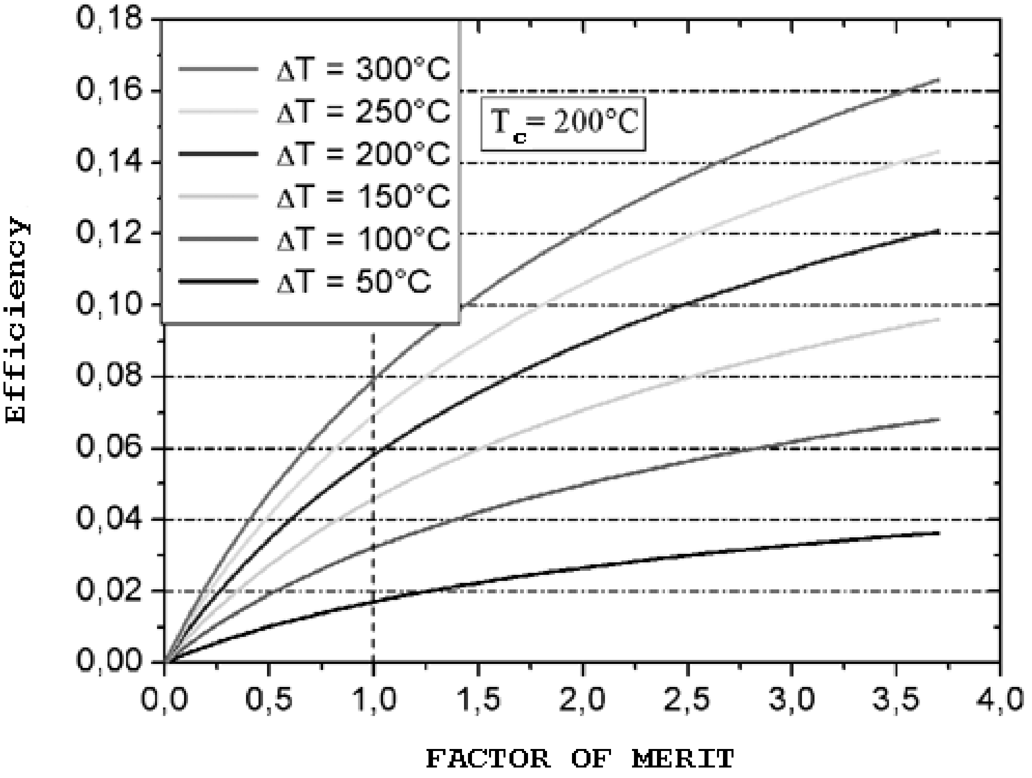

Figure 4: Thermodynamic efficiency of a thermoelectric device vs factor of merit at various difference of temperature (T_c is cold side temperature).

It is worthwhile to note that the efficiency of a thermoelectric device is limited by the Carnot efficiency (hence the T_H and T_C terms in η_{max}), since thermoelectric devices are still inherently heat engines.

As a consequence it can be easily demonstrated that if the ZT factor tends toward positive infinity then the efficiency of the thermoelectric device can reach the Carnot limit: however no material has been reported to feature a $Z\bar{T}$ higher than 3 [6].

3.1. Materials of interest

Strategies to improve thermoelectric materials performance include both advanced bulk materials and the use of low-dimensional systems. Such approaches to reduce lattice thermal conductivity fall under three general material types:

1. Alloys: create point defects, vacancies, or rattling structures (heavy-ion species with large vibrational amplitudes contained within partially filled structural sites) to scatter phonons within the unit cell crystal [7]
2. Complex crystals: separate the phonon-glass from the electron crystal using approaches similar to those for superconductors. The region responsible for electron transport would be

an electron-crystal of a high-mobility semiconductor, while the phonon-glass would be ideal to house disordered structures and dopants without disrupting the electron-crystal (analogous to the charge-reservoir in high-T_C superconductors [8]).

3. Multiphase nanocomposites: scatter phonons at the interfaces of nanostructured materials [9]. Research showed that both mixed composites or thin-film superlattices are good thermoelectric materials.

There are a number of materials being researched for thermoelectric device applications and temperature ranges. Some such materials include:

Bismuth chalcogenides

These materials involve Bi_2Te_3 and Bi_2Se_3 and comprise some of the best performing TE at room temperature with a temperature-independent figure of merit, ZT, between 0.8 and 1.0 [10].

Nanostructuring [11] of these materials to produce a layered superlattice structure of alternating Bi_2Te_3 and Bi_2Se_3 layers produces a device within which there is good electrical conductivity but perpendicular to which thermal conductivity is poor. The result is an enhanced ZT (approximately 2.4 at room temperature for p-type) [12] Note that this high value has not entirely been independently confirmed.

Skutterudite TE materials

Recently, skutterudite materials have sparked the interest of researchers in search of new TE [13] These structures are of the form $(Co,Ni,Fe)(P,Sb,As)_3$ and are cubic with space group Im3. Undoped, these materials contain voids into which low-coordination ions (usually rare earth elements) can be inserted in order to alter thermal conductivity by producing sources for lattice phonon scattering and decrease thermal conductivity due to the lattice without reducing electrical conductivity [14]. Such qualities make these materials behave with PGEC behavior [4].

Oxide TE

Due to the natural superlattice formed by the layered structure in homologous compounds (such as those of the form $(SrTiO_3)_n(SrO)_m$--the Ruddleson-Popper phase), oxides are also being considered for high-temperature thermoelectric devices [15]. These materials exhibit low thermal conductivity perpendicular to these layers while maintaining electrical conductivity within the layers. The figure of merit in oxides is still relatively low (~0.34 at 1000 K) [16], but the enhanced thermal stability, as compared to conventional high-ZT bismuth compounds, makes the oxides superior in high-temperature applications [17]

Nanomaterials

In addition to the nanostructured Bi_2Te_3/Bi_2Se_3 superlattice thin films that have shown a great deal of promise, other nanomaterials have also shown potential in improving TE materials. One example involving PbTe/PbSeTe quantum dot superlattices was shown to provide an enhanced ZT (approximately 1.5 at room temperature) that was a great deal higher than the bulk ZT value for either PbTe or PbSeTe (approximately 0.5) [10].

More recently, two research groups have shown that individual silicon nanowires can act as efficient TE materials. Each group found ZT values approaching 1.0 for their structures, even though bulk silicon is known to be a poor thermoelectric material (its factor of merit is approximately 0.01 at room temperature) because of its high thermal conductivity [18, 19].

As said before, the Seebeck cell has a major drawback in his low efficiency but this is compensated by the fact that also carrying electric energy for long distances implies significant grid losses; if also the improvements of the factor of merit that the nanotechnologies have granted to this are taken into account, then it makes sense to carry out research about the energy generation based on the Seebeck effect.

Articles cited in the introductive chapters

1) M.Keveney(2000)a
2) C.M. Hargreaves (1991) *The Philips Stirling engine* Elsevier
3) Tritt et al., "Thermoelectrics: Direct Solar Thermal Energy Conversion," MRS Bulletin: April 2008, Vol. 33, pp. 366-8 5
4) Slack GA., CRC Handbook of Thermoelectrics, ed. DM Rowe, Boca Raton, FL: CRC Press (1995)
5) Tritt, T. M.; Subramanian, M. A., Thermoelectric Materials, Phenomena, and Applications: A Bird's Eye View. MRS Bulletin 2006, 31, (3), 188-194.
6) Timothy D. Sands (2005), "Designing Nanocomposite Thermoelectric Materials," http://nanohub.org/resources/383.
7) Bhandari, C. M. in CRC Handbook of Thermoelectrics (ed. Rowe, D. M.) 55–65 (CRC, Boca Raton, 1995).
8) Cava, R. J. Structural chemistry and the local charge picture of copper-oxide superconductors. Science 247, 656–662 (1990).
9) Dresselhaus, M. S. et al. New directions for low-dimensional thermoelectric materials. Adv. Mater. 19, 1043–1053 (2007).
10) D.Y. Chung et al., Complex Bismuth Chalcogenides as Thermoelectrics, 16th International Conference on Thermoelectrics (1997), pp. 459-462
11) Harman, T. C.; Taylor, P. J.; Walsh, M. P.; LaForge, B. E., Quantum dot superlattice thermoelectric materials and devices. Science 2002, 297, (5590), 2229-2232.
12) Venkatasubramanian et al., Nature, 413, 597 (2001)
13) Caillat, T., Borshchevsky, A., and Fleurial, J.-P., In Proceedings of 7th International Conference TEs, K. Rao, ed., pp. 98 – 101. University of Texas, Arlington, 1993.
14) Nolas et al., J. Appl. Phys ., 79 (1996), 4002-8
15) K. Koumoto,I. Terasaki, T. Kajitani, M. Ohtaki, R. Funahashi “Oxide Thermoelectrics”; Section 35: pp.1-14 in Thermoelectrics Handbook: Macro to Nano, Edited by D.M. Rowe, CRC Press: New York (2006).
16) W. Wunderlich, S. Ohta, and K. Koumoto, 24th International Conference on Thermoelectrics, 2005, pp. 252-255
17) M. Senthilkumar et al. "High-temperature resistivity and thermoelectric properties of coupled substituted Ca3Co2O6" Sci. Technol. Adv. Mater. 10 (2009) 015007
18) Hochbaum, A. I. et al. Enhanced thermoelectric performance of rough silicon nanowires. Nature 451, 163–167 (2008).
19) A.I. Boukai et al. "Silicon nanowires as efficient thermoelectric materials" Nature 451 (2007) 168-171

Index of symbols used in the introductive chapters

S =Seebeck coefficient V/K
Z= factor of merit K^{-1}

ZT= adimensional factor of merit
ρ =electrical resistivity ($\Omega\cdot$m)
σ = electrical conductivity ($\Omega\cdot$m)$^{-1}$
κ = thermal conductivity W$\cdot$m$^{-1}\cdot$K^{-1}
T_C,T_H, ΔT = cold side, hot side, and difference of temperature respectively (K)

4 The Micro combustor design

The micro combustor consists in a small flat honeycomb monolith in which fuel burns generating heat that is collected by the same monolith, which is built in a highly conductive material such as SiC, and transferred to the thermoelectric generator for energy production.

The cell we are testing requires an input power of about 25 watts thermal; unfortunately it also has an operative temperature limitation of 300 °C so it is unfeasible to expose it to a free flame without damaging it irreversibly.

The solution to this problem was found in catalysis: if fuel could be oxidized at low temperature but near 300 °C then the heat produced could be easily used for direct electricity generation.

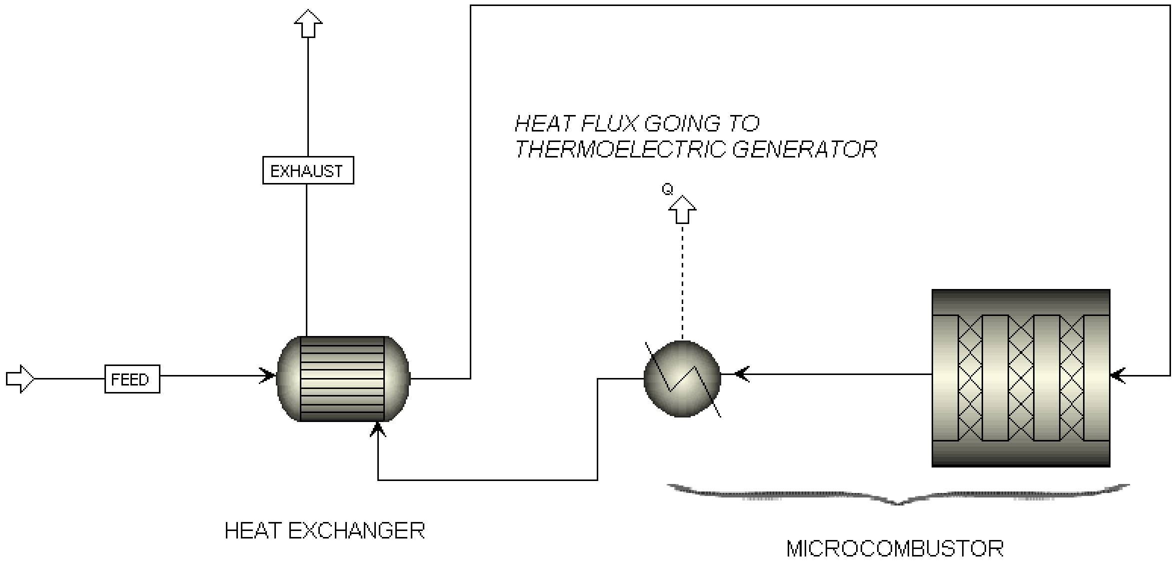

Figure 5: Flow diagram of a micro combustor

Figure 5 shows the modellistic concept behind the energy generator device: gas mixture is fed to pre-heater before it enters in the combustion zone, the mixture burns inside a catalytic micro-combustor which is physically coupled with two TE generators that harvest the heat produced and finally exhaust gases are sent back to the heat recovery system.

Further developments increased the integration of the various components as showed in Figures 6 and 7.

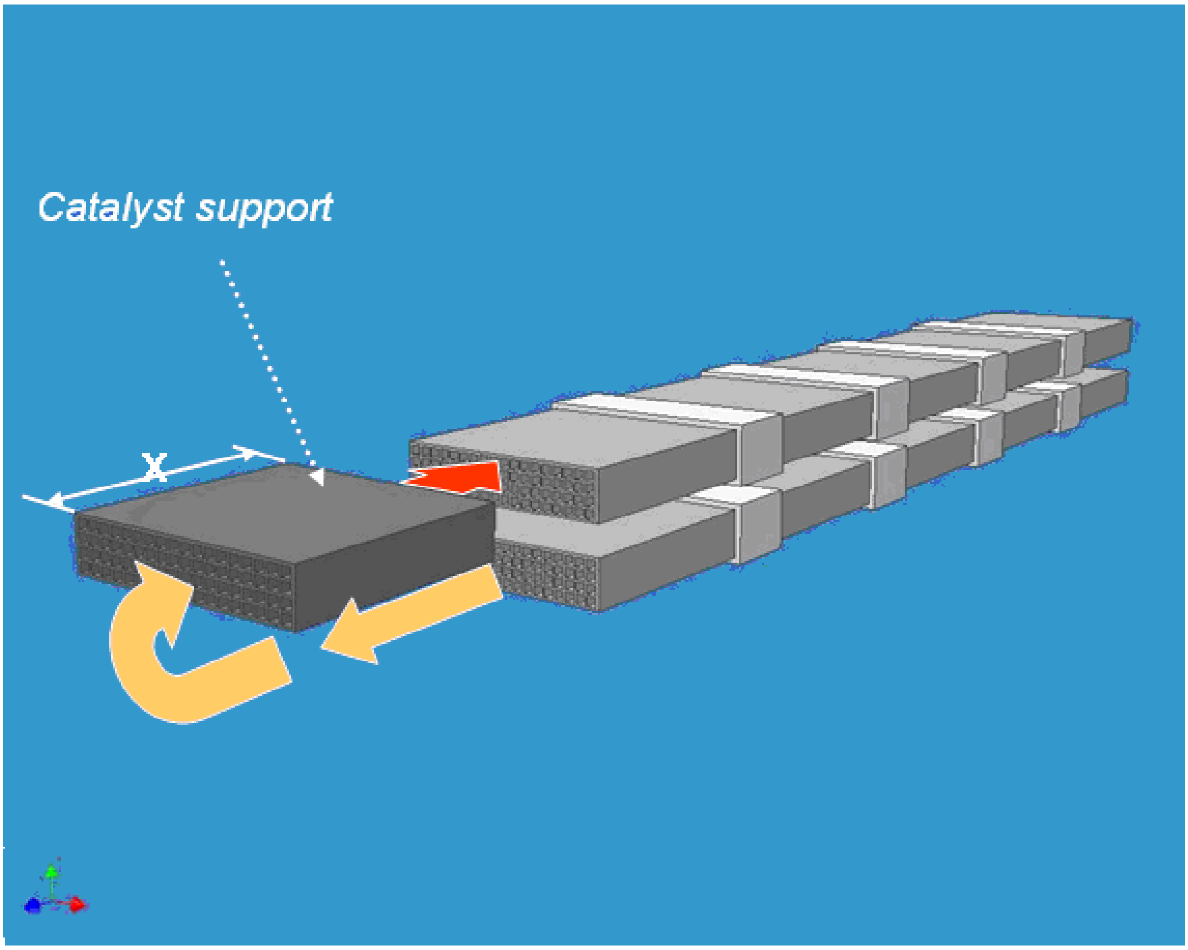

CRF Orbassano (TO)

Figure 6: Scheme for the micro combustor preheater

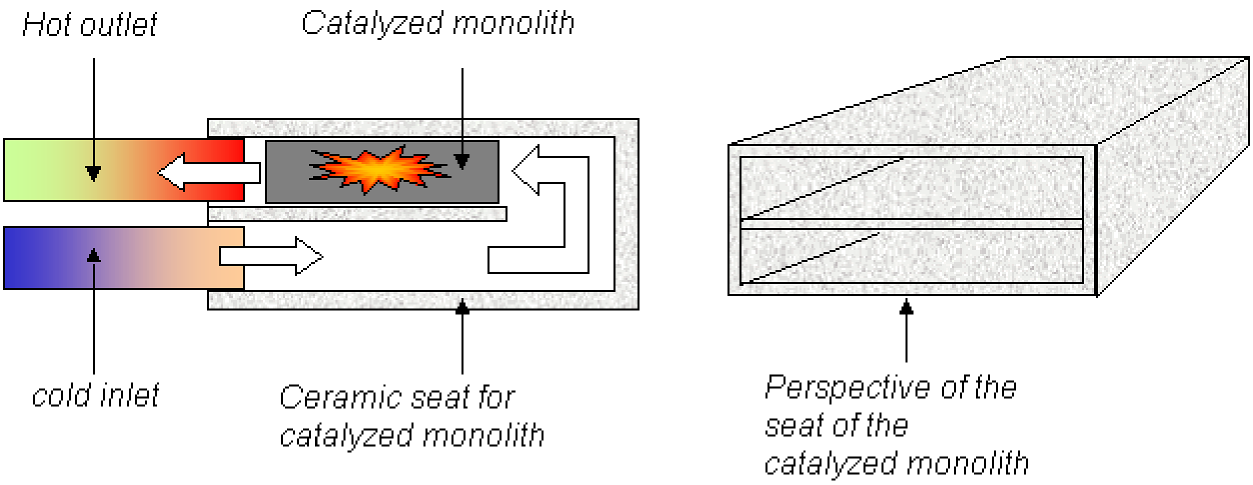

Figure 7: Scheme of the gas flow entering the micro combustor

Typical gas flow of the micro combustor burned gas is 800 Nml/min and its composition doesn't exceed the 5% molar of methane in air.

It is self evident that the activity of system must be very high in order to burn fuel smoothly without leaving residual carbon monoxide to leak outside: during combustion the following 3 steps take place:

- Reagent diffusion to the catalyst.
- Reaction on catalyst surface.
- Product back-diffusion to the gas flow.

It is not yet known which resistance could be the most important rate limiting phenomenon but all of them must work well in order to increase miniaturization.

Two lines of research are therefore important: one concerning the activity of the catalyst to obtain a lower light off temperature, while the other is related to monolith's fluid dynamics because a structured monolith has a the drawback of a limited reagent diffusion towards catalytic walls.

Decreasing channel width or shifting to a silicon carbide foam is very effective in increasing gas mixing and reagent diffusion at the cost of a significant pressure loss inside the micro combustor.

A Computational Fluid Dynamics simulation of a monolith has been developed in this thesis to optimize system design to know the right amount of catalyst to be placed and where catalyst deposition is more effective.

Before that, however, a detailed analysis of reaction kinetics has been performed to asses a feasible kinetic equation that has been implemented in the model.

5 Introduction to the materials tested

In recent years, catalytic combustion of CH_4 has been extensively studied as an alternative option to conventional thermal combustion [1,2] for the production of heat and energy in view of its capability to achieve effective combustion at much lower temperatures than in conventional oxidation processes.

Given the need to choose a very active catalyst a screening of catalysts yet known in literature was performed making a Temperature Programmed Combustion (TPC) of methane.

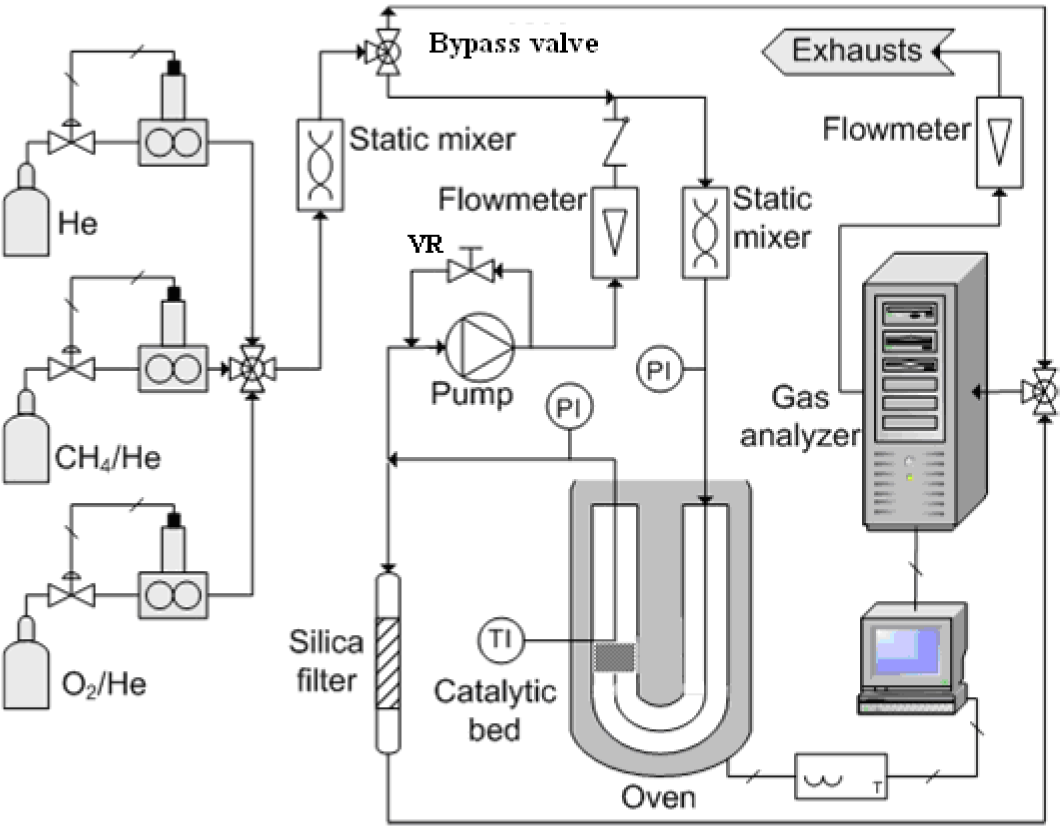

Figure 8: Full catalytic testing rig (pump is used to when a differential reactor is needed).

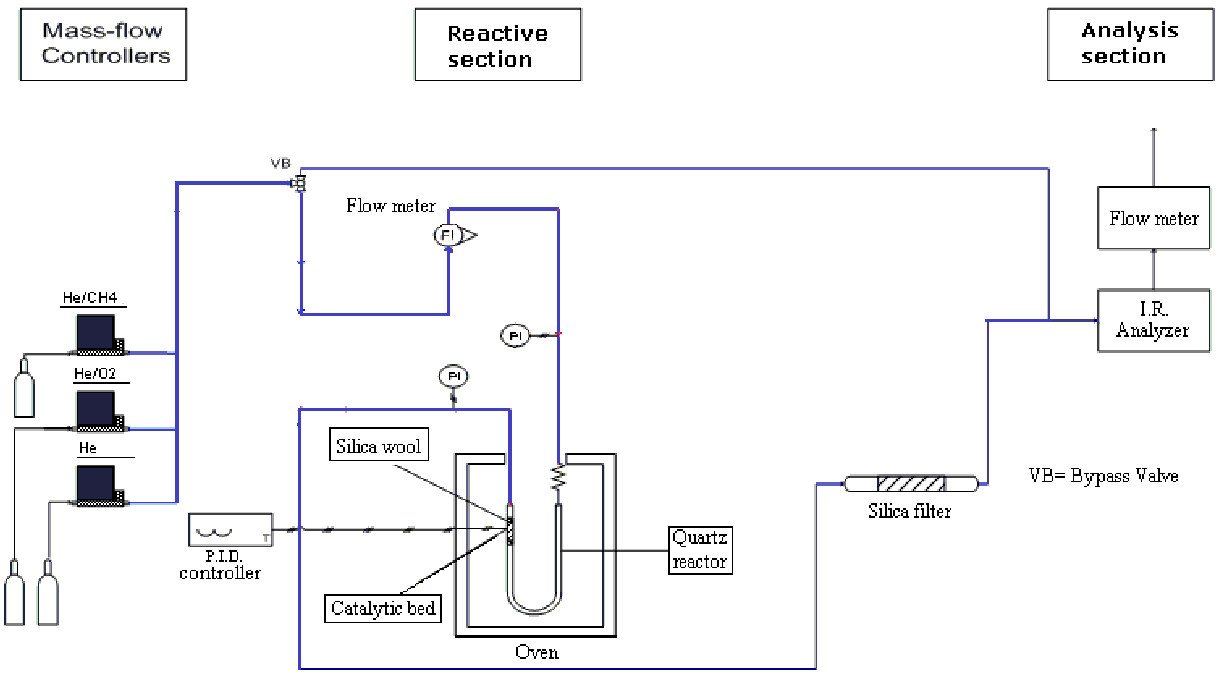

Figure 8 / bis: Flow scheme of the catalytic testing rig used for TPC

Figures 8 and 8bis shows the basic test rig that was used both for TPC and kinetic analysis: gases were first sent directly to the gas analyzer to register the gas inlet composition, after this the bypass valve VB was turned and the mixture passed once through the catalyst bed: during the tests performed to determine the TPC curve the recirculation pump was turned off and the valve VR was kept closed to get the gas flow through the catalytic bed.

In order to easily visualize the gas flow during the TPC analysis the scheme 8/bis is reported

On the other hand, kinetical analysis required high gas flow to abate mass transfer resistances and to make the catalytic bed to work as a differential reactor: so the pump was turned on and the backflow was regulated by valve V_R.

Furthermore, a silica filter was located between the reactor and the analyzer in order to remove water vapour formed during the combustion reaction.

The tested catalytic materials were:

- Nickel Chromate
- Ceria-zirconia solid solution oxide
- Lanthanum manganite perovskite

Each of these materials was tested as catalyst without any doping and with a 2% Pd addition: Palladium is a very active catalyst towards methane oxidation especially when is present in the oxidized state PdO_x

The catalysts were then characterized by XRD analysis (Philips PW1710 apparatus equipped with a monochromator for the CuKα radiation; markers located according the PcpdfWin database); the B.E.T. specific surface area was determined by N_2 adsorption at the liquid N_2 temperature (Micrometrics ASAP 2010 M); the samples were degassed in vacuum for at least 4 h at 250 °C before analysis.

The catalytic activity of the prepared catalysts towards CH_4 combustion was tested in a temperature programmed combustion (CH_4-TPC) device. The apparatus consisted of a fixed bed reactor inserted between quartz wool (i.d. 4 mm), made of 0.1 grams of catalyst (0.4-0.6 mm) and 0.9 of SiO_2 pellets (0.3-0.7 mm, Unaxis). The reactor, placed in a PID-regulated oven, was fed with 50 Nml min^{-1} of gas (2.5% CH_4; 15%, O_2; He to balance).

The SiO_2 pellets were used to increase the internal spacing between the catalyst powders and to reduce the pressure drop across the fixed bed.

The temperature was then increased up to 850 °C (using a heating ramp of 50 °C min^{-1}) until the CH_4 combustion was complete. When this condition was reached, the oven was allowed to cool naturally.

During the oven cooling, the reactor outlet gas concentration was measured every 10 °C of temperature decrease with a NDIR analyzer (Hartman and Braun URAS 10E) and recorded versus time by a computer.

Each test was repeated at least three times to verify the stability and repeatability of the measurements.

Plotting CH_4 conversion versus temperature, sigma-shaped curves were obtained and the half-conversion temperature (T50) was regarded as an index of the catalytic activity. The CH_4-TPC curve of a fixed bed composed of only 1.0 g of SiO_2 was evaluated to estimate the non-catalytic combustion of CH_4 in the reactor (blank test reported in Figure 9).

References for chapter 5

[1] Pfefferle, L. D.; Pfefferle, W. C. "*Catalysis in combustion*" .Catal. Rev. Sci. Eng. 1987, 29, 219.

[2] Zwinkels, M. F. M., Järås, S. G.; Menon, P. G.; Griffin, T. A. *"Catalytic materials for high-temperature combustion"* Catal. Rev. Sci. Eng. 1993, 35, 319.

6 Nickel chromate

The first material tested was nickel chromate whose activity towards methane was previously studied by the *CRE3* research team and the results of the experimentation where presented at [1]: activity of $NiCrO_4$could be explained combining the high affinity of nickel towards methane with the powerful oxidative properties of chromate ion.

Taking all the adequate precautions needed to manipulate this powder and its precursors, the catalyst was synthesized by solution combustion synthesis SCS of metal nitrates hydrates

Reagent name	**Formula**	**Quantity per gram of catalyst**
Nickel Nitrate	$Ni(NO_3)_2\_6H_2O$	**1,665 g**
Chromium Nitrate	$Cr(NO_3)_3\_9H_2O$	**2,291 g**
Palladium Nitrate	10% solution. H_2O	**0,433 g**
Urea	N_2H_4CO	**3,78 g**

Table 1: Reagents for 1gr of 2%Pd on nickel chromate

The synthesis method consisted in weighting all the reagents and dissolving them in the proper amount of water: then the solution is put in a capsule which in turn is placed in a furnace at 500°C for some minute. After the end of the simultaneous combustion synthesis step a further step of calcination was taken over at 800°C for two hours to remove any residual carbon.

When doped with Palladium, nickel chromate shows a significant activity with a half combustion temperature of 400 °C but this catalyst suffers from deactivation, sintering and sulphur poisoning: for this reason and because the materials involved in the preparation of this catalyst are considered carcinogen for humans it has been decided to end any research on nickel chromate.

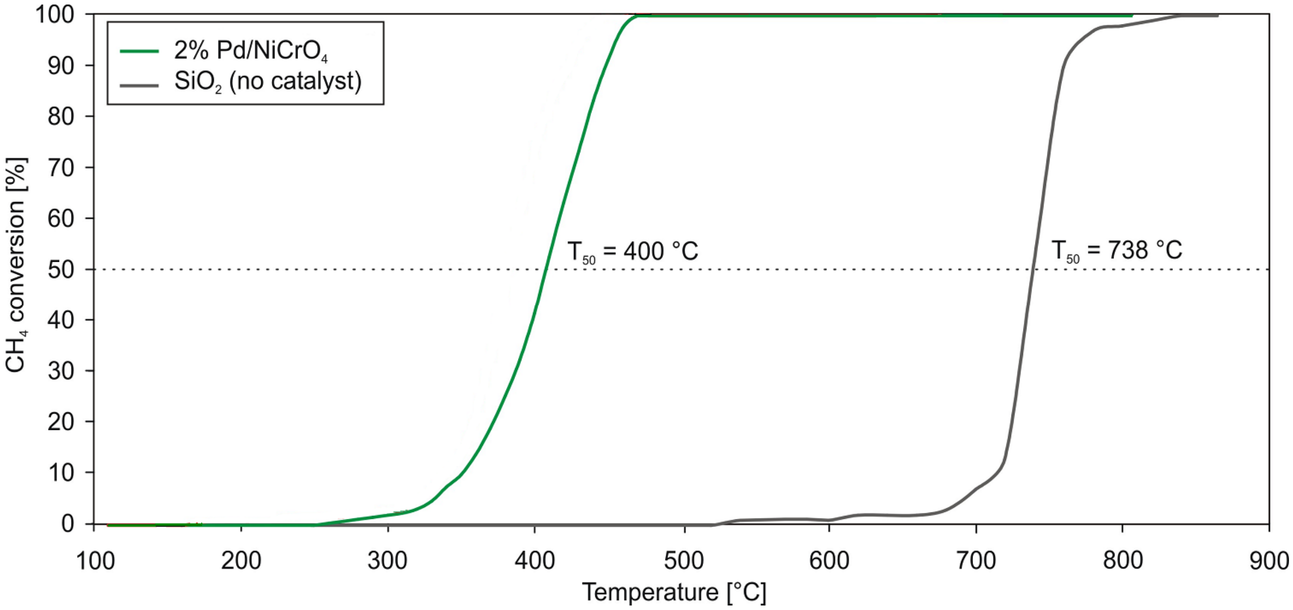

Figure 9: Temperature Programmed Combustion (TPC) with nickel chromate and without any catalyst

References for chapter 5

1) Conti F., Rossati A., Vella L.D., Specchia S., Specchia V., "*Kinetic Analysis of Pd-based Methane Combustion Catalysts.*" In: XXXII Annual Meeting of the Combustion Institute Italian Section, 26-28/04/2009, Napoli. ISBN: 978-88-88104-10-2, Page II-2/II-8

7 Ceria Zirconia oxide catalyst

In view of its high activity, supported PdO is usually the employed catalyst for CH4 combustion in applications which require low auto-ignition temperatures, such as in the treatment of internal combustion engine exhausts, and in catalytic combustors for gas turbines with ultra-low emissions [1]; PdO exhibits an outstanding activity for CH4 combustion, but is particularly sensitive to temperatures above about 850 °C [8,9], where PdO loses its activity mainly due to its decomposition to Pd [1]

In particular, the active state of Pd particles is a fully oxidized surface state, and the formation of oxygen species on the surface of PdO is crucial to explain the catalytic activity[2,10].

Although several studies are reported in the literature on CH_4 combustion kinetics over Pd catalysts,[10−20] there is no unanimity about the mechanisms of this reaction: Eley-Rideal (ER)[10−13], Langmuir Hinshelwood (LH)[14−16], and Mars van Krevelen (MvK)[13,15-20] mechanisms have been proposed.

This thesis reports the kinetic study carried on 2% Pd over $Ce_xZr_{1-x}O_2$ catalyst (hereafter named PCZ); moreover, also the kinetics of the sole $Ce_xZr_{1-x}O_2$ carrier (hereafter named CZ) was investigated.

The aim of this part of the research was the determination of the kinetic equation and related parameters.

The comparison between PCZ and CZ kinetics had the role to better understand the mechanisms of the noble metal deposited over the CZ carrier toward the methane combustion.

The PCZ catalyst was previously studied for CH_4 combustion in domestic appliances [3−7] , and for CH_4/air and CH_4/H_2/air lean mixtures oxidation into small monoliths (micro-burners)[21,22] as alternative method to produce contemporarily thermal and electrical energy.[22]

CeO_2 is a very promising catalyst thanks to the good capability of Ce in changing rapidly its oxidation number from Ce^{3+} to Ce^{4+} state, with a consequent fast release of O_2 from its lattice to the nearby species[23−25]: this O_2 mobility was proven to assist Pd in surface O_2 bonding helping thus the oxidation. ZrO_2 was chosen to counteract the sintering of CeO_2 and improve the specific surface area: mixing high melting temperature oxides should improve thermal stability[4,5,24−26].

Moreover, it was also demonstrated that upon incorporation of ZrO_2 into a solid solution with CeO_2, the reducibility of the Ce^{4+} is strongly enhanced compared to pure CeO_2,[24] so as the thermal stability and oxygen storage capacity [27] .

Thus, ZrO_2 was added in proportion of 2 moles of ZrO_2 per mole of CeO_2.

Moreover, PCZ systems are also known in literature as very good and promising catalysts for other industrial applications, such as three-way catalysts (TWC) for automotive applications,[27−31] or catalysts for diesel soot combustion,[32,33] and NO reduction by CO.[34−37]

Experimental part

CZ and PCZ catalysts were prepared by solution combustion synthesis.[38]

A homogenous aqueous solution of Ce and ZrO nitrates as oxidizers and glycine as organic fuel, dosed in stoichiometric ratio, once dissolved in distilled water, was placed into an oven at 650°C.[26] $Pd(NO_3)_2$ was directly added to the precursors solution to co-synthesize 2% b.w. of Pd on the CZ carrier in a "one shot" preparation.

This preparation route was preferred since a considerable portion of Pd could be encapsulated into the porous support, resulting in an embedded active metal with improved thermal stability; the positive characteristics of embedded catalytic phases compared to the traditional impregnated ones were pointed out in a very recent review paper [39].

Following combustion synthesis, catalysts were calcined in calm air for 2 h at 800 °C [26].

Reagent name	**Formula**	**Quantity per gram of catalyst**
Cerium Nitrate	$Ce(NO_3)_3\_6H_2O$	**1,038 g**
Zirconium Oxynitate	$ZrO(NO_3)_2\_6H_2O$	**1,622 g**
Palladium Nitrate	10% solution. H2O	**0,434 g**
Glycine	$COOH.CH_2.NH_2$	**1,356 g**

Table 2: reagents for 1gr of Pd/ $Ce_{0,33}Zr_{0,66}O2$

7.1 Characterization techniques

Methane programmed combustion was performed in the same experimental test rig outlined in Figure 8.

It was a U shaped reactor, employing a quartz tube (inner diameter 4 mm outer 6mm) for the catalyst housing; that Figure shows also a scheme of the experimental apparatus used for this purpose.

Experiments were undertaken using 0.05 g, of powdered catalyst diluted with 0.45 g of SiO_2; the feed flow rate was kept equal to 50 Nml min^{-1} which was the same employed for the detailed kinetic assessment.

In this case however, the gas recirculation pump was kept off in order to work with higher reactant concentration so that the comparison between different catalyst can be done more easily.

H_2 temperature programmed reduction (H_2-TPR) and O_2 temperature programmed desorption (O_2-TPD) analysis (Thermoquest TPD/R/O 1100 Series, Thermo Finningan analyzer, equipped with a thermal conductivity detector TCD) were also employed to investigate the O_2 desorption with temperature and to quantify the presence of PdO on the catalysts' surface on fresh and aged samples (that is, after the use for the kinetic tests).

TPD/R/O tests were performed on both PCZ and CZ catalysts, and on the PCZ sample after the kinetics assessment (used PCZ catalyst). H_2-TPR tests were performed by firstly flowing 10 Ncm^3 min^{-1} of 5% H_2 in Ar, increasing the temperature from 50 to 900 °C at 10 °C min^{-1} to evaluate the H_2 consumption. To determine the reference global amount of potential PdO (with the assumption that it remained the same for fresh and used catalysts), firstly a complete oxidation treatment was performed by flowing 40 Ncm^3 min^{-1} of pure O_2 increasing the temperature from 25 to 750 °C at 40 °C min^{-1} followed by cooling to room temperature in the same oxidizing atmosphere.

With the catalysts completely oxidized, H_2-TPR tests were performed again by flowing once more 10 Ncm^3 min^{-1} of 5% H_2 in Ar, increasing the temperature from 50 to 900°C at 10°C min^{-1} to evaluate the new H_2 consumption.

The reference global amount of potential PdO was calculated as the difference between the integral TCD curve (linked to the adsorbed H_2 volumes) of the completely oxidized PCZ catalyst and that of the CZ support.

The PdO oxide percentages on fresh and used PCZ catalysts were calculated considering their integral adsorbed H_2 connected with the TCD curves (reduced by the CZ support effect) related to the reference global amount of potential PdO.

7.2 Characterization results

The XRD diffraction patterns of the as-prepared catalytic powders (Figure 10), showed that both CZ and PCZ crystallized as solid solution of CeO_2 and ZrO_2, with very well detectable peaks, in agreement with previous studies [26,40].

These peaks corresponded to two different phase compositions ($0.5Ce$-$0.5ZrO_2$ and $2Ce$-$3ZrO_{10}$), which insisted to the same peaks; the assignment to one of the two phases, or the presence of a mixture of the two phases, was impossible with the analysis of only the XRD spectra.

Moreover, the presence of possible micro-domains of Ce-rich or Zr-rich phases cannot be detected by conventional diffraction analysis because the crystallographic structure and orientation of the atomic planes are the same for all the CeO_2- and ZrO_2-enriched regions within the crystallite[28].

Only more complex techniques, such as neutron diffraction, or luminescence spectroscopy using Eu^{3+} ion as a structural probe, proved to be able to identify in-homogeneities even in samples appeared homogeneous from XRD analysis, revealing the presence of nanometric domains with different compositions [41].

The width of these peaks suggested their nanoscale dimension: by applying the Scherrer equation, it was possible to estimate the dimensions of the grain size, equal to 21.8 nm for CZ carrier and 11.9 nm for PCZ catalyst, respectively.

No diffraction peaks of either Pd or PdO were detected in the PCZ system, a sign that Pd dispersion was satisfactory.

The addition of Pd in the simultaneous one shot preparation of PCZ sample allowed almost halving the average size of the crystallites.

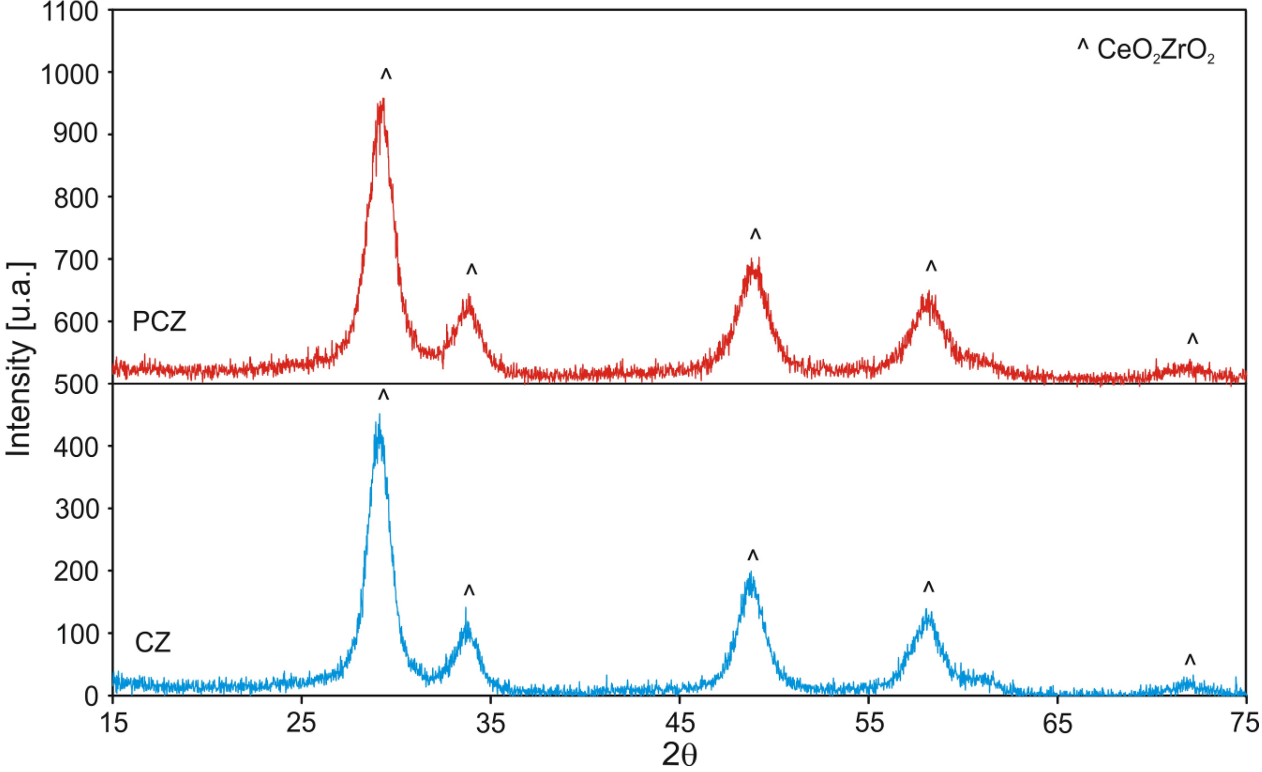

Figure 10: Xrays analysis on $CeZrO_2$

The calculated BET value of the specific surface area were 16.5 $m^2\ g^{-1}$ for CZ sample and 22.5 $m^2\ g^{-1}$ for PCZ one, respectively; the slight increase of the BET value for the PCZ sample was in agreement with the lower crystallite size calculated via the Scherrer equation: a sign that the presence of Pd during the co-synthesis leaded to more nanometric material.

The SEM analysis allowed enlightening the nanometric morphology on both the examined catalysts (see Figure 11, reporting only PCZ sample) obtained by SCS. The EDX elemental analysis confirmed the purity degree of both the samples: only Ce, Zr and O_2 were detected on CZ sample, whereas on PCZ one also Pd was detected.

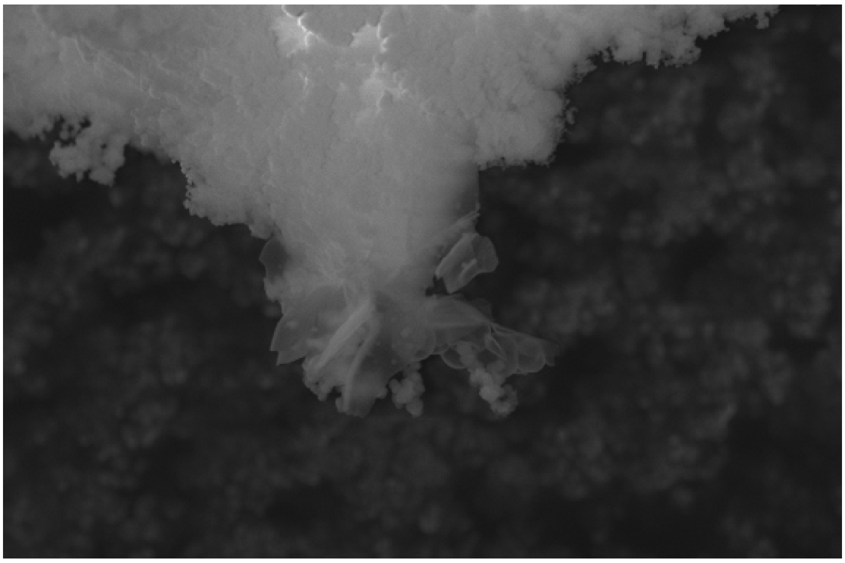

Figure 11: PCZ SEM picture

The carbon mole balance during the CH_4-TPC experiments was closed within 5%. And the only products formed during the combustion were water (removed prior entering the analyzer through a condenser settled at 3 °C), and carbon dioxide.

No carbon monoxide was detected in the reactor effluent mixture, in accordance with the high inlet ratio of oxygen used.

Figures 12-13 show the sigma-shaped curves of the CH_4-TPC analysis reporting the CH_4 conversion versus temperature: both the catalysts had a lower the T_{50} than the blank test (reported in figure 9): PCZ catalyst appeared as the most promising one, thanks to its lowest T_{50} (420 °C respect to 580 °C of CZ, and 738 °C of the blank test).

These experimental results were in slight disagreement with some literature data [43,44,45] where, in conditions similar to ours, the specific combustion activity of PdO supported on Al_2O_3 showed a persistent activity hysteresis between 450 and 750 °C.

In those works hysteresis in CH_4 combustion rate was caused by higher activation energy for reduction of oxygen chemisorbed on metallic Pd (so metallic Pd is a poorer catalyst than PdO) and by kinetically slow re-oxidation of Pd metal relative to PdO decomposition [43].

The catalyst PCZ prepared by combustion synthesis instead featured a PdO so well intimately mixed in the CZ matrix that state transitions between Pd and PdO took place smoothly without noticeable hysteresis (Figure 12); instead Pd/ Lanthanum Manganite presented like the literature data of 45,46,47 the typical decrease in catalytic activity between 650 and 580°C figure (34).

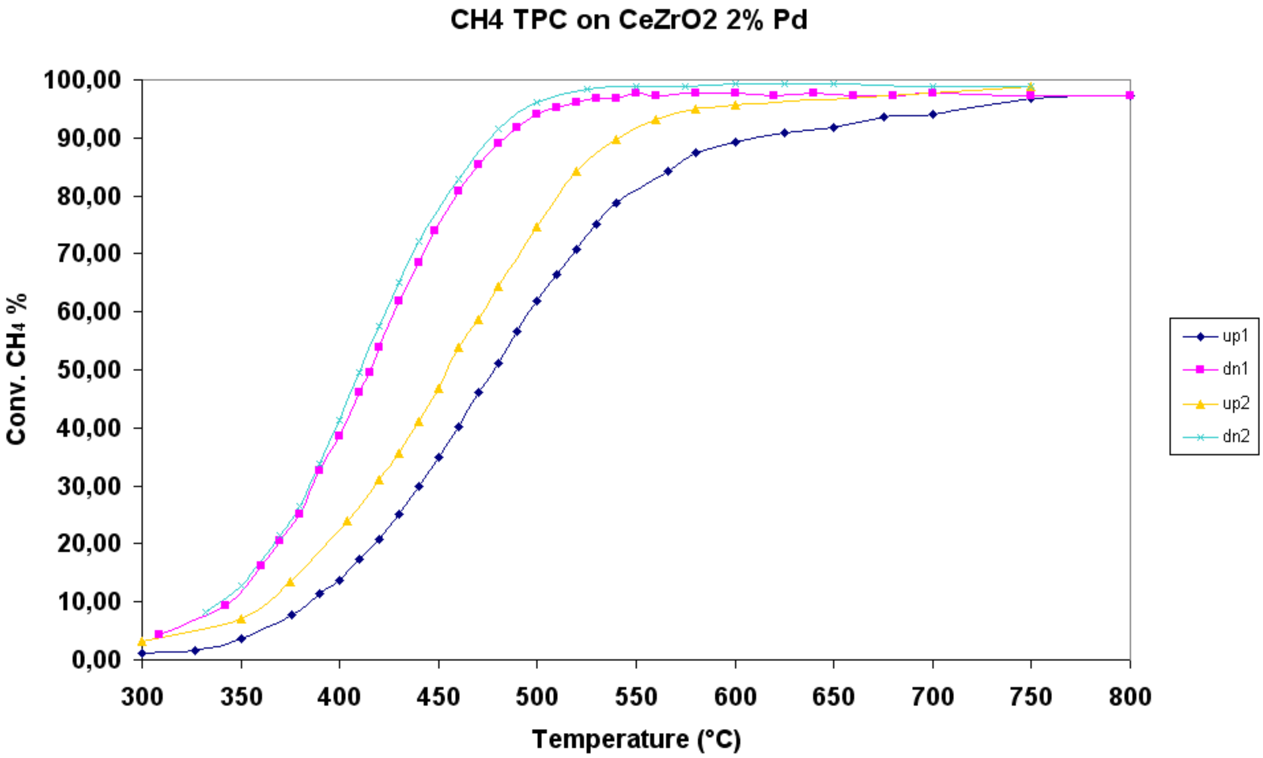

Figure 12: methane TPC using 2% Pd /CeZrO_2

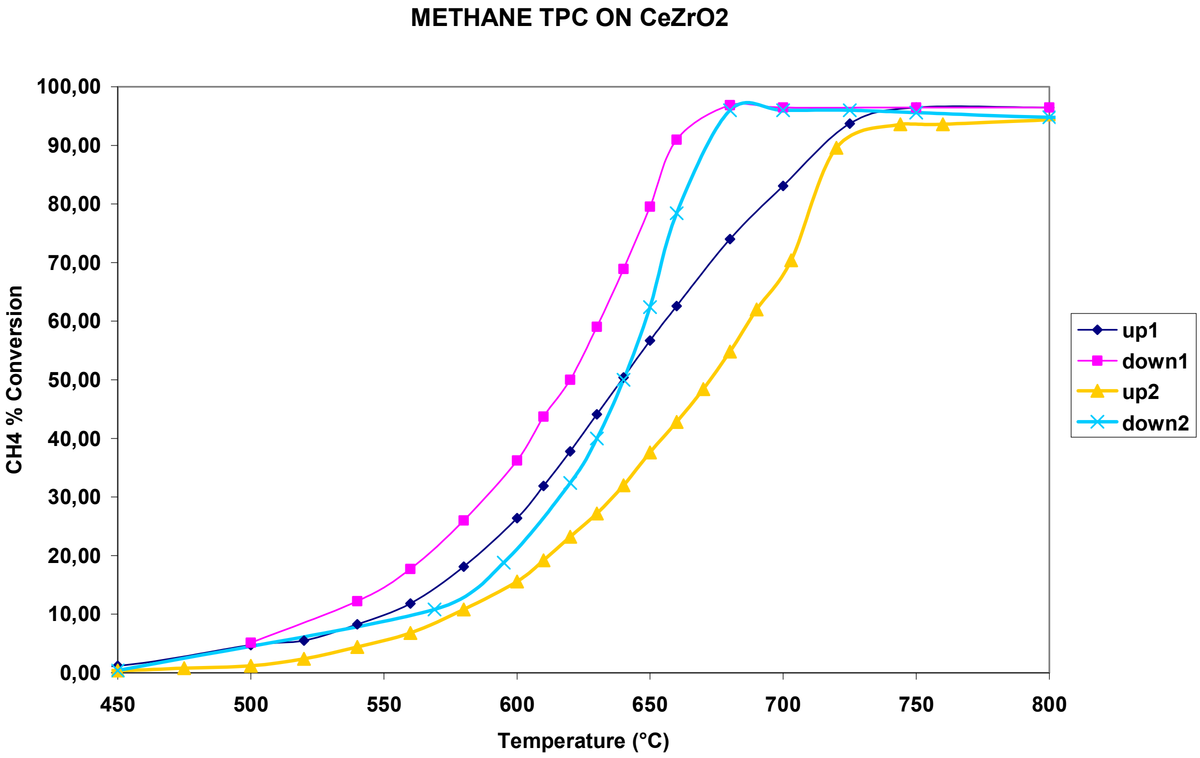

Figure 13: methane TPC using undoped CeZrO2

The oxidation state of the as-prepared catalysts was studied by O_2-TPD (Figure 14).

The normalized O_2-TPD curve of the fresh PCZ catalyst showed the desorption threshold near 480 °C, with the peak near 570 °C.

This peak shifted towards higher temperatures after the catalyst use for the kinetic assessment (about 200 h of work): desorption started at around 585 °C, with the peak at about 670 °C.

For the fresh PCZ catalyst, the temperature range of the O_2 desorption peak corresponded approximately to the range where the Pd/PdO transition was recorded.

Moreover, the end of the desorption peak corresponded approximately to the temperature where the CH_4 conversion became complete.

The O_2 desorption temperatures of the fresh PCZ catalyst were not too far from the temperature at which adsorbed O_2 was found to desorb from Pd(111) single crystal surface (490 °C).[46]

In terms of desorption performance, PCZ maintained practically the same amount of desorbed O_2, evaluated as 54.2 and 56.7 μmol g^{-1} for the fresh and used samples, respectively while the only CZ carrier (not reported here) desorbed a very low amount, equal as 1.8 μmol g^{-1}.

H_2-TPR analysis (Figure 14) allowed estimating the amount of PdO available at the PCZ catalyst surface: 34.6% and 84.9% for the fresh and used samples, respectively.

From the normalized H_2-TPR profiles, it was possible to note processes involving the reduction of both the noble metal oxide and the carrier.[47−49].

The low temperature peaks can be attributed to the reduction of the dispersed metal phase and to a partial reduction of the support:[47−49] it was clearly visible, in fact, that on both fresh and used catalysts Pd was reduced at room temperature, then at around 70−80 °C there was the bulk Pd hydride decomposition.[49,50].

The high-temperature features can be associated to the processes of deep reduction in the bulk of the ceria-zirconia solid solution[47,49,51]; the latter was an indirect sign that the solid solution was quite homogeneous.

The overall appearance of the curves was similar to that reported in the literature for some other ceria-zirconia supported noble metal catalysts[50,51]: it was demonstrated, in fact, that for homogeneous ceria-zirconia solid solutions Ce^{4+} reduction to Ce^{3+} occurred in the same time at the surface and in the bulk [53]. The presence on the used catalyst of two smooth peaks at high temperature can be interpreted as a partial de-mixing of the homogeneous solid solution, probably due to some ageing effects.

Both the values calculated by O_2-TPD and H_2-TPR were perfectly in line with previous studied performed on the same PCZ catalyst used in domestic burners application for CH_4 combustion [28].

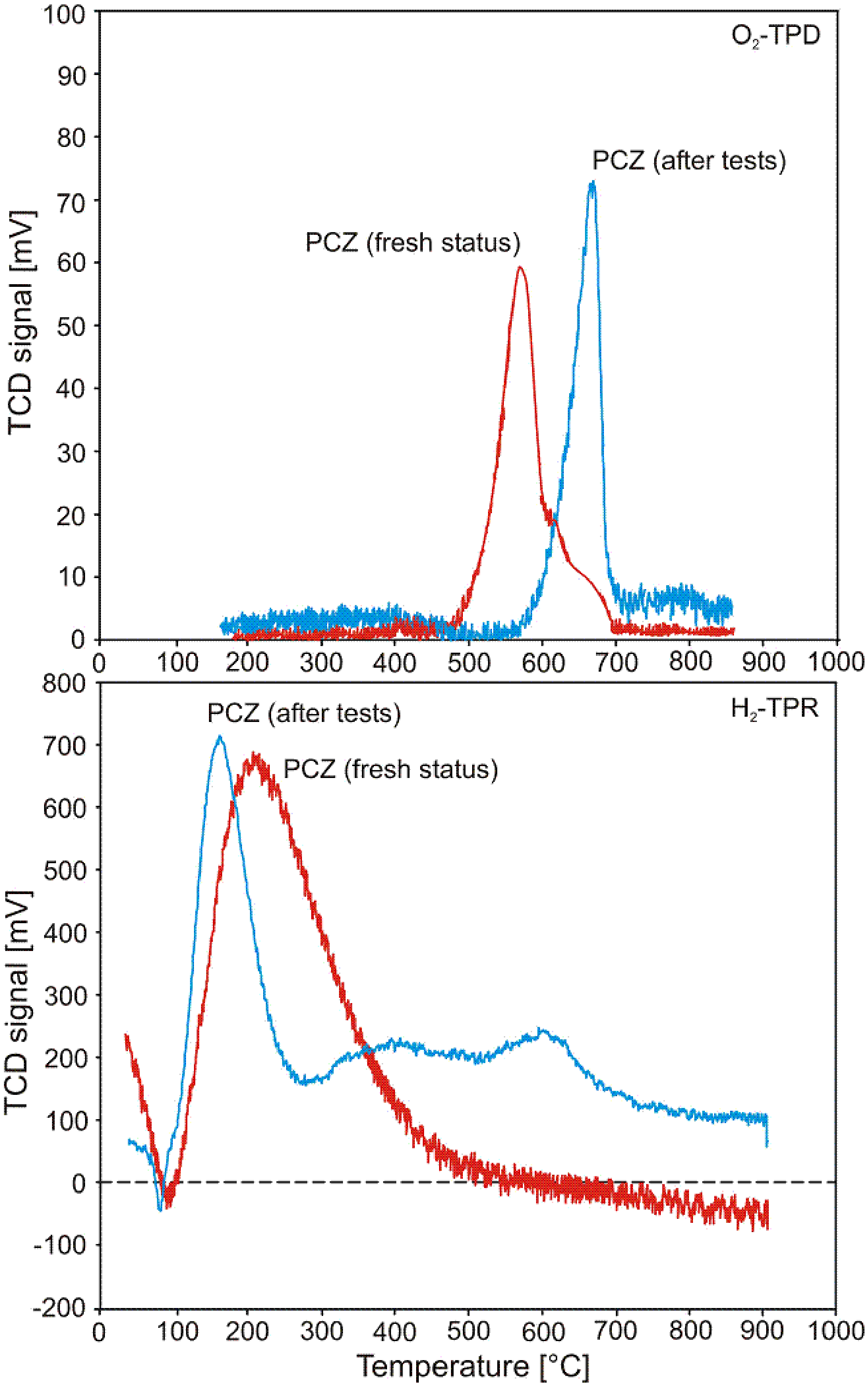

Figure 14: H_2 Temperature programmed reduction (upper) and O_2 temperature programmed oxidation(lower) of PCZ catalyst

As a final comment on basic characterization because the Ceria Zirconia support showed an overall better performance, having a T50% between 400 and 450°C and no hysteresis during cooling, it was chosen as catalyst for the micro combustor.

7.3 Detailed kinetic analysis of undoped and doped ceria-zirconia

7.3.1 Kinetics measurements

A reaction kinetics study was performed to establish the more appropriate kinetics law and the temperature dependence of the characteristic kinetic parameters.

The experimental test rig was based on a continuous recycle micro reactor, employing a quartz tube (inner diameter 4 mm outer 6mm) for the catalyst housing. Figure 8 shows a scheme of the experimental apparatus used for this purpose.

The amount of powdered catalyst was 0.05 g, diluted with 0.45 g of SiO_2; the recycle of the reacting gases was enabled by a Teflon-membrane pump (KNF Italia).

Analysis of the inlet and outlet gas feeds were performed via the above described analytical tools (the reactor may be bypassed closing the bypass valve installed ahead the mass flows: in this way the reacting mixture was directly sent to the analyzer).

Two pressure indicators were positioned at the inlet and at the outlet of the reactor to control and measure the pressure.

The feed flow rate was kept equal to 50 Nml min^{-1}, whereas the overall recycle flow rate passing through the reactor was 1,050 Nml min^{-1}.

The O_2 and CH_4 feed concentrations were varied in the ranges 2-15% and 0.5-2.5%, respectively, He being the balance. Runs were performed in the temperature range 380-500 °C for the PCZ sample, and 480-580 °C or the CZ one, whereas the absolute operating pressure was practically equal to 1 bar. Each test was repeated at least three times to verify the stability and repeatability of the measurements.

7.3.2 Results and discussion: kinetics analysis and modeling

For both catalysts (abbreviated respectively PCZ and CZ), the present kinetic study was based on the data of CH_4 reaction rate (R_{CH4} expressed as $mol_{CH4}\ g^{-1}\ s^{-1}$) obtained at steady-state mode, operating the reactor under a differential regime of CH_4 conversion and calculated according to:

$$R_{CH4} = \frac{F_{fed} \cdot \Delta_{CH4}}{M_{cat}} \qquad (5)$$

where F_{fed} was the flow rate fed to the system (without the recycled rate), Δ_{CH4} the difference between the inlet CH_4 concentration (determined before the recycled rate) and the one at the reactor outlet, and M_{cat} the mass of catalyst loaded into the reactor. Also for the kinetics experiments the carbon mole balance was closed within 5%.

For both catalysts, the absence of mass transfer limitations at reaction conditions was verified both experimentally and theoretically.

The high recirculation ratio used assured a low CH_4 conversion: for a recirculation ratio equal to 20, the CH_4 conversion per passage was approximately 2% (see Figure 15).

This was sufficient to eliminate almost any external mass transfer effect on the overall conversion measured. Moreover, the absence of external mass transfer was also evaluated by estimating the Damköhler number at each operating condition [52]: more than 85% of the experimental data presented a Damköhler number less than 0.05, whereas the remaining 15% presented a Damköhler number between 0.05 and 0.09: This means that even in the most unfavourable conditions the external diffusion mass transfer was negligible.

Besides, assuming a tortuosity factor equal to 2 for the catalyst pellets, also the internal mass transfer did not significantly affect the attained conversion (the catalyst effectiveness factor was always higher than 0.999). Within these limits the average values of O_2 and CH_4 partial pressure in the catalyst were assumed as reference data for the assessment of a kinetic law.

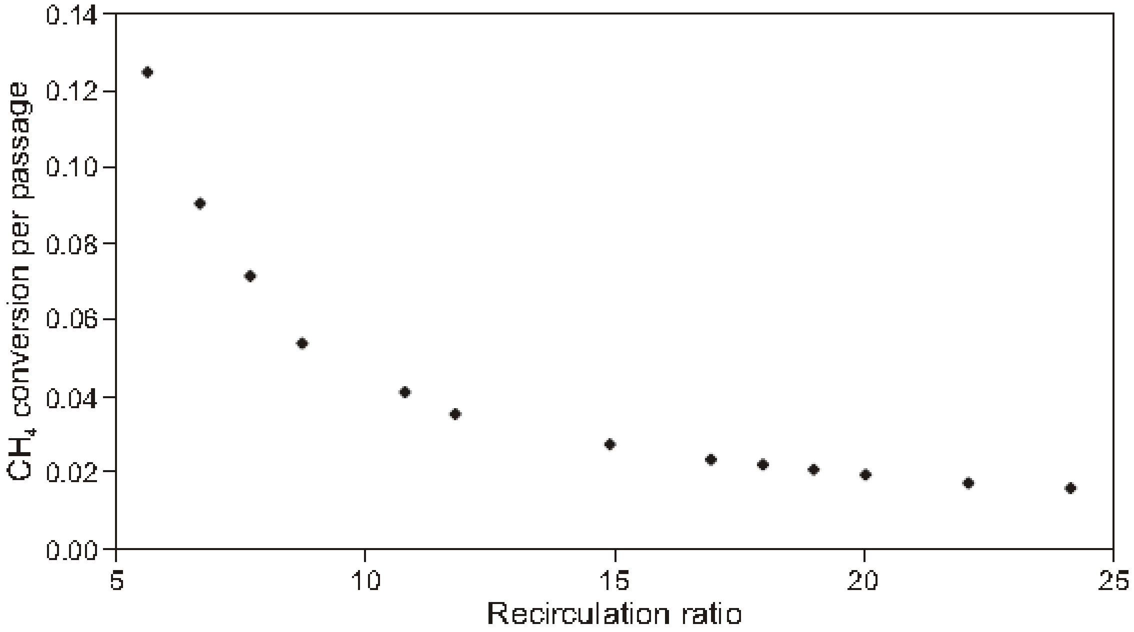

Figure 15: increasing more and more recirculation ratio the reacting system becomes a differential reaction reactor.

7.3.3 Theoretical discussion about the models presented

In this study 12 different models were taken into account to evaluate the kinetic expression of PCZ catalyst and CZ carrier; their mathematical expressions are reported in Table 3.

Model	Equation	Description
ER1	$R_{CH_4} = k_{sr}\frac{K_{O_2}p_{O_2}p_{CH_4}}{1+K_{O_2}p_{O_2}}$	Non dissociative oxygen chemisorption, one oxygen species involved
ER2	$R_{CH_4} = k_{sr}\frac{\sqrt{K_{O_2}p_{O_2}}\,p_{CH_4}}{1+\sqrt{K_{O_2}p_{O_2}}}$	Dissociative oxygen chemisorption, one oxygen species involved
ER3	$R_{CH_4} = k_{sr}\frac{K_{O_2}^2p_{O_2}^2p_{CH_4}}{\left(1+K_{O_2}p_{O_2}\right)^2}$	Non dissociative oxygen chemisorption, two oxygen species involved
ER4	$R_{CH_4} = k_{sr}\frac{K_{O_2}p_{O_2}p_{CH_4}}{\left(1+\sqrt{K_{O_2}p_{O_2}}\right)^2}$	Dissociative oxygen chemisorption, two oxygen species involved
LH1	$R_{CH_4} = k_{sr}\frac{K_{O_2}p_{O_2}K_{CH_4}p_{CH_4}}{\left(1+K_{O_2}p_{O_2}+K_{CH_4}p_{CH_4}\right)^2}$	Non dissociative oxygen chemisorption, one oxygen species involved

LH2	$R_{CH_4} = k_{sr} \dfrac{\sqrt{K_{O_2} p_{O_2}} K_{CH_4} p_{CH_4}}{\left(1 + \sqrt{K_{O_2} p_{O_2}} + K_{CH_4} p_{CH_4}\right)^2}$	Dissociative oxygen chemisorption, one oxygen species involved
LH3	$R_{CH_4} = k_{sr} \dfrac{K_{O_2}^2 p_{O_2}^2 K_{CH_4} p_{CH_4}}{\left(1 + K_{O_2} p_{O_2} + K_{CH_4} p_{CH_4}\right)^3}$	Non dissociative oxygen chemisorption, two oxygen species involved
LH4	$R_{CH_4} = k_{sr} \dfrac{K_{O_2} p_{O_2} K_{CH_4} p_{CH_4}}{\left(1 + \sqrt{K_{O_2} p_{O_2}} + K_{CH_4} p_{CH_4}\right)^3}$	Dissociative oxygen chemisorption, two oxygen species involved
MvK1	$R_{CH_4} = \dfrac{k_1 p_{O_2} k_2 p_{CH_4}}{k_1 p_{O_2} + 2k_2 p_{CH_4}}$	Reduction and re-oxidation step by non dissociative oxygen
MvK2	$R_{CH_4} = \dfrac{k_1 \sqrt{p_{O_2}} k_2 p_{CH_4}}{k_1 \sqrt{p_{O_2}} + 2k_2 p_{CH_4}}$	Reduction and re-oxidation step by dissociative oxygen
MvK3	$R_{CH_4} = \dfrac{k_1 p_{O_2} k_2 p_{CH_4}}{k_1 p_{O_2} + 2k_2 p_{CH_4}} \left(1 - \dfrac{k_1 p_{O_2}}{k_1^*}\right)$	Reduction and re-oxidation step by non dissociative oxygen, taking into account the concentration of the molecular oxygen
MvK4	$R_{CH_4} = \dfrac{k_1 p_{O_2} k_2 p_{CH_4}}{k_1 p_{O_2} + 2k_2 p_{CH_4} + \left(\dfrac{k_1 k_2}{k_3}\right) p_{O_2} p_{CH_4}}$	Reduction and re-oxidation step by non dissociative oxygen, slow desorption of the reaction products

Table 3: List of the Kinetic Models Used to Implement the Experimental Data on PCZ and CZ Catalysts

The results coming out from the modelling approach were obtained by means of a computer programmed to perform a random walk towards the optimal solution from a starting approximate value.

All the values of the kinetics parameters were derived, on the basis of the described kinetic expressions, by least-squares fitting the experimental data.

Within the considered models (see Table 3), the ER ones feature O_2 chemisorption and reaction with CH_4 from the gas phase; the surface reaction is assumed to be rate determining.

The fact that O_2 is assumed to adsorb can be justified by the high inlet O_2 partial pressure, compared to the CH_4 inlet partial pressure[10−13,53].

These models, and particularly ER2, that supposes dissociative adsorption of oxygen, were applied successfully for the oxidation of methane over different perovskite-type catalysts[10,53].

As an alternative, LH mechanisms account for the competitive adsorption of CH_4 and O_2 with the surface reaction as rate-determining step; moreover, the adsorption is limited to a monolayer[14−16].

Finally, four different MvK mechanisms were considered, too. MvK models are the most frequently used to describe the oxidation of organic compounds over noble metals as well as over many metal oxides.[13,16−20].

Among noble metals, MvK mechanisms are likely to occur for Pd and Rh, since it was observed that they present different interchangeable catalytically active oxidation states at the reaction conditions used for hydrocarbons oxidation [19].

According to these MvK models, the reaction takes place through alternative oxidations and reductions of the catalyst surface, the surface oxidation being produced by molecular O_2 dissociatively adsorbed from the gas phase [19].

The CH_4 reacts with the chemisorbed atomic oxygen in successive irreversible steps, yielding finally the total oxidation products and making free the corresponding site fraction θ:

$$O_2 + \theta \xrightarrow{r_1} \theta_{O_2} \xrightarrow{r_1^*} 2\theta_O \tag{6}$$

$$CH_4 + \theta_O \xrightarrow{r_2} \theta_I \xrightarrow{r_3} products + \theta \tag{7}$$

The considered MvK1 model (Table 3) corresponds to a reduction step where the CH_4 reacts with a single oxidized site and with a re-oxidation step by gas phase molecular O_2, involving a single reduced surface site.

The factor “2” in the denominator of the corresponding rate equation arises from the number of O_2 molecules needed for the complete combustion of CH_4 molecule [13]

MvK2 model instead, is similar to MvK1 but the re-oxidation of the single site is done by dissociatively O_2 [16]; MvK3 model takes into account the concentration of molecular O_2, which is adsorbed on the active site and then dissociates on it[20].

On the other hand, MvK4 model takes into account the slow desorption of the reaction products[19].

The discrimination of the kinetic models was done by rejecting first the models that led to thermodynamically inconsistent adsorption heats and activation energies, or negative kinetic parameters in the considered confidence interval.

Then, the best fitting model, for CZ and PCZ systems, respectively, was selected among the remaining models, adopting as criterion the minimization of the least-squares fitting sum (Σ) of R_{mod} towards R_{exp}.

In particular, the surface reaction constant $k_{sr,i}$ and the adsorption coefficient K_i, present in the equation reported in Table 3, can be expressed as a function of temperature by Arrhenius- and van’t Hoff-type expressions, respectively:

$$k_{sr,i} = k_{sr,i}^{\infty} \exp\left(-\frac{E_{sr}}{RT}\right) \tag{8}$$

$$K_i = K_i^{\infty} \cdot \exp\left(-\frac{\Delta H_i}{RT}\right) \tag{9}$$

7.3.4 Palladium ceria zirconia model selection

By analyzing the experimental data obtained for the PCZ catalyst at the various tested temperatures, the data points in Figures 16 to 19 (R_{CH4} versus p_{CH4}) and 20 to 23 (R_{CH4} versus p_{O2}), respectively, it is worth noting that, when the O_2 concentration was maintained at a constant value and the CH_4 concentration was increased (see Figures 16 to 19), R_{CH4} increased with the enhancement of p_{CH4} and of the temperature. Instead, when the CH_4 concentration was maintained constant and the O_2 concentration fed to the reactor was increased (see Figures 20 to 23), R_{CH4} increased up to a maximum value, and then decreased with the enhancement of p_{O2} and of the temperature.

It was as if the available active sites were completely saturated by the presence of O_2, and then the reaction rate could not increase anymore by further increasing the O_2 concentration; moreover, the presence of O_2 on the active sites did not allow CH_4 to react, thus its conversion decreased. Such a behavior could not be explained by adopting any ER model.

Then, only LH and MvK models were adopted to fit the experimental data: the obtained results are reported in Table 4, concerning the LH models, and Table 5 (columns 2 to 4), concerning the MvK models. Models LH3 and MvK2 (not reported in Tables 4 and 5) gave inconsistent results, thermodynamically not feasible (inconsistent activation energies, or negative adsorption heats, or negative kinetic parameters), thus they were rejected.

Among the selected LH and MvK mechanisms, the best fitting belonged to the MvK models, which presented the lower Σ values. In particular, MvK3 model *(which considers the concentration of the molecular O_2 adsorbed on a single active site on the catalyst surface, and then the dissociation rate of the adsorbed molecular oxygen on the same active site)* was considered as the best model fitting the experimental data (it presented the lowest Σ value), and it could be considered as the more realistic mechanism describing the reaction on PCZ catalyst.

Specifically, the obtained kinetic parameters were $E_{\mathrm{act},1}$ = 23.8 kJ mol^{-1} (activation energy for the molecular oxygen adsorption), $E_{\mathrm{act},2}$ = 31.9 kJ mol^{-1} (activation energy for the reaction between CH_4 and the adsorbed molecular O_2), and $E^{*}_{act,1}$ = 5.4 kJ mol^{-1} (activation energy for the adsorbed molecular O_2 dissociation), respectively.

The obtained modelling data from MvK3 are reported in Figures 16 to 23, respectively, as solid lines.

As a general comment, the quality of the fitting was satisfactory, as shown in the parity plot of figure 32.

A similar analysis was performed on the experimental data obtained by the kinetic tests with the CZ carrier, where the active element Pd was not present.

The experimental data are reported in Figures 24 to 27 (R_{CH4} versus p_{CH4}) and 28 to 31 (R_{CH4} versus p_{O2}), respectively.

While the trend of the R_{CH4} curves versus p_{CH4} was similar to that of catalyst PCZ (see Figures 16 to 23), the trend of R_{CH4} curves versus p_{O2} was different (see Figures 20 to 27), instead.

When the CH_4 concentration was maintained constant and the O_2 concentration fed to the reactor was increased (see Figures 28 to 31), in most of cases R_{CH4} increased up to a maximum plateau value for the higher p_{O2} values.

7.3.5 Ceria zirconia model selection

For CZ carrier, all the three families of models were used to fit the experimental data. In this case, all the LH models were inconsistent with the experimental data, thus they were rejected. ER models, instead, gave interesting results, which are reported in Table 6.

Among the MvK models, instead, only MvK1 and MvK2 gave consisted results, which are reported in Table 5 (columns 5 and 6).

Taking into consideration the obtained ER results, the most interesting models seemed ER1 (non dissociative oxygen chemisorption, one oxygen species involved) and ER3 (non dissociative oxygen chemisorption, two oxygen species involved), which presented very similar Σ values. The discrimination between these two models is difficult to tell.

But, most interesting resulted the values obtained with MvK1 (reduction and re-oxidation step by non dissociative oxygen) and MvK2 (reduction and re-oxidation step by dissociative oxygen) models: the obtained kinetic parameters in terms of activation energies were very similar among them, and the respective Σ values were lower to the ones calculated for the ER models.

It is worth noting that, because the difference between PCZ and CZ catalyst was only a 2% of Pd, most probably the reaction mechanism of these two catalysts was very similar.

Thus, if the selected mechanism for PCZ catalyst was MvK3, most probably, also CZ catalyst presented a mechanism governed by an MvK model.

The lowest Σ value belonged to the MvK1 model, which was then selected as “preferred” reaction mechanism on CZ carrier: it allowed obtaining the following kinetic parameters $E_{\mathrm{act},1}$ = 79.6 kJ

mol^{-1} (activation energy for the molecular oxygen adsorption), $E_{act,2}$ = 114.6 kJ mol^{-1} (activation energy for the reaction between CH_4 and the adsorbed molecular O_2), respectively.

7.3.6 Catalyst kinetical comparison

These values were higher compared the corresponding activation energies obtained for the PCZ catalyst (as expected), enlightening that the presence of Pd over the CZ carrier enhanced its catalytic activity, This was also in agreement with the T_{50} recorded on the CH_4-TPC experiments (see Figure 13).

Most probably, the presence of Pd over CZ (PCZ catalyst) favoured the dissociation of the adsorbed molecular O_2 (which remained in the molecular status on CZ catalyst), by favouring reaction r_1* (equation 2) so the atomic oxygen involved in the combustion reaction with CH_4 should be more active.

The data fitting is shown in figures 24 to 27 and 28 to 31 (solid lines) and in the parity plot drawn in Figure 32: as for the case of PCZ catalyst, also the quality of the CZ fitting was satisfactory

	LH1	LH2	LH4
E_{act} [kJ mol^{-1}]	71.0	57.9	44.6
k_{sr}^{∞} [mol g^{-1} s^{-1}]	11.4	1.01	5.42×10^{-1}
ΔH_{O_2} [kJ mol^{-1}]	37.0	104.2	26.4
ΔH_{CH_4} [kJ mol^{-1}]	10.4	21.5	62.2
Σ [mol^2 g^{-2} s^{-2}]	7.18×10^{-10}	3.28×10^{-10}	1.42×10^{-9}

Table 4: Results of the LH models for the PCZ catalyst.

	PCZ/MvK1	PCZ/MvK3	PCZ/MvK4
$E_{act,1}$ [kJ mol^{-1}]	31.9	23.77	33.8
k_1^{∞} [mol bar^{-1} g^{-1} s^{-1}]	8.76	7.26×10^{-1}	$2.31 \times 10^{+1}$
$E_{act,2}$ [kJ mol^{-1}]	21.0	31.9	24.4
k_2^{∞} [mol bar^{-1} g^{-1} s^{-1}]	7.26×10^{-1}	2.95×10^{0}	3.57×10^{-1}
$E_{act,1}^{*}$[kJ mol^{-1}]		5.4	
$k_1^{*,\infty}$ [mol g^{-1} s^{-1}]		2.66×10^{-3}	
$E_{act,3}$ [kJ mol^{-1}]			8.89
k_3^{∞} [mol g^{-1} s^{-1}]			2.12×10^{-4}
Σ [mol^2 g^{-2} s^{-2}]	1.08×10^{-10}	1.34×10^{-11}	2.01×10^{-11}

	CZ/MvK1	CZ/MvK2
$E_{act,1}$ [kJ mol^{-1}]	79.6	78.2
k_1^{∞} [mol bar^{-1} g^{-1} s^{-1}]	7.14×10^{-1}	8.88×10^{-2}
$E_{act,2}$ [kJ mol^{-1}]	114.6	120.9
k_2^{∞} [mol bar^{-1} g^{-1} s^{-1}]	$1.04 \times 10^{+2}$	$3.56 \times 10^{+3}$
Σ [mol^2 g^{-2} s^{-2}]	4.98×10^{-15}	6.07×10^{-15}

Table 5: Results of the MvK Models for the PCZ and CZ Catalysts.

	ER1	ER2
E_{act} [kJ mol^{-1}]	112.7	132.1
ΔH_{O_2} [kJ mol^{-1}]	−34.3	−82.6
k_{sr}^{∞} [mol bar^{-1} g^{-1} s^{-1}]	$1.68 \times 10^{+2}$	$2.79 \times 10^{+3}$
$K_{O_2}^{\infty}$ [bar^{-1}]	1.95×10^{-1}	2.00×10^{-5}
Σ [mol^2 g^{-2} s^{-2}]	9.31×10^{-15}	1.34×10^{-14}

	ER3	ER4
E_{act} [kJ mol^{-1}]	112.0	120.6
ΔH_{O_2} [kJ mol^{-1}]	−17.3	−45.4
k_{sr}^{∞} [mol bar^{-1} g^{-1} s^{-1}]	$6.87 \times 10^{+1}$	$3.97 \times 10^{+2}$
$K_{O_2}^{\infty}$ [bar^{-1}]	7.32	8.05×10^{-2}
Σ [mol^2 g^{-2} s^{-2}]	9.14×10^{-15}	9.81×10^{-15}

Table 6: Results of the ER Models for the CZ Catalyst

7.3.7 Palladium doped $Ce_{0,33}$ $Zr_{0,66}O_2$ plots

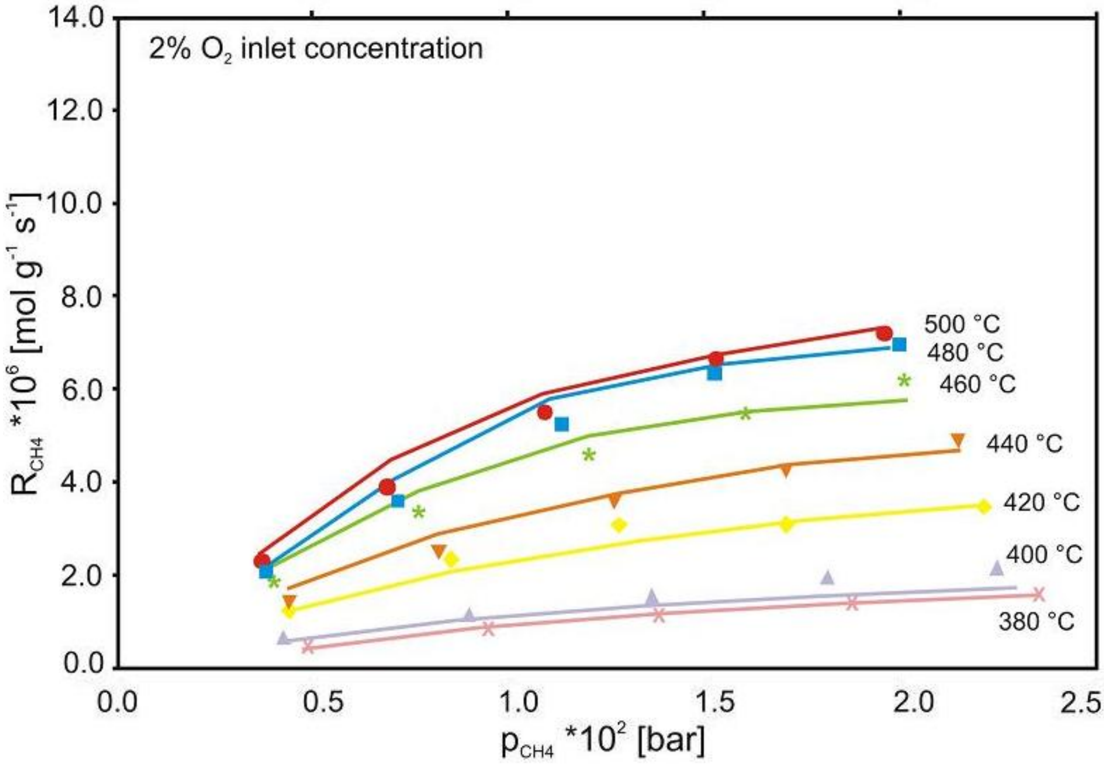

Figure 16: Reaction rate vs methane concentration; dots represent experiment, solid line model MVK3.

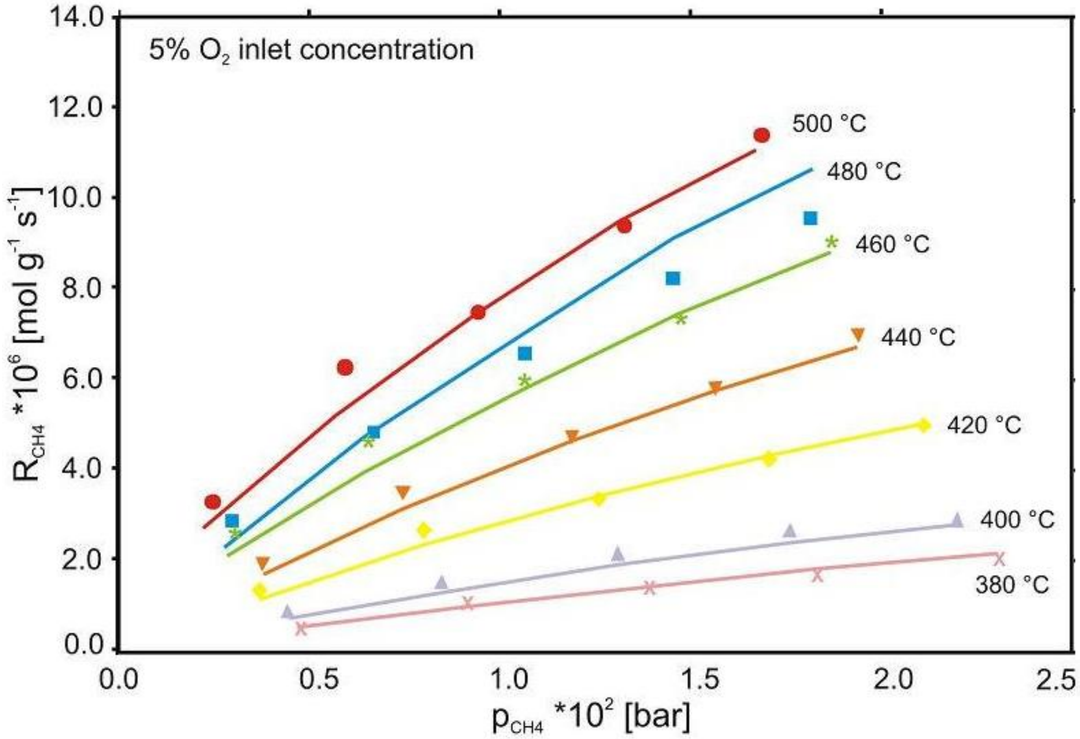

Figure 17: Reaction rate vs methane concentration; dots represent experiment, solid line model MVK3.

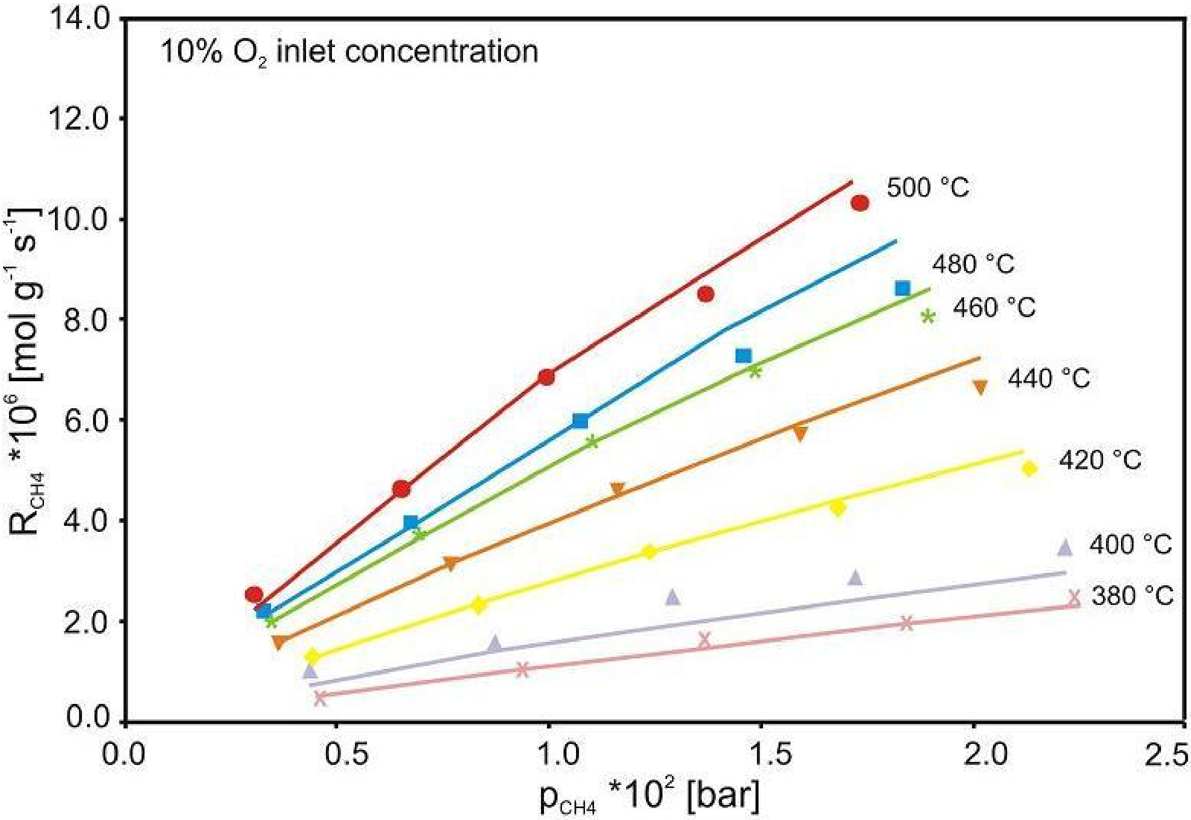

Figure 18: Reaction rate vs methane concentration; dots represent experiment, solid line model MVK3.

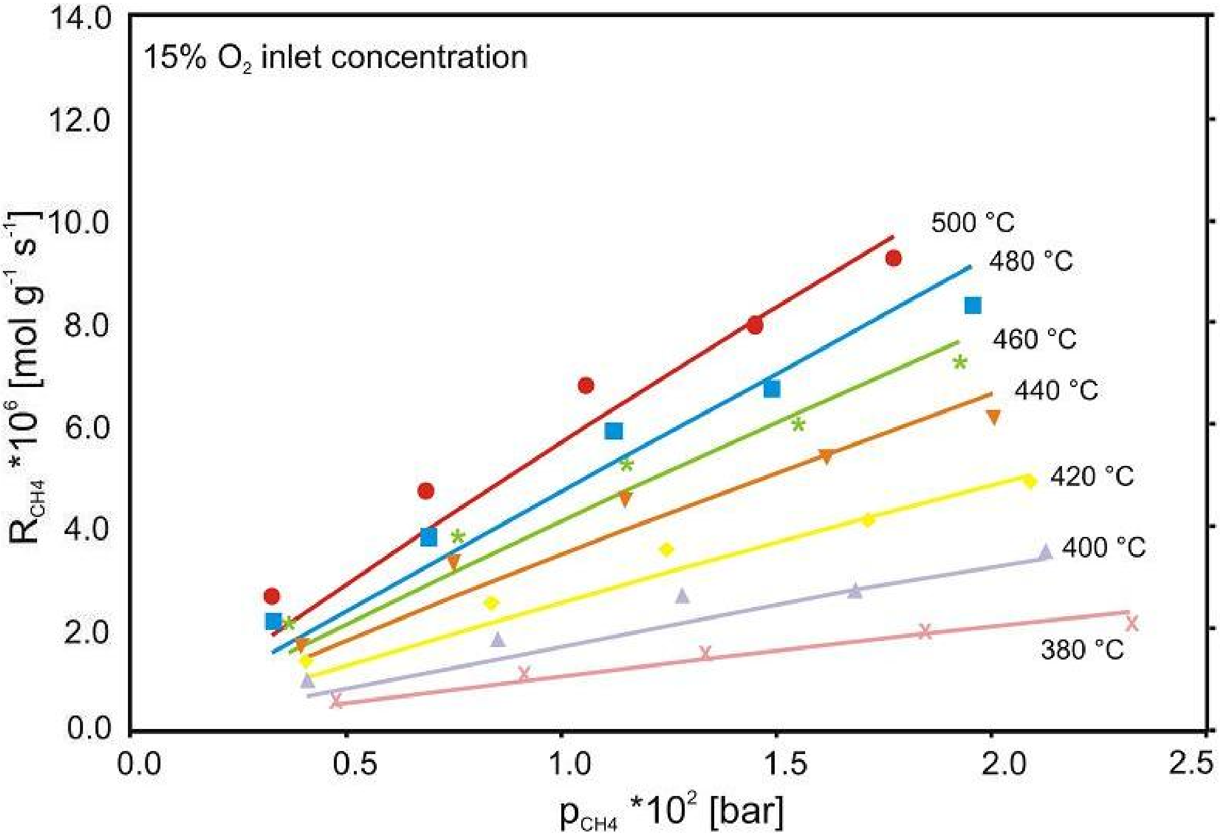

Figure 19: Reaction rate vs methane concentration; dots represent experiment, solid line model MVK3.

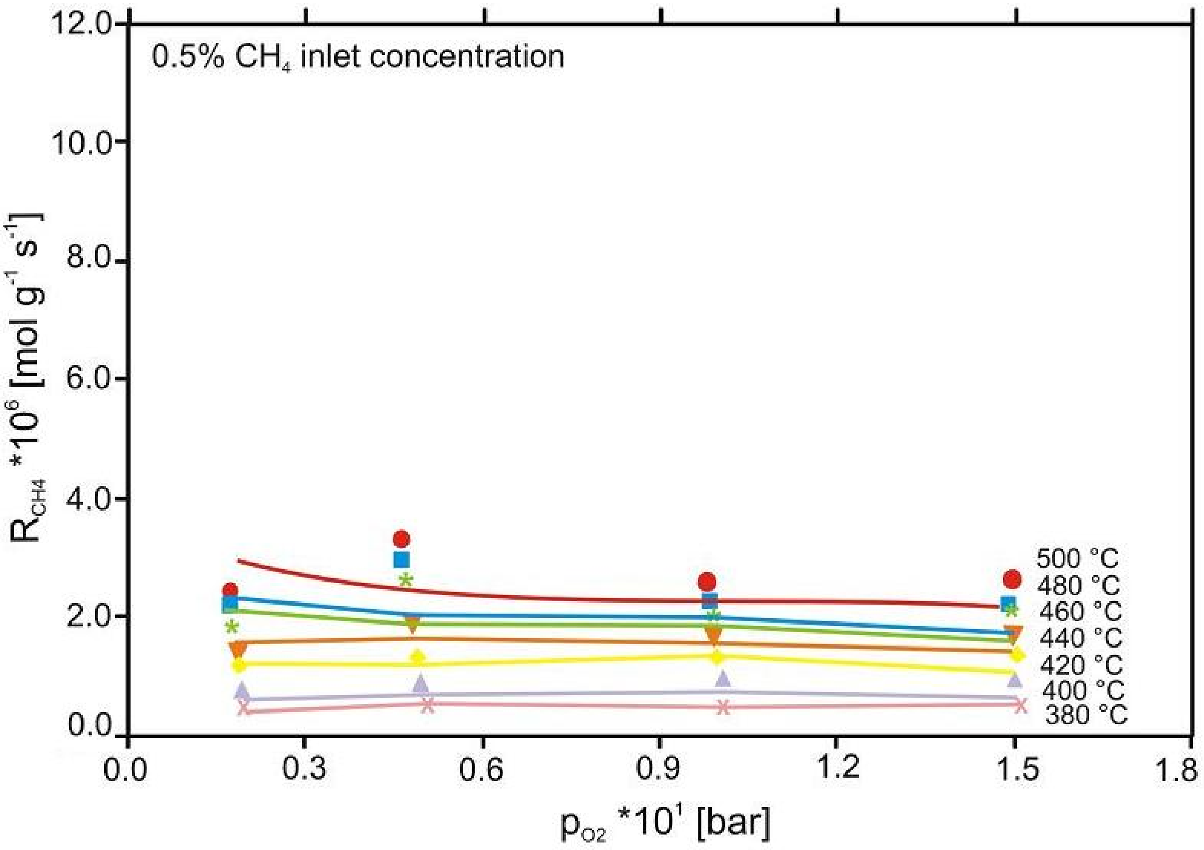

Figure 20: Reaction rate vs oxygen concentration; dots represent experiment, solid line model MVK3.

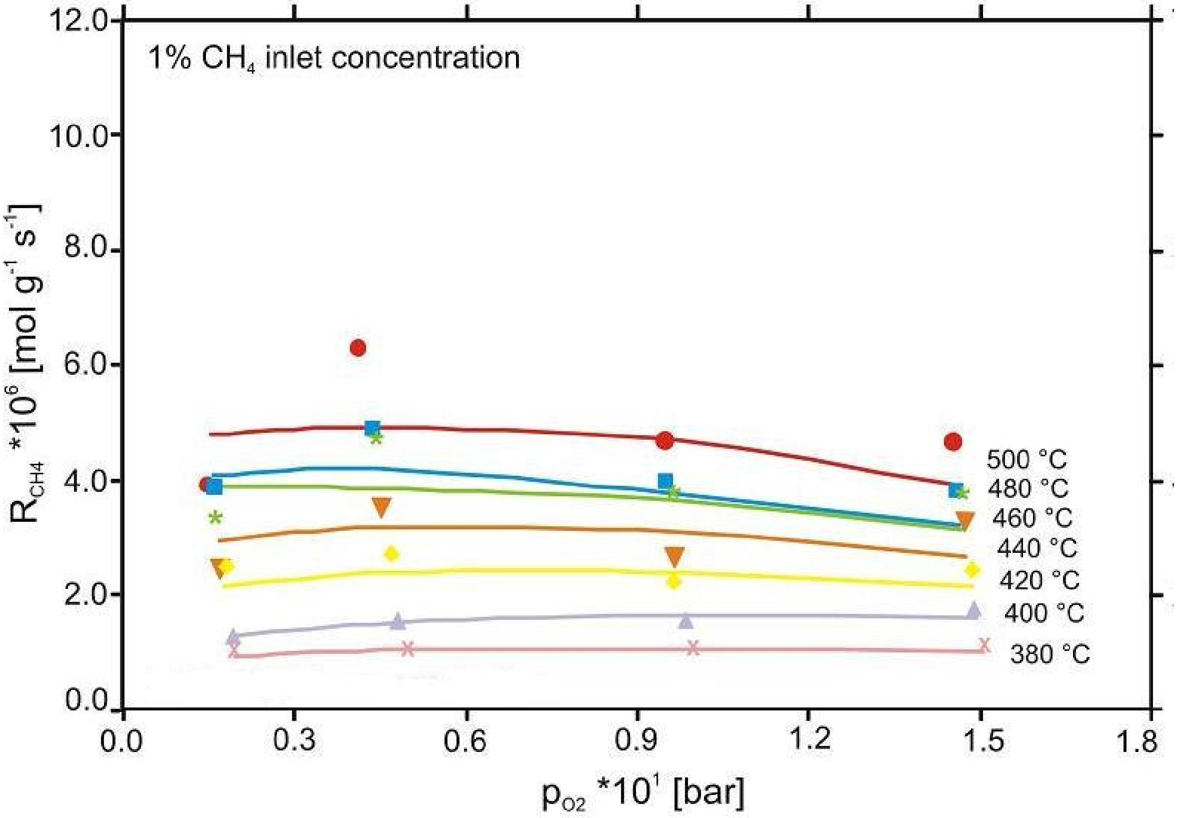

Figure 21: Reaction rate vs oxygen concentration; dots represent experiment, solid line model MVK3.

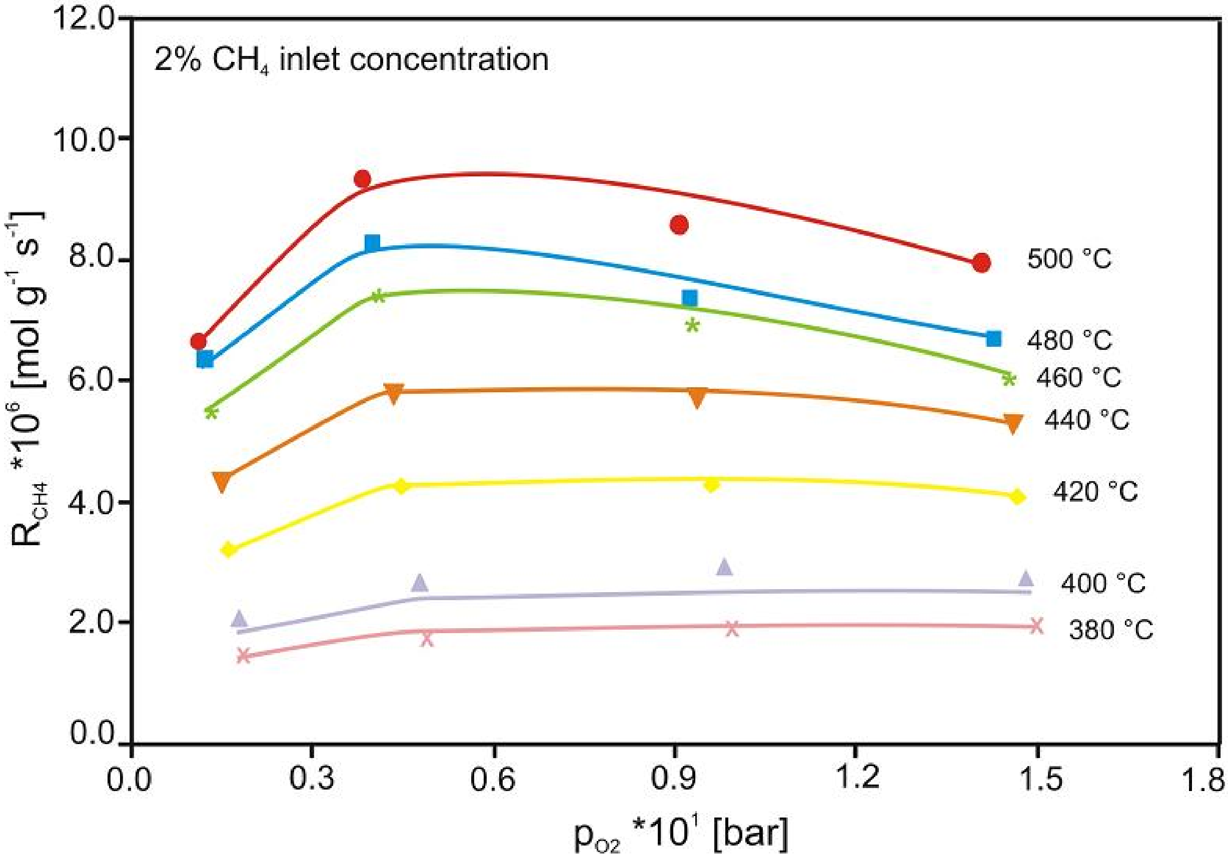

Figure 22: Reaction rate vs oxygen concentration; dots represent experiment, solid line model MVK3.

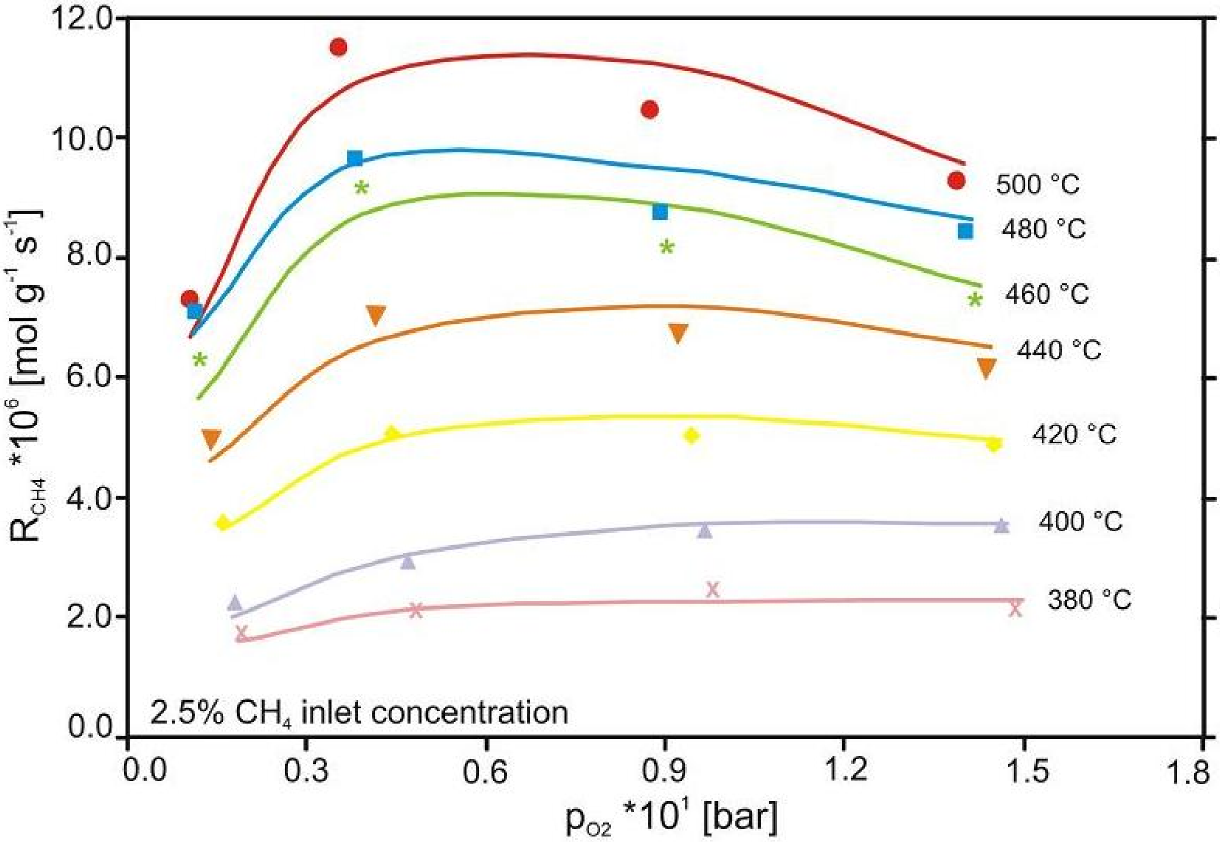

Figure 23: Reaction rate vs oxygen concentration; dots represent experiment, solid line model MVK3.

7.3.8 Undoped $Ce_{0,33}$ $Zr_{0,66}O_2$ plots

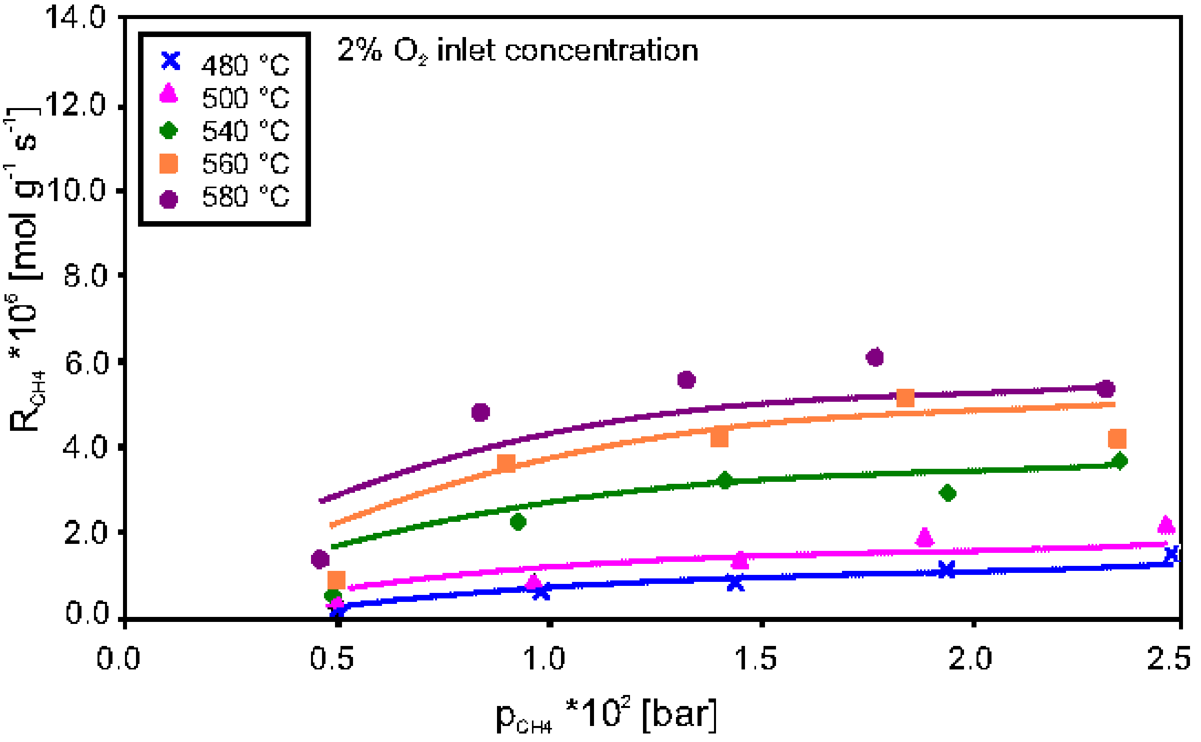

Figure 24: Reaction rate vs methane concentration; dots represent experiment, solid line model MvK1.

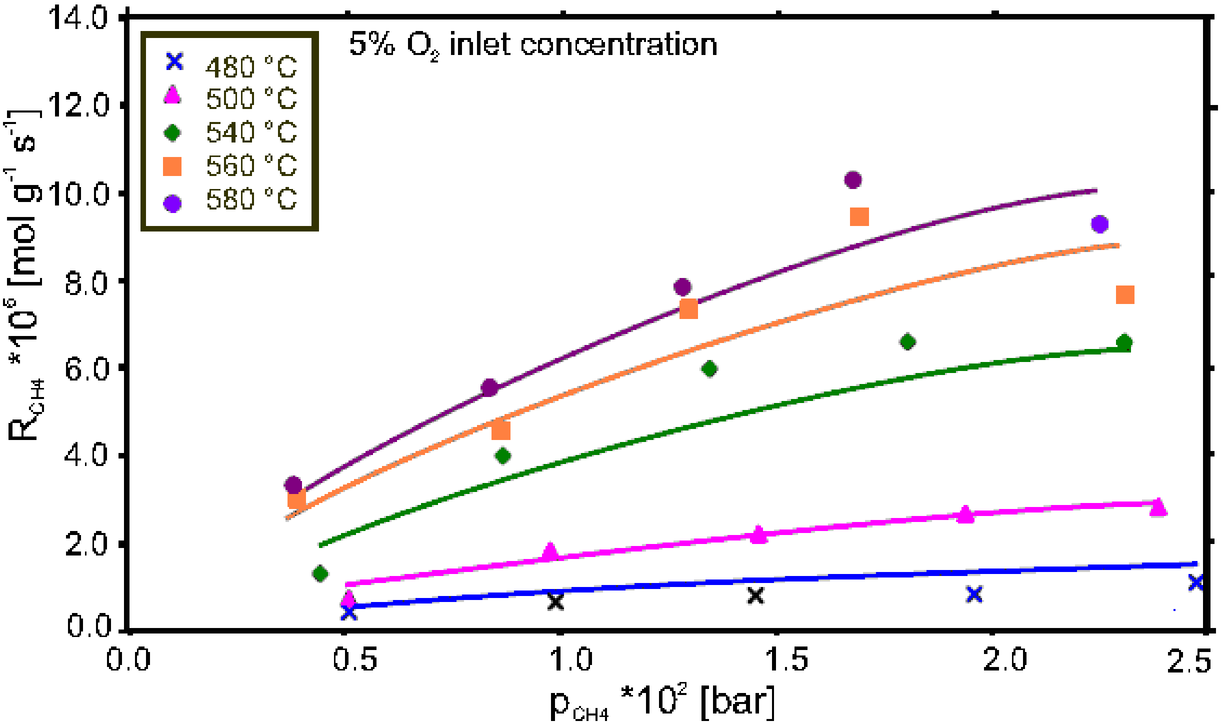

Figure 25: Reaction rate vs methane concentration; dots represent experiment, solid line model MVK1.

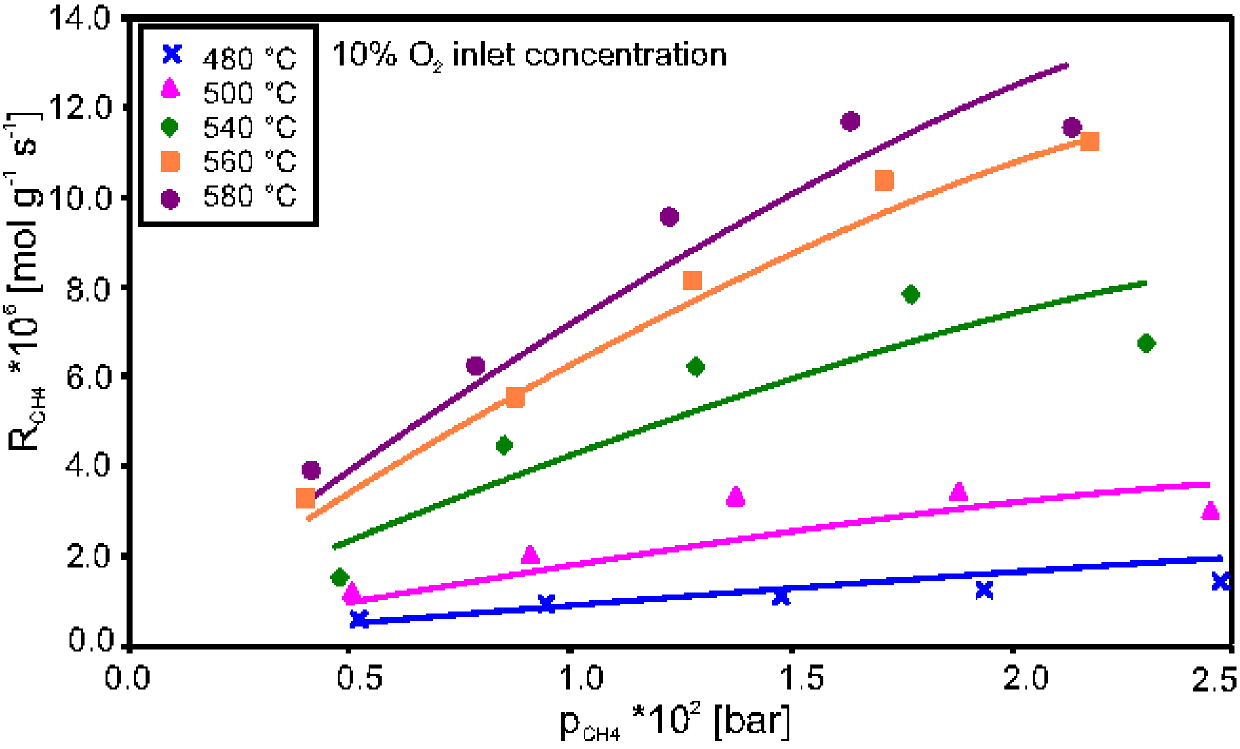

Figure 26: Reaction rate vs methane concentration; dots represent experiment, solid line model MVK1.

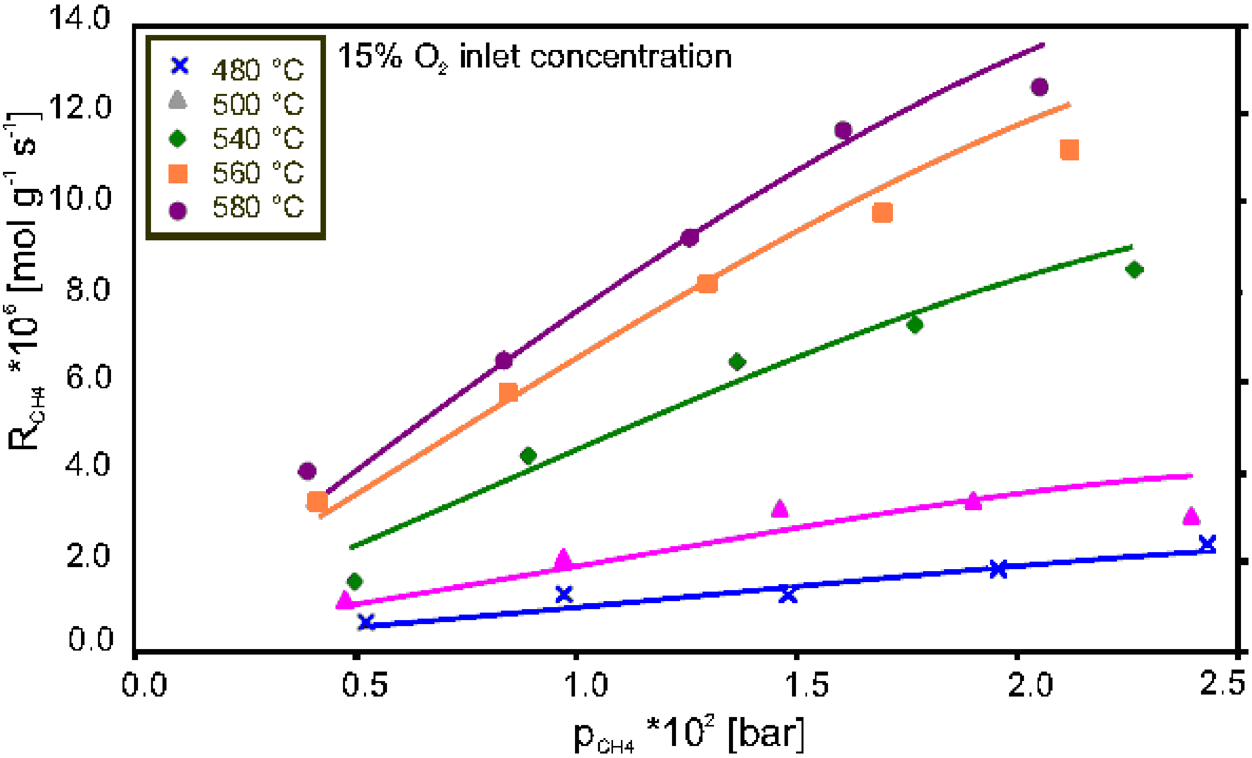

Figure 27: Reaction rate vs methane concentration; dots represent experiment, solid line model MVK1.

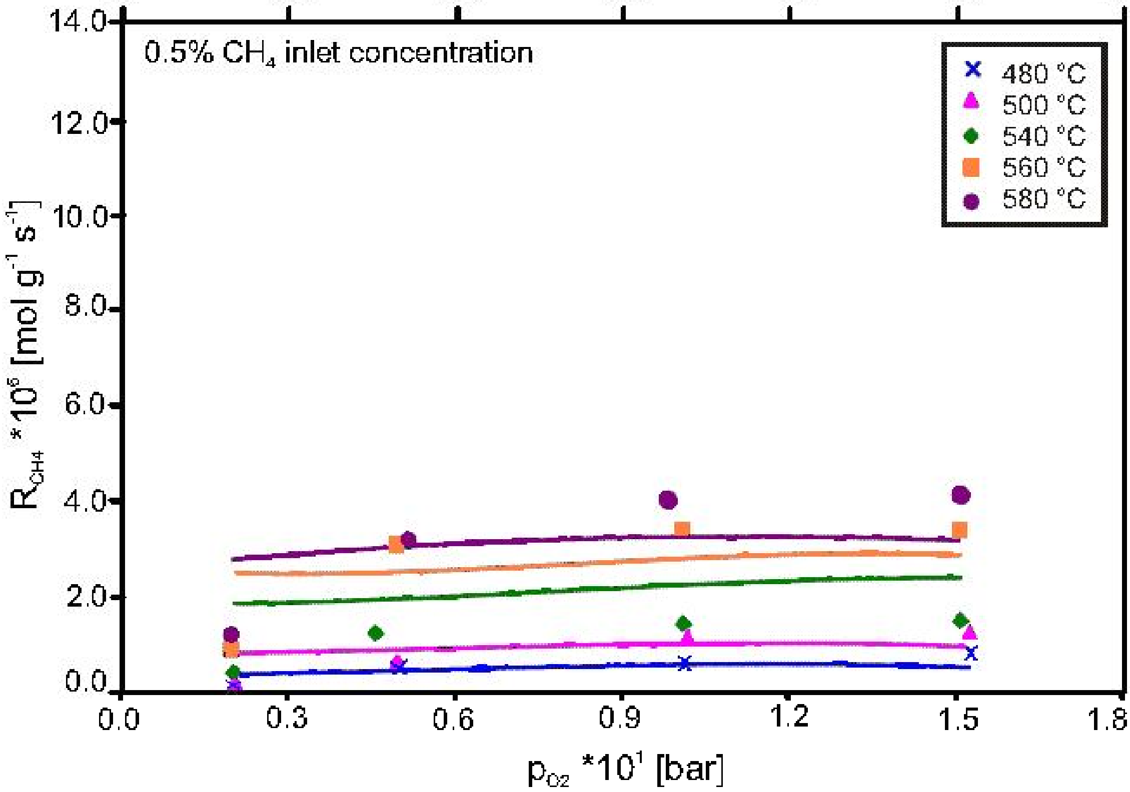

Figure 28: Reaction rate vs oxygen concentration; dots represent experiment, solid line model MVK1.

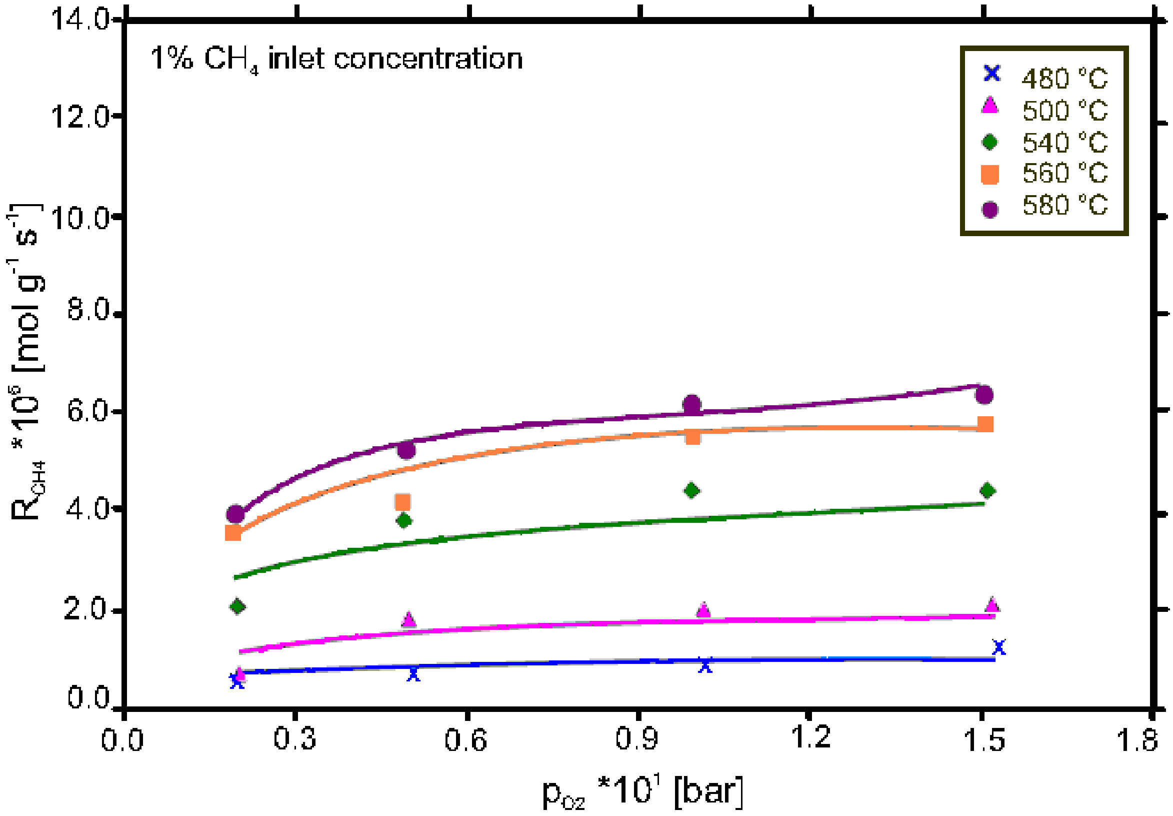

Figure 29: Reaction rate vs oxygen concentration; dots represent experiment, solid line model MVK1.

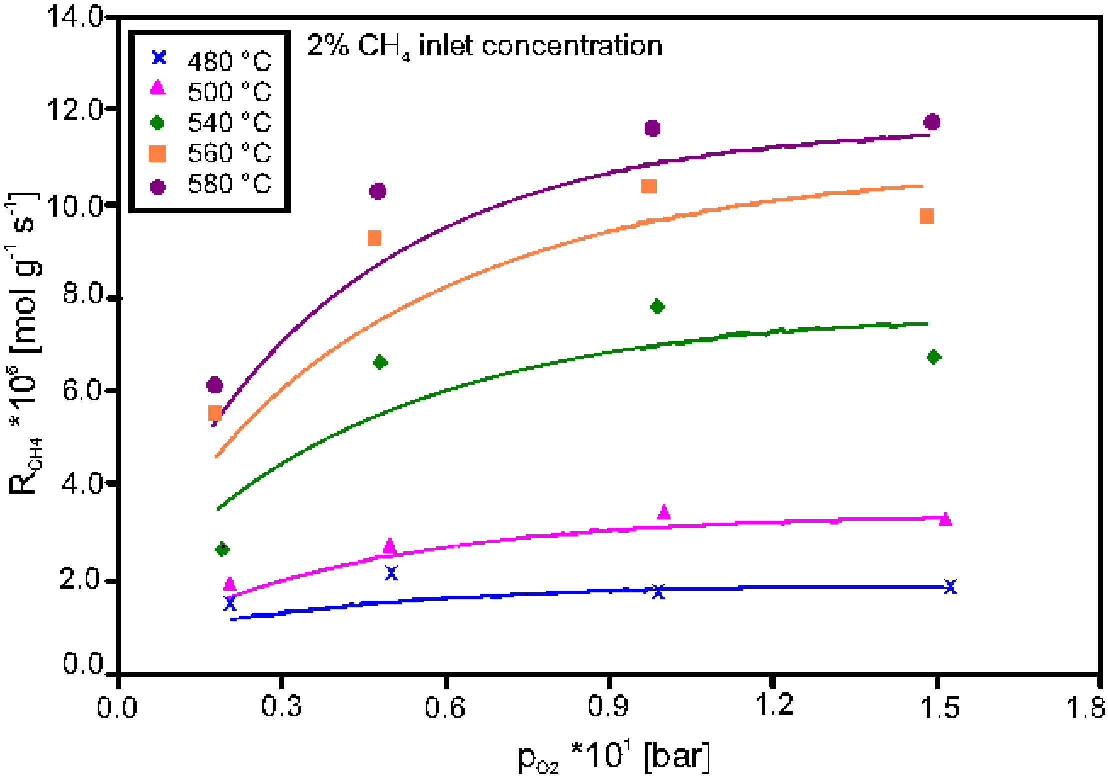

Figure 30: Reaction rate vs oxygen concentration; dots represent experiment, solid line model MVK1.

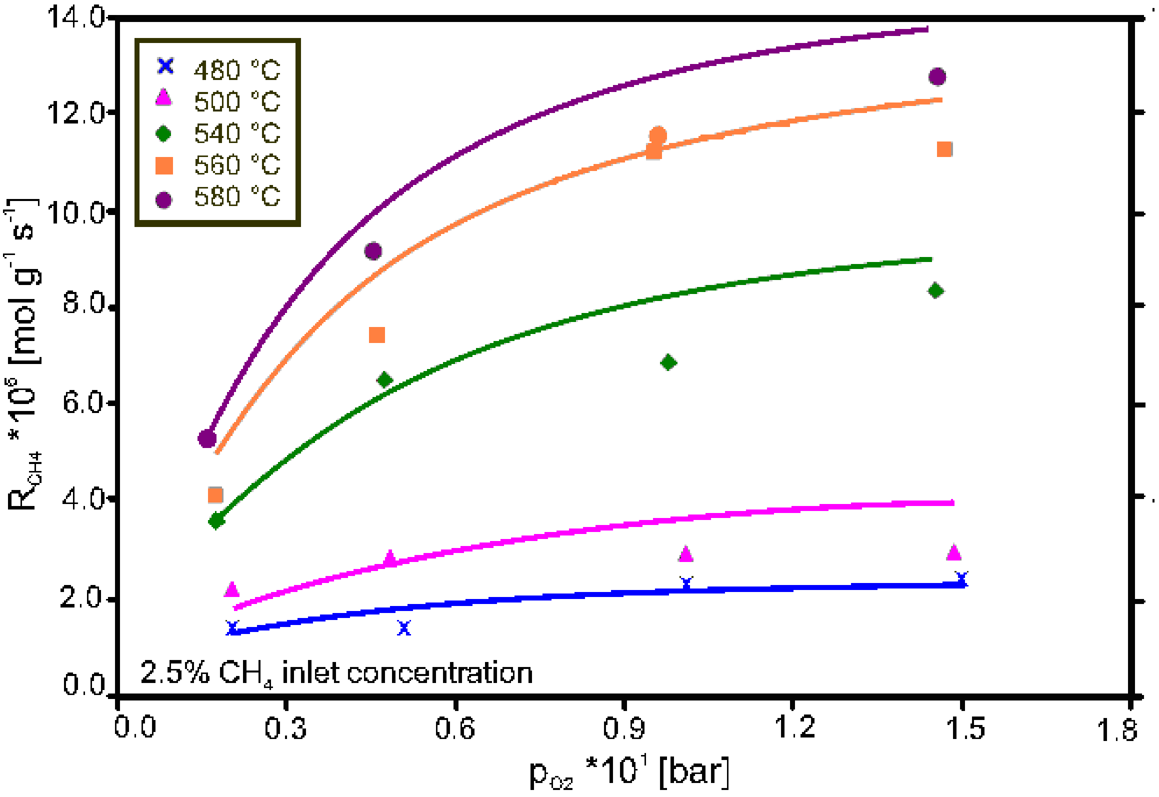

Figure 31: Reaction rate vs oxygen concentration; dots represent experiment, solid line model MVK1.

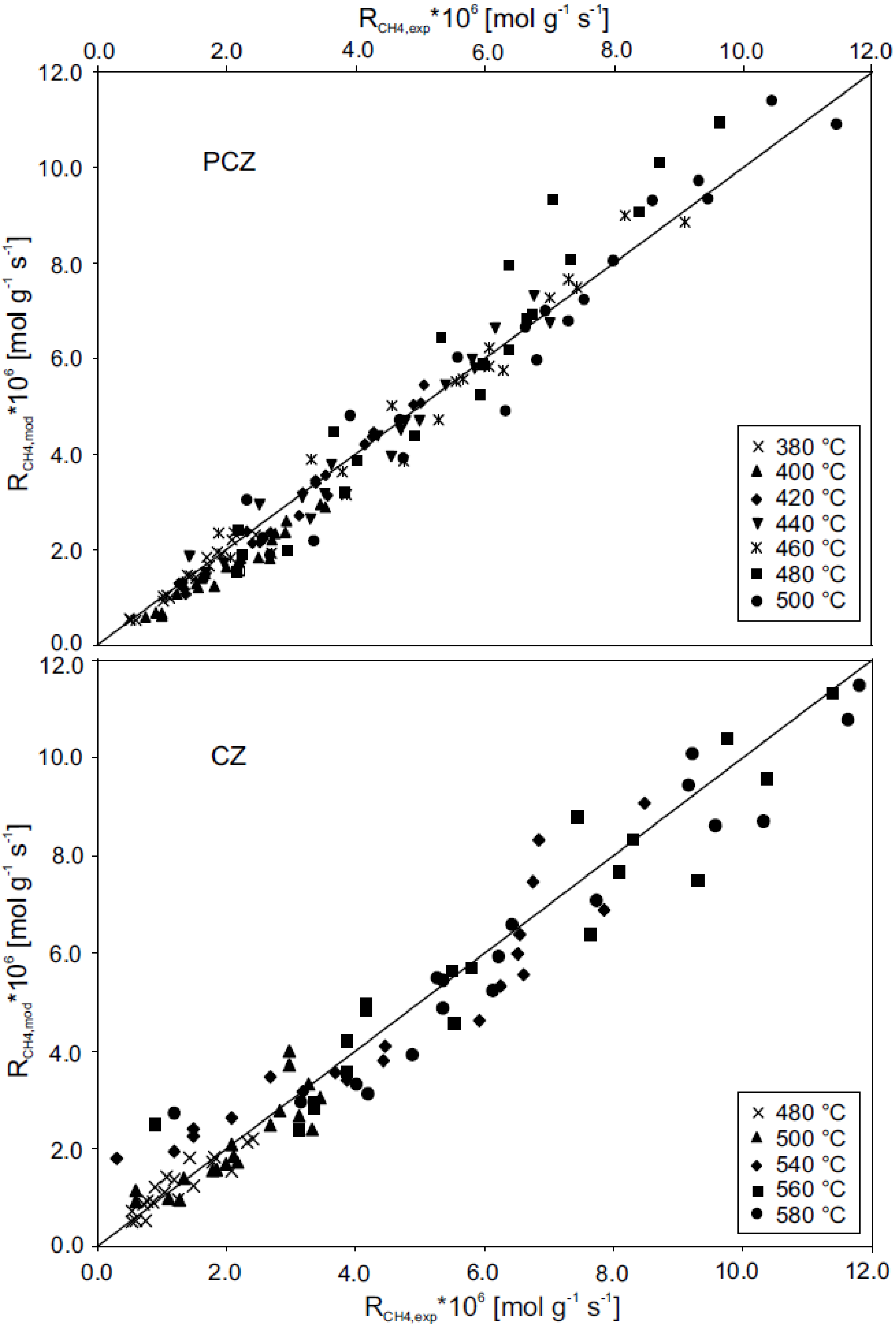

Figure 32: Parity plot used as a final check for the quality of the fitting

References for chapter 7

1) Forzatti, P.; Groppi, G. *"Catalytic combustion for the production of energy."* Catal. Today 1999, 54, 165.

2) Gélin, P.; Primet, M. *"Complete oxidation of methane at low temperature over noble metal based catalysts: a review."* Appl. Catal. B: Environ. 2002, 39, 1.

3) Specchia, S.; Civera, A.; Saracco, G. *"In situ combustion synthesis of perovskite catalysts for efficient and clean methane premixed metal burners".* Chem. Eng. Sci. 2004, 59, 5091.

4) Civera, A.; Negro, G.; Specchia, S.; Saracco, G.; Specchia, V. *"Optimal compositional and structural design for the for a $LaMnO_3/ZrO_2/Pd$-based catalyst for methane combustion".* Catal. Today 2005, 100, 275.

5) Specchia, S.; Civera, A.; Saracco, G.; Specchia, V. *"Palladium/perovskite/zirconia catalytic premixed fiber burners for efficient and clean natural gas combustion".* Catal. Today 2006, 117, 427.

6) Specchia, S.; Ahumada Irribarra, M. A.; Palmisano, P.; Saracco, G.; Specchia, V. *"Ageing of premixed metal fiber burners for natural gas combustion catalyzed with Pd/LaMnO3·2ZrO2"* Ind. Eng. Chem. Res. 2007, 46, 6666.

7) Specchia, S.; Toniato, G. *"Natural gas combustion catalysts for environmental-friendly domestic burners"* Catal. Today 2009, 147S, S99.

8) Iamarino, M.; Salatino, P.; Chirone, R.; Pirone, R.; Russo, G. *"Catalytic combustion of methane and propane in a fluidized bed reactor."* Proc. Comb. Inst. 2002, 29, 827.

9) Lee, J.; Trimm, D. *"Catalytic combustion of methane".* Fuel Process Technol. 1995, 42, 339.

10) Demoulin, O.; Navez, M.; Gaigneaux, E. M.; Ruiz, P.; Mamede, A.-S.; Granger, P.; Payen, E. *"Operando resonance Raman spectroscopic characterisation of the oxidation state of Palladium in Pd/γ-Al2O3 catalysts during the combustion of methane."* Phys. Chem. Chem. Phys. 2004, 5, 4394.

11) Seimanides, S.; Stoukides, M. *"Catalytic oxidation of methane on polycrystalline Palladium supported on stabilized zirconia."* J. Catal. 1986, 98, 540.

12) Saracco, G.; Scibilia, G.; Iannibello, A.; Baldi, G. *"Methane combustion on Mg-doped LaCrO3 perovskite catalysts".* Appl. Catal. B: Environ. 1996, 8, 229.

13) Heynderickx, P. M.; Thybaut, J. W.; Poelman, H.; Poelman, D.; Marin, G. B. *"Assessment of synergetic and precursor effects in propane total oxidation over Cu- and Ce-based catalyst."* Appl. Catal. B: Environ. 2009, 90, 295.

14) Sohrabi, M.; Bahram Dabir, B.; Eskandari, A.; Golapasha, R. D. *"Some aspect of kinetics and mechanism of the oxidative coupling of methane".* J. Chem. Tech. Biotechnol. 1996, 67, 15.

15) Groppi, G. *"Combustion of CH4 over a PdO/ZrO2 catalyst: an example of kinetic study under severe conditions".* Catal. Today 2003, 77, 335.

16) Tseng, T.; Chu, H.; Ko, T.; Chaung, L. *"The kinetic of the catalytic decomposition of methyl isobutyl ketone over a Pt/γ-Al2O3 catalyst".* Chemosphere 2005, 61, 469.

17) Garbowski, E.; Feumi-Jantou, C.; Mouaddib, N.; Primet, "*M. Catalytic combustion of methane over Palladium supported on alumina catalysts: evidence for reconstruction of particles.*" Appl. Catal. A 1994, 109, 277.

18) Hayes, R. E.; Kolaczkowsky, S. T.; Li, P. K. C.; Awdry, S. "*Evaluating the effective diffusivity of methane in the washcoat of a honeycomb monolith".* Chem. Eng. Sci. 2001, 56, 4815.

19) Hurtado, P.; Orodonez, S.; Sastre, H.; Dìez, F. V. "*Development of a kinetic model for the oxidation of methane over Pd/Al2O3 at dry and wet conditions".* Appl. Catal. B: Environ. 2004, 51, 229.

20) Auer, R.; Warnier, L.; Thyrion, F. C. "*Kinetic study of methane combustion over* $La_{0.9}Ce_{0.1}CoO_3$*."* Stud. Surf. Sci. Catal. 2001, 133, 599.

21) Vella, L. D.; Burelli, S.; Specchia, S.; Saracco, G.; Specchia, V. "*Microcombustion of CH4/H2/air misture".* Proceedings of the XXXI Event of The Italian Section of The Combustion Institute, Torino, Italy, I-6, 2008.

22) Specchia, S.; Vella, L. D.; Burelli, S.; Saracco, G.; Specchia, V. "*Combustion of CH4/H2/air mixtures in catalytic microreactors".* Chem. Phys. Phys. Chem. 2009, 10, 783.

23) Boaro, M.; Vicario, M.; de Leitenburg, C.; Dolcetti, G.; Trovarelli, A. "*The use of temperature-programmed and dynamic/transient methods in catalysis: characterization of ceria-based, model three-way catalysts".* Catal. Today 2003, 77, 407.

24) Fornasiero, P.; Dimonte, R.; Rao, G.; Kašpar, J.; Meriani, S.; Trovarelli, A., Graziani, M. "*Rh-loaded CeO2-ZrO2 solid-solutions as highly efficient oxygen exchangers - dependence of the reduction behavior and the oxygen storage capacity on the structural-properties".* J. Catal. 1995, 151, 168.

25) Kašpar, J.; Fornasiero, P.; Graziani, M. Use of *"CeO2-based oxides in the three-way catalysis".* Catal. Today 1999, 50, 285.

26) Specchia, S.; Finocchio, E.; Busca, G.; Palmisano, P.; Specchia, V. *"Surface chemistry and reactivity of ceria–zirconia-supported Palladium oxide catalysts for natural gas combustion."* J. Catal. 2009, 263, 134.

27) Fornasiero, P.; Di Monte, R.; Montini, T.; Kašpar, J.; Graziani, M. "*Thermal stability and oxygen storage capacity of noble metal/ceria-zirconia catalysts for the automotive converters with the on-board-diagnostics (OBD)".* Stud. Surf. Sci. Catal. 2000, 130, 1355.

28) Mamontov, E.; Brezny, R.; Koranne, M.; Egami, T. *"Nanoscale heterogeneities and oxygen storage capacity of* $Ce_{0.5}$ $Zr_{0.5}O_2$*."* J. Phys. Chem. B 2003, 107, 13007.

29) Rajasree, R.; Hoebink, J. H. B. J.; Schouten, J. C. *"Transient kinetics of carbon monoxide oxidation by oxygen over supported Palladium/ceria/zirconia three-way catalysts in the absence and presence of water and carbon dioxide."* J. Catal. 2004, 223, 36.

30) Fornasiero, P.; Montini, T.; Graziani, M.; Zilio, S.; Succi, *"M. Development of functionalized Fe-Al-Cr alloy fibers as innovative catalytic oxidation devices".* Catal. Today 2008, 137, 475.

31) Di Monte, R.; Kašpar, J.; Fornasiero, P.; Graziani, M.; Paze, C.; Gubitosa, G. *"NO reduction by CO over Pd/Ce0.6Zr0.4O2-Al2O3 catalysts: in situ FT-IR studies of NO and CO adsorption".* Inorg. Chim. Acta 2002, 334, 318.

32) Atribak, I.; Bueno-López, A.; García-García, A. “*Thermally stable ceria–zirconia catalysts for soot oxidation by O2”*. J. Catal. 2008, 259, 123.

33) Hosseinpour, N.; Khodadadi, A. A.; Mortazavi, Y.; Bazyari, A. “*Nano-ceria–zirconia promoter effects on enhanced coke combustion and oxidation of CO formed in regeneration of silica–alumina coked during cracking of triisopropylbenzene”*. Appl. Catal. A: Gen. 2009, 353, 271.

34) Di Monte, R.; Kašpar, J.; Fornasiero, P.; Ferrero, A.; Gubitosa, G.; Graziani, M. *“NO reduction by CO over Pd/CeO2-ZrO2-Al2O3”*. Stud. Surf. Sci. Catal. 1998, 116, 559.

35) Thomas, C.; Gorce, O.; Fontaine, C.; Krafft, J.-M.; Villain, F.; Djéga-Mariadassou, G. *“On the promotional effect of Pd on the propene-assisted decomposition of NO on chlorinated* $Ce_{0.68}Zr_{0.3}2O_2$*”* Appl. Catal. B Environ. 2006, 63, 201.

36) Di Monte, R.; Fornasiero, P.; Kašpar, J.; Rumori, P.; Gubitosa, G.; Graziani*, “M. Pd/Ce0.6Zr0.4O2/Al2O3 as advanced materials for three-way catalysts: Part 1. Catalyst characterisation, thermal stability and catalytic activity in the reduction of NO by CO”*. Appl. Catal. B: Environ. 2000, 24, 157.

37) Hickey, N.; Fornasiero, P.; Di Monte, R.; Kašpar, J.; Gonzalez-Velasco, J. R.; Gutierrez-Ortiz M. A.; Gonzalez-Marcos, M. P.; Gatica, J. M.; Bernal, S. *“Reactivation of aged model Pd/Ce0.68Zr0.32O2 three-way catalyst by high temperature oxidising treatment”*. Chem. Comm. 2004, 10, 196.

38) Specchia, S.; Finocchio, E.; Busca, G.; Specchia V. *Handobook of Combustion, Volume 5: New Technologies, Chapter 17: Combustion synthesis.* Wiley-VCH Verlag GmbH & Co. KGaA: Weinheim, 2010.

39) De Rogatis, L.; Cargnello, M.; Gombac, V.; Lorenzut, B.; Montini, T.; Fornasiero, P. “*Embedded phases: a way to active and stable catalysts”*. Chem. Sus. Chem. 2010, 3, 24.

40) Sánchez Escribano, V.; Fernández López, E.; Panizza, M.; Resini, C.; Gallardo Amores, J. M.; Busca, G. *“Characterization of cubic ceria–zirconia powders by X-ray diffraction and vibrational and electronic spectroscopy”*. Solid State Sci. 2003, 5, 1369.

41) Montini, T.; Speghini, A.; De Rogatis, L.; Lorenzut, B.; Bettinelli, M.; Graziani, M.; Fornasiero, P. *“Identification of the structural phases of CexZr1-xO2 by Eu(III) luminescence studies”,* J. Am. Chem. Soc. 2009, 131, 13155.

42) Farrauto, R. J.; Lampert, J. K.; Hobson, M. C.; Waterman, E. M. *“Thermal-decomposition and reformation of PdO catalysts - support effects.”* Appl. Catal. B: Environ. 1995, 6. 263.

43) Beguin, B.; Garbowski, E.; Primet, M. *“Stabilization of alumina by addition of lanthanum.”* Appl. Catal. 1991, 75, 119.

44) McCarty, J. G. *“Kinetics of PdO combustion catalysis”*. Catal. Today 1995, 26, 283.

45) Kleykamp, K. *“Freie Bildungsenthalpie von Palladiumoxid”*. Z. Phys. Chem. N.F. 1970, 71, 142.

46) Kan, H. H.; Shumbera, R. B.; Weaver, J. F. *“Growth and properties of high-concentration phases of atomic oxygen on platinum single crystal surfaces”*. Surf. Sci. 2008, 602, 1337.

47) Fornasiero, P.; Kašpar, J.*; "Graziani, M. Redox behaviour of high surface area Rh-loaded Ce0.5Zr0.5O2 mixed oxide".* J. Catal. 1997, 167, 576.

48) Balducci, G.; Kašpar, J.; Fornasiero, P.; Graziani M.; Islam, M. S. *"Surface and reduction energetics of the CeO2-ZrO2 catalysts".* J. Phys. Chem. B 1998, 102, 557.

49) Gennari, F. C.; Neyertz, C.; Meyer, G.; Montini, T.; Fornasiero, P. *"Hydrogen adsorption kinetics on Pd/$Ce_{0.8}Zr_{0.2}O_2$."* Phys. Chem. Chem. Phys. 2006, 8, 2385.

50) Fornasiero, P.; Kašpar, J.; Sergo, V.; Graziani, M. *"Redox behavior of high-surface-area Rh-, Pt-, and Pd-loaded $Ce_{0.5}Zr_{0.5}O_2$ mixed oxide".* J. Catal. 1999, 182, 56.

51) Gatica, J. M.; Baker, R. T.; Fornasiero, P.; Bernal, S.; Kašpar, J. "*Characterization of the metal Phase in NM/$Ce_{0.68}Zr_{0.32}O_2$ (NM: Pt and Pd) catalysts by hydrogen chemisorption and HRTEM microscopy: a comparative study."* J. Phys. Chem. B 2001, 105, 1191.

52) Carberry, J. J. "*Catalysis: Science and Technology",* Springer-Verlag: Berlin, 1987.

53) Arai, H.; Yamada, T.; Eguchi, K.; Seiyama, T. "*Catalytic combustion of methane over various perovskite-type oxides".* Appl. Catal. A 1986, 26, 265.

List of symbols and acronyms for chapter 7

ER= Eley Rideal kinetic model
LH= Langmuir Hinshelwood kinetic model
MVK= Mars van Krevelen kinetic model
PCZ = Palladium doped Ce0,33 Zr0,66O2 catalyst
CZ = Ce0,33 Zr0,66O2 catalyst
SCS = Simultaneous Combustion Synthesis
EDX = Energy-dispersive X-ray spectroscopy
SEM= scanning electron microscope
TPD, R, O = Temperature Programmed Desorption , Reduction, Oxidation : respectively
TCD= Thermal Conductibility Detector
TPC = Temperature programmed combustion
F= molar total flow (mol/s)
ΔCH4= defined as (mol. frac CH4 in) –(mol frac ch4 out)
R_{CH4}= methane reaction rate (mol/s)
Kx= equilibrium constant
kx = kinetic constant
px = partial pressure of component x
θ= active site
E =Activation energy
R = Universal gas constant 8,314472 (J K^{-1} mol^{-1})

8 Lanthanum manganite catalyst

8.1 Overview and production

Perovskites have been studied for a long time for the combustion of VOC [1] with good results but higher efforts are needed to reach high conversion rates for methane combustion due to the higher stability of the molecule.

While [1] obtained significant results in CH_4 oxidation using cerium doped lanthanum cobaltite in this thesis researching on lanthanum manganite was preferred because of the low toxicity of the compound.

The effectiveness of various synthesis methods for $LaMnO_3$ and for $LaCoO_3$ was discussed by [2] who tested various techniques including flame hydrolysis[3,4], sol-gel method, EDTA complexation [5] and ball milling.

They concluded that sol gel and flame hydrolysis were the most suited technologies for perovskite synthesis and that flame hydrolysis led to a catalyst with more durable performances.

Microwave assisted hydrothermal synthesis was the strategy adopted by [6,7] to produce $La_{(1-x)}B_xMnO_{3.15}$ perovskites (B = Sr, Ag; x = 0 or 0.2) for CH_4 combustion.

Silver doping revealed to be very effective reducing by more about 80°C the temperature of half reaction: in this case the substitution of some lanthanum with silver increases the oxidation number of manganese because it is an element with high electro negativity that can’t be oxidized above +1 state.

By using Ba instead of Sr and applying Pechini technique instead of microwave assisted hydrothermal synthesis [8] found similar effect

Further confirmation of the positive effect of Mn in the 4^+ state are reported by [9,10] in particular [9] which synthesized a $Pr_xSr_{1-x}MnO_3$ perovskite linked this beneficial effect to the fact that smaller Mn^{4+} ions give more room to oxygen atoms to diffuse.

$LaMn_xMg_{(1-x)}O_3$ synthesized by [11] al focused on doping the perovskite structure adding magnesium to the B site of the crystalline structure (general formula of perovskites is ABO_3): this action again shifted the oxidation state of manganese towards 4^+ therefore increasing the catalytic capabilities at low temperature.

Performing a detailed kinetical analysis he concluded that Mg doping created a new kind of oxygen species that was very active and that was detectable also un the oxygen TPD.

Daturi et al. [12] synthesized a special perovskite based on titania which incorporates also zirconium and manganese: this structure is well suited to outstand high temperature for higher time than lanthanum manganite because titanates have higher fusion temperature and retain longer their original specific surface area.

The paper concludes remarking that zirconium addition increases further surface area while catalytic activity is imputable to Mn^{4+}.

Instead of intrinsically doping the catalyst crystal, our research team, following the paper of [13] decided to focus on structural promotion to overcome the small surface area that affects every perovskite prepared by solution combustion synthesis SCS: for this reason zirconium oxide was used to give a backbone onto which the perovskite could expand its surface.

The SCS method consists in weighting all the reagents and dissolving them in the proper amount of water: then the solution is put in a capsule which in turn is deposited in a furnace at 500°C for some minute.

The principal difference between this paper’s synthesis technique and the literature [13] is that in this case Palladium nitrate was dissolved directly into the mixture and that an excess of glycine was used.

This kind of one shot synthesis proved to be very effective in enhancing Palladium dispersion and catalyst activity.

Reagent name	Formula	Quantity per gram of catalyst
Zirconium Oxynitrate	ZrO(NO3)2_6H2O	**1,390 g**
Lanthanum Nitrate	La(NO3)3_6H2O	**0,887 g**
Manganese Nitrate	Mn(NO3)2_4H2O	**0,514 g**
Palladium Nitrate	10% solution H2O	**0,433 g**
Glycine	COOH.CH2.NH2	**1,504 g**

Table 7: Reagents for 1gr of 2% Pd/ $LaMnO_3$•$2ZrO_2$

After the reaction the powder obtained was calcined at 800°C for 2 hours in calm air to remove residual carbon (due to glycine excess).

8.2 Basic characterization

As seen on Figure 34 the activity of the catalyst doped with Palladium is characterized by a valley when the temperature programmed combustion is carried from high to low temperatures: this is almost surely linked to the fact that Palladium undergoes changes in its crystalline structure and in its superficial oxidation state. These unconventional features have been reported also by 14, 15, 16 who link the drop and rebound of palladium activity to a slow PdO_x formation and decomposition.

Beside these considerations the temperature of half conversion is between 500 and 550°C

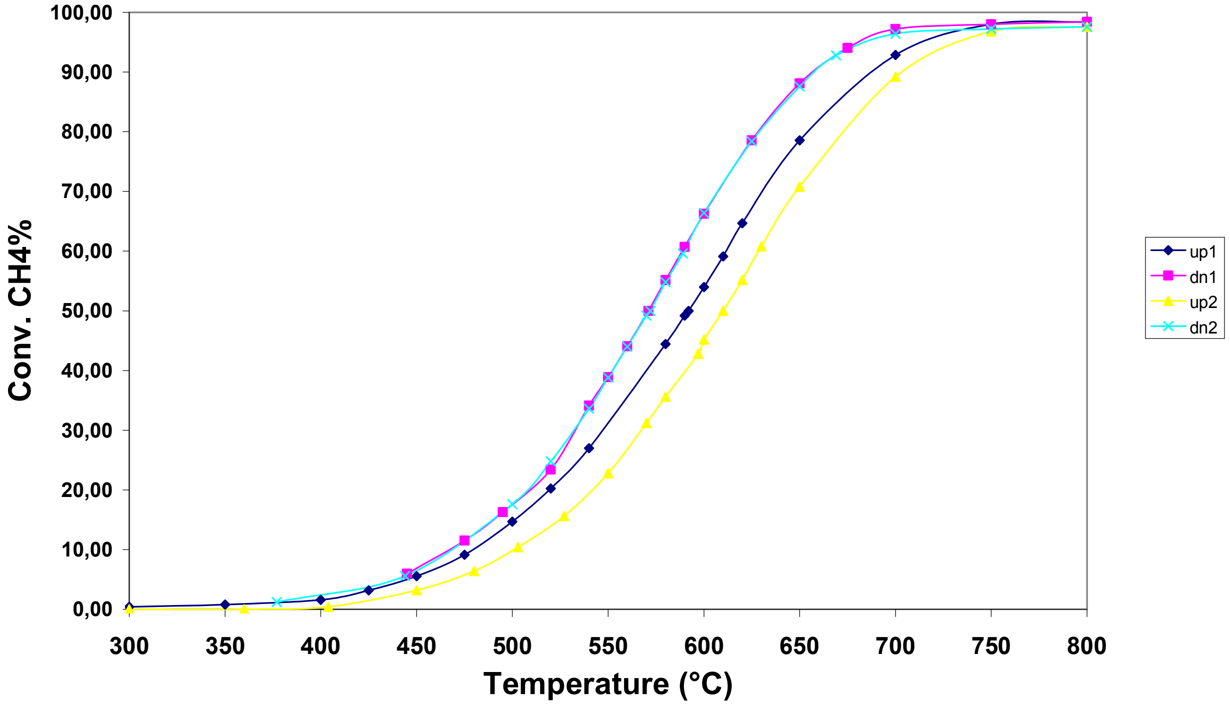

Figure 33: Temperature programmed combustion on $LaMnO_3$•$2ZrO_2$

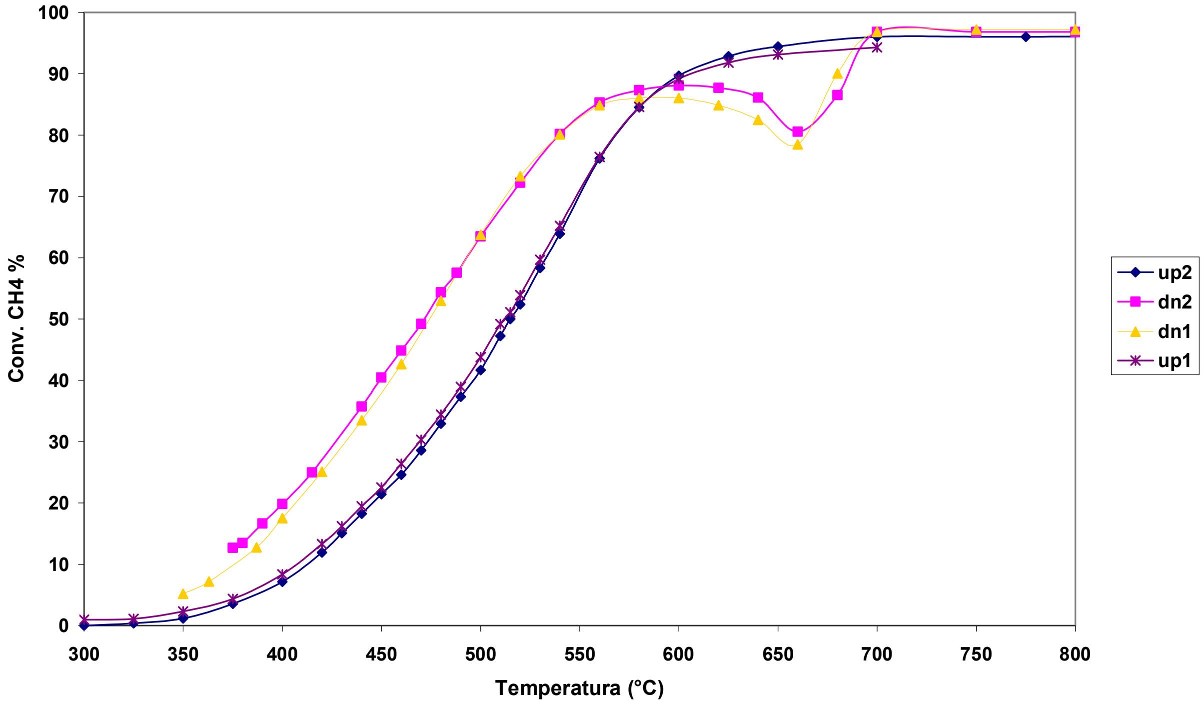

Figure 34: Temperature programmed combustion on 2%Pd/ $LaMnO_3$•$2ZrO_2$

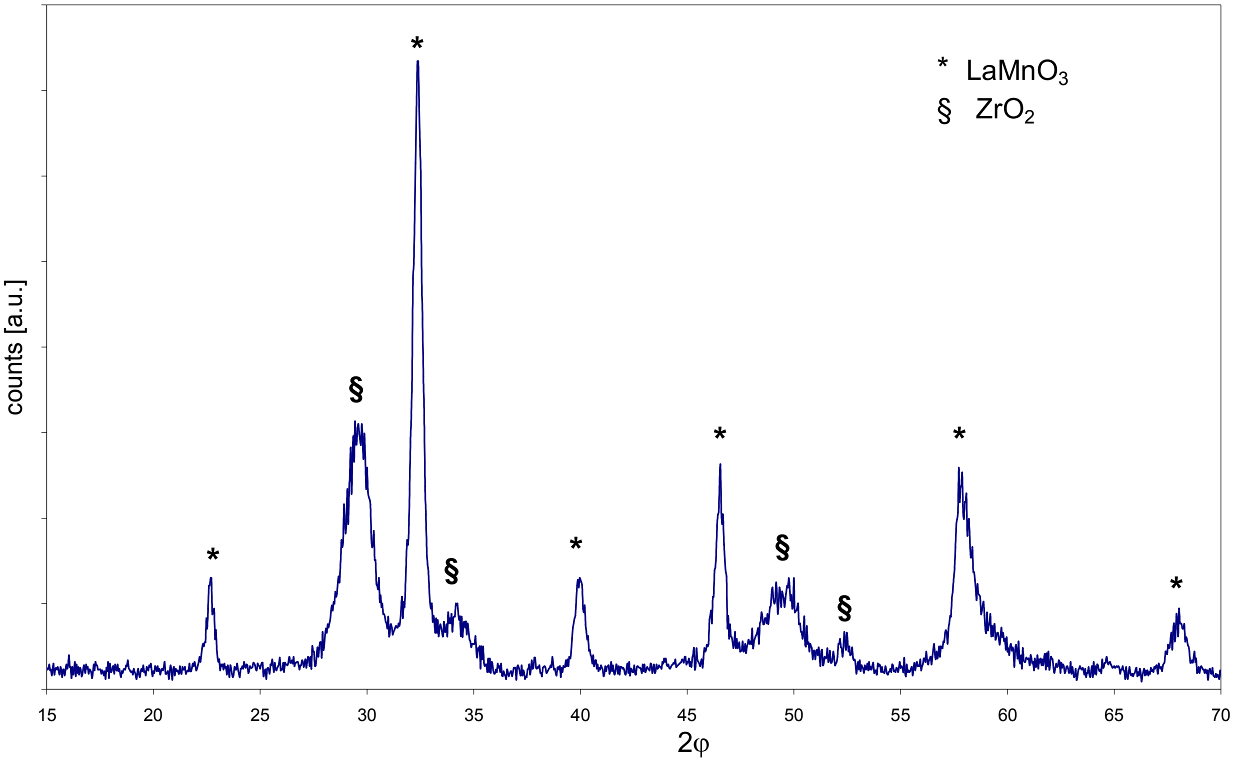

Figure 35: XRD spectrum of lanthanum manganate + zirconia. The two phases are separated

8.3 Detailed kinetic analysis of undoped and doped LaMnO$_3$/2ZrO$_2$

Using the same experimental apparatus described in chapter five and applying the same automatic analysis technique described in the appendix we compiled a table of best fitting kinetic parameters for the models we tested.

From the equations present in literature and reported in table 3 it was chosen to test only Mars van Krevelen and Langmuir Hinshelwood models because in the previous chapter the poor performance of Eley Rideal models was showed.

		MvK1	MvK2	**MvK4**
LaMnO$_3$/2ZrO$_2$	E_ox (J/mol/K)	1,674E+05	1,070E+05	1,653E+05
	k_inf_ox (mol/bar/g/s)	1,145E+06		9,498E+05
	k_infox (mol/bar^{0,5}/g/s)		1,832E+01	
	E_met (J/mol/K)	7,867E+04	7,395E+04	7,672E+04
	k_inf_met (mol/bar/g/s)	1,005E+00	6,353E-01	8,950E-01
	E_diss (J/mol/K)			5,124E+04
	K_inf_diss (mol/g/s)			2,227E-03
	Square error mol^2/s^2	1,573E-14	9,311E-15	**1,428E-14**
Pd/LaMnO$_3$/2ZrO$_2$	E_ox (J/mol/K)	1,703E+05	1,365E+05	1,946E+05
	K_inf_ox (mol/bar/g/s)	2,974E+07		2,194E+09
	k_inf_ox (mol/bar^{0,5}/g/s)		1,082E+04	
	E_met (J/mol/K)	8,845E+04	8,106E+04	9,968E+04
	k_inf_met (mol/bar/g/s)	8,594E+00	3,123E+00	7,396E+01
	E_diss (J/mol/K)			4,335E+04
	k_inf_diss (mol//g/s)			3,500E-04
	Square error (mol^2/s^2)	2,846E-14	2,762E-14	**2,092E-14**

Table 8: Results of Mars van Krevelen models for doped and undoped LaMnO$_3$/2ZrO$_2$.

		LH1	LH2	LH3	LH4
$LaMnO_3/2ZrO_2$	E_{cin}(J/mol/K)	1,309 E5	1,345 E5	8,037 E4	
	$k_{\infty\ cin}$ (mol/g/s)	607,7	984,6	0,7104	
	ΔH_{o2}(J/mol/K)	*2,534 E4*	*7,557 E4*	*1,97 E4*	
	$K_{\infty o2}$(bar^{-1})	581,8	2,467 E5	639,4	
	ΔH_{ch4}(J/mol/K)	-5,162 E4	-6,528 E4	*6,271 E3*	
	$K_{\infty ch4}$(bar^{-1})	8,671 E-3	1,333 E-3	37,05	
	Square error (mol^2/s^2)	4,902 E-14	1,45 E-14	7,98 E-14	
$Pd/LaMnO_3/2ZrO_2$	E_{cin}(J/mol/K)	1,19 E5	6,785 E4		6,785 E4
	$k_{\infty\ cin}$ (mol/g/s)	386,3	7,868 E-3		0,1248
	ΔH_{o2}(J/mol/K)	*2,936 E4*	*1,085 E5*		*7,394 E4*
	$K_{\infty o2}$(bar^{-1})	2,24 E3	5,4 E8		1,117 E7
	ΔH_{ch4}(J/mol/K)	-3,008 E4	*4,186 E4*		*2,951 E4*
	$K_{\infty ch4}$(bar^{-1})	0,1275	2,14 E4		2,612 E3
	Square error (mol^2/s^2)	1,281 E-14	2,032 E-14		2,18 E-14

Table 9: Results of Langmuir Hinschelwood models for doped and undoped $LaMnO_3/2ZrO_2$

For what concerns the Langmuir Hinschelwood models 4 and 3 applied respectively to the $LaMnO_3/2ZrO_2$ and to the $Pd/LaMnO_3/2ZrO_2$ the least square algorithm converged just for too few gas composition to perform the final analysis step in a reliable way.

The same problem affected The Mars van Krevelen model n°3 and prevented us from completing the parameter fitting procedure.

Differently from Ce,ZrO_2 and $Pd/Ce,ZrO_2$ catalysts tables 8 and 9 report the mean of the square errors instead of their sum.

When fitting a Langmuir Hinshelwood model a physical constrain must be checked: the heat of adsorption must be exothermic because an adsorbed species has less degree of freedom than a gaseous one.

For this reason in table 9 the heats of adsorption that resulted endothermic were reported underlined and the model was no more considered as a fitting candidate.

8.3.1 Palladium unique properties

Another feature that must be noted is that, when dealing with Pd/$LaMnO_3$/$2ZrO_2$ all the models misbehave around the stoichiometric point; the reason of that phenomenon must be researched by looking at the axioms laying at the base of the Arrhenius theory.

One of them is that the catalytic site must not change in nature when varying the reacting mixture composition.

Instead the gas mixture of the carried out experiments shifted from very lean to rich and during the process the Palladium oxide was reduced to Palladium metal: the peak of activity of our catalyst is therefore easily explainable because when λ was equal to 1 the stable Palladium phase consisted of a single layer of Palladium oxide on a core of metallic Palladium

This phase was reported by many authors as the most active form of Palladium and for the same reason Otto engines are electronically adjusted to λ=1 in order to maximize the catalytical capabilities of the off gas converter (which is based on Palladium).

This is the reason why every model tested using Pd/$LaMnO_3$/$2ZrO_2$ shows a serious inaccuracy when confronted with 5% oxygen mixtures (molar basis): where kinetics has a spike up due to catalyst modification the model registers a lower reactant concentration and miscalculates reaction rates (with a spike down).

For the same reason it seems that the addition of Palladium increases the activation energy of the catalyst: but looking at the Figure 36 it can be noted an abrupt increase in catalyst activity at the temperature of 525°C that is about the same above which anomalous spike-up becomes evident for stoichiometric mixtures.

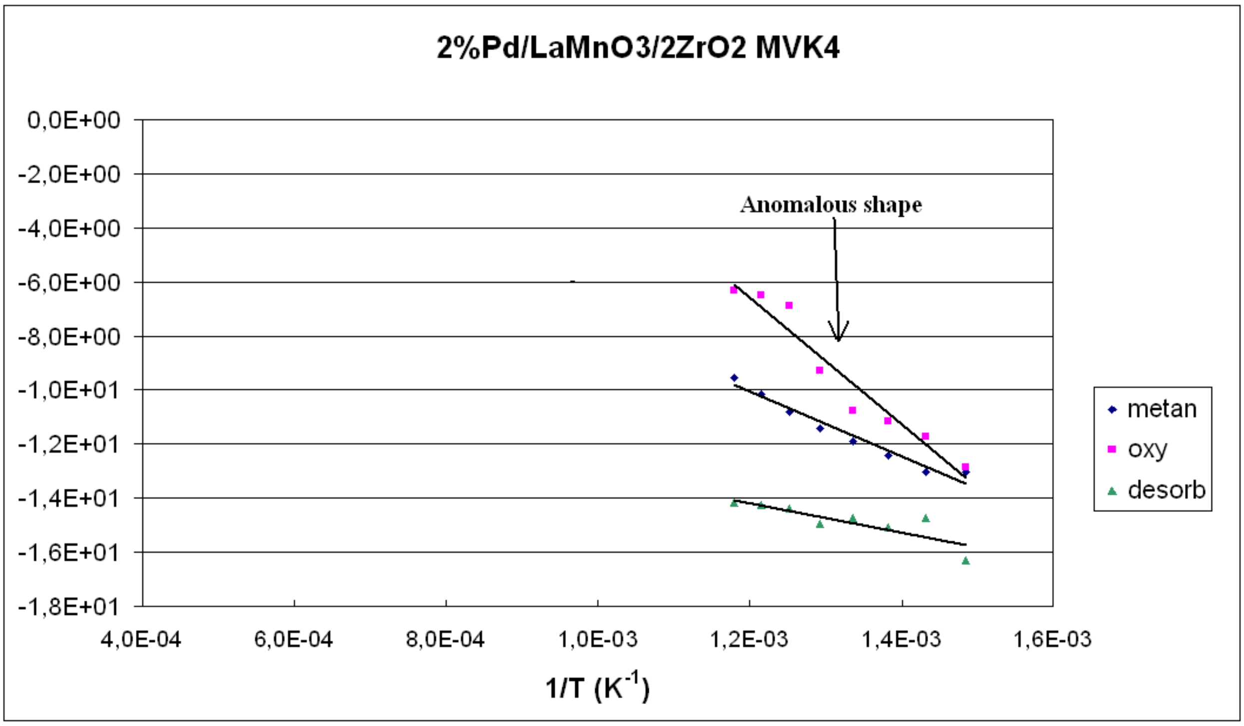

Figure 36 : Anomalous behaviour of oxygen reaction on 2% Pd/$LaMnO_3$/$2ZrO_2$

This effect doesn't occur in the Pd/$CeZrO_2$ catalyst because of the extremely efficient dispersion of Palladium inside the ceria zirconia matrix so that no phase transition happens to the active site.

Also the strange behavior of Pd/$LaMnO_3$/$2ZrO_2$ TPC during cooling can be explained using the uncommon property of Palladium.

As said before, because PdO formation is exothermic it is very probable that during TPC reported on Figure 34 heating at high temperature forces Palladium oxide dissociate into its components forming metallic Palladium; during cooling, Pd(0), which is less active than oxide, fails to burn completely methane until temperature decreases enough to permit PdO formation; after that, conversion picks up again.

After having considered all the issues cited above we concluded that the Mars Van Krevelen model n°2 was the best fitting model for CH4 combustion on $LaMnO_3/2ZrO_2$ while the most suited model for CH4 combustion on 2%Pd $LaMnO_3/2ZrO_2$ was Mars Van Krevelen model n°4.

MVK4 is the same model that gave very good result applied to methane combustion on 2% Pd $Ce_{0,33}Zr_{0,66}O_2$,probably because a large part of the reaction occurs on Pd active sites.

8.3.2 Undoped LaMnO3 /2ZrO2 plots

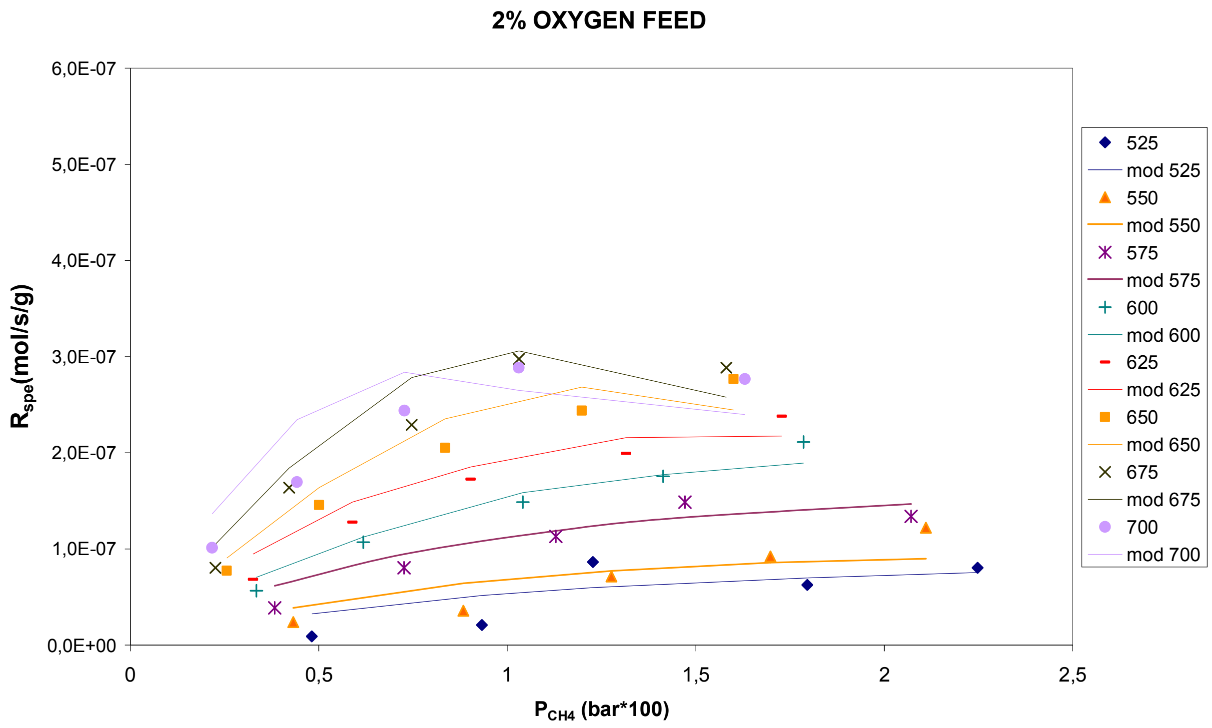

Figure 37: Reaction rate on $LaMnO_3/2ZrO_2$ vs inlet methane pressure at a fixed inlet oxygen molar fraction of 2%

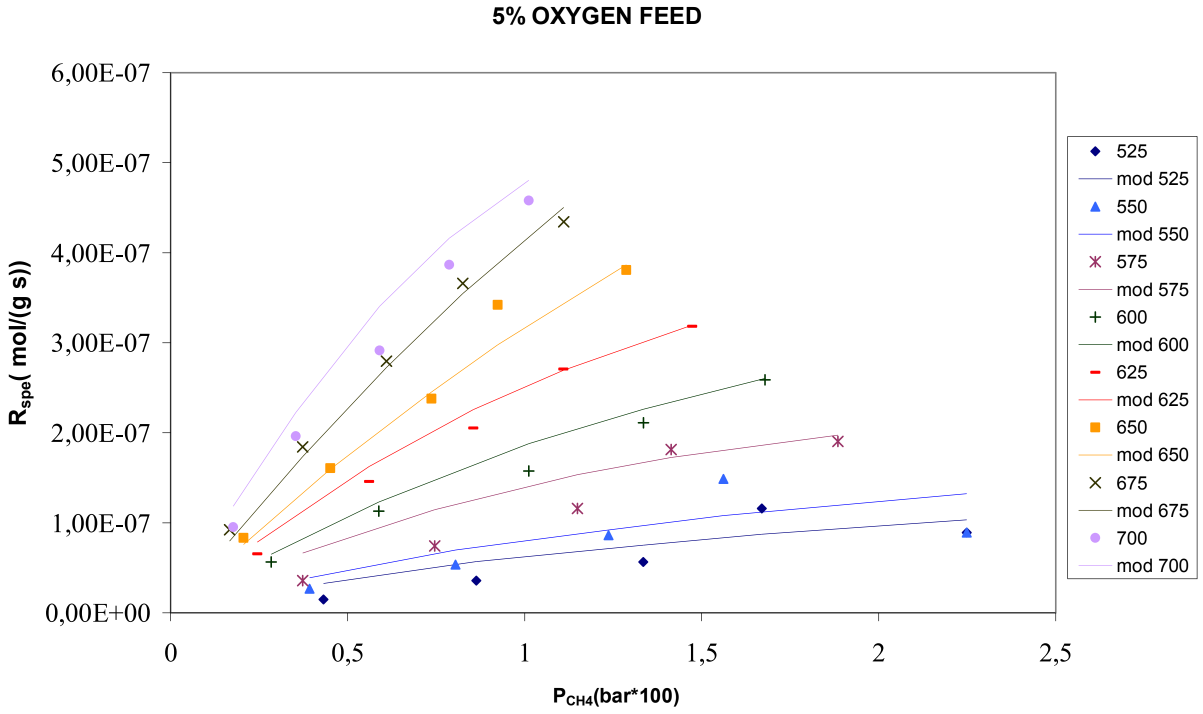

Figure 38: Reaction rate on $LaMnO_3/2ZrO_2$ vs inlet methane pressure at a fixed inlet oxygen molar fraction of 5%

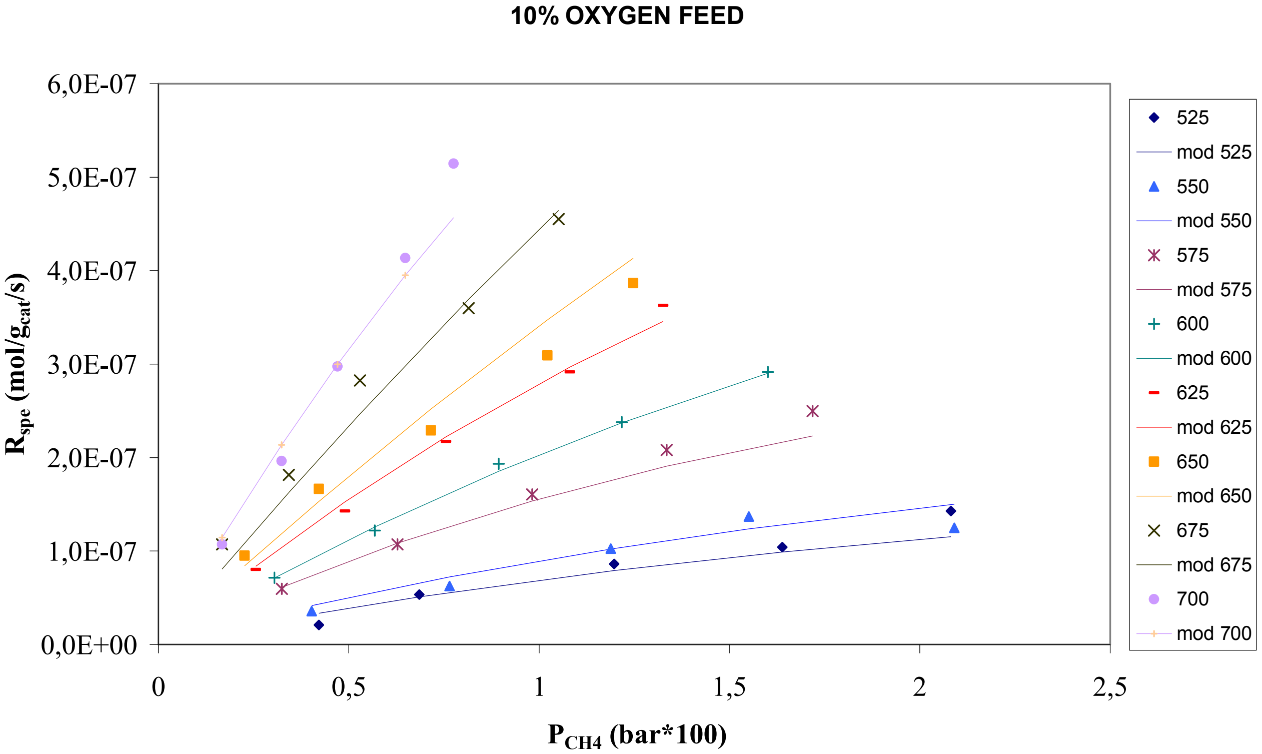

Figure 39: Reaction rate on $LaMnO_3/2ZrO_2$ vs inlet methane pressure at a fixed inlet oxygen molar fraction of 10%.

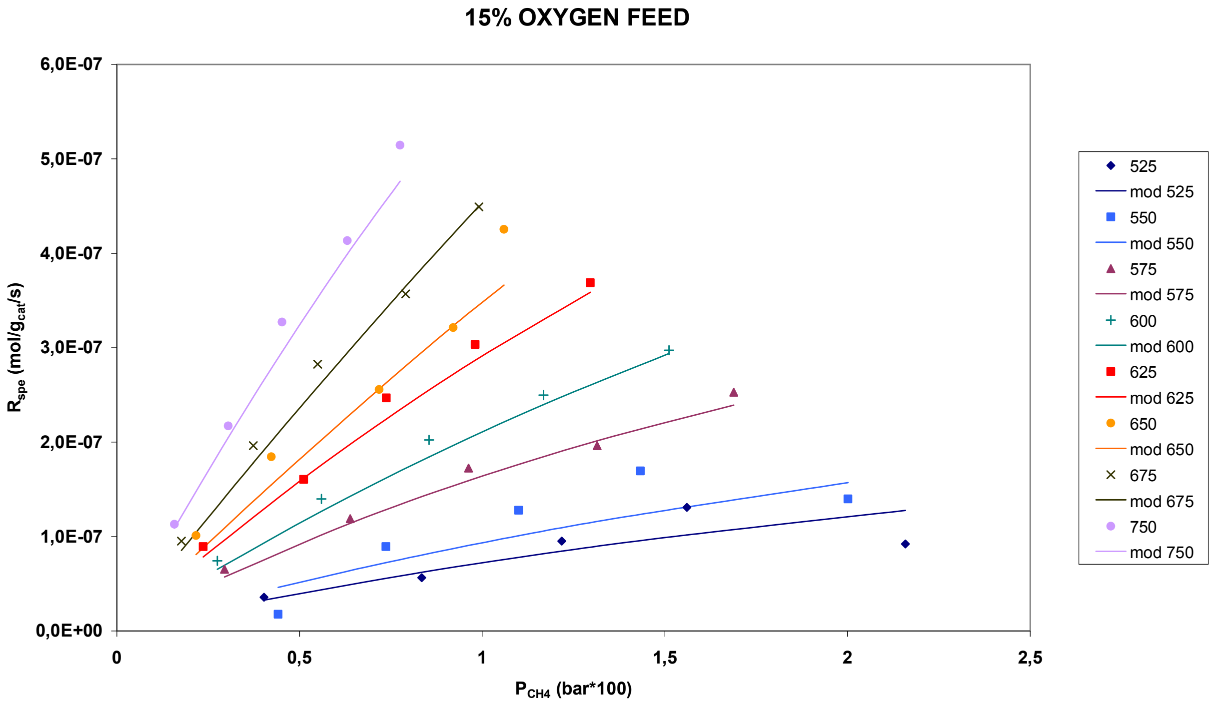

Figure 40: Reaction rate on $LaMnO_3/2ZrO_2$ vs inlet methane pressure at a fixed inlet oxygen molar fraction of 15%

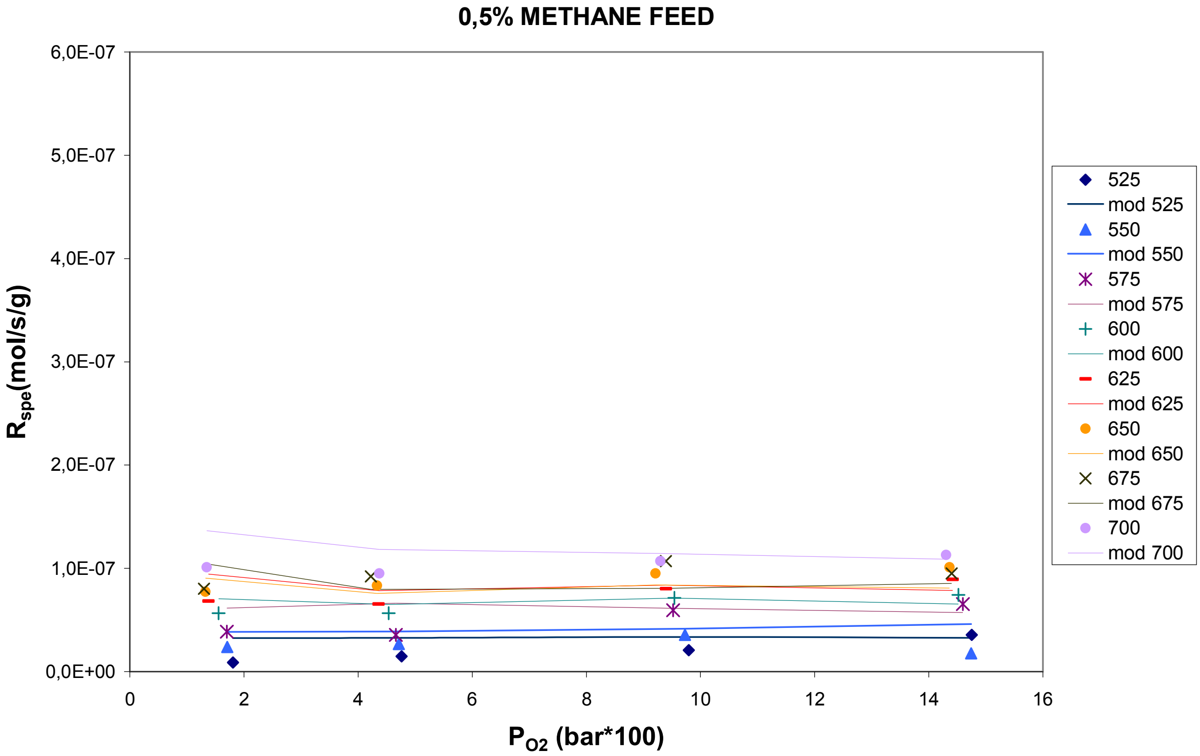

Figure 41: Reaction rate on $LaMnO_3/2ZrO_2$vs inlet oxygen pressure at a fixed inlet methane molar fraction of 0,5%

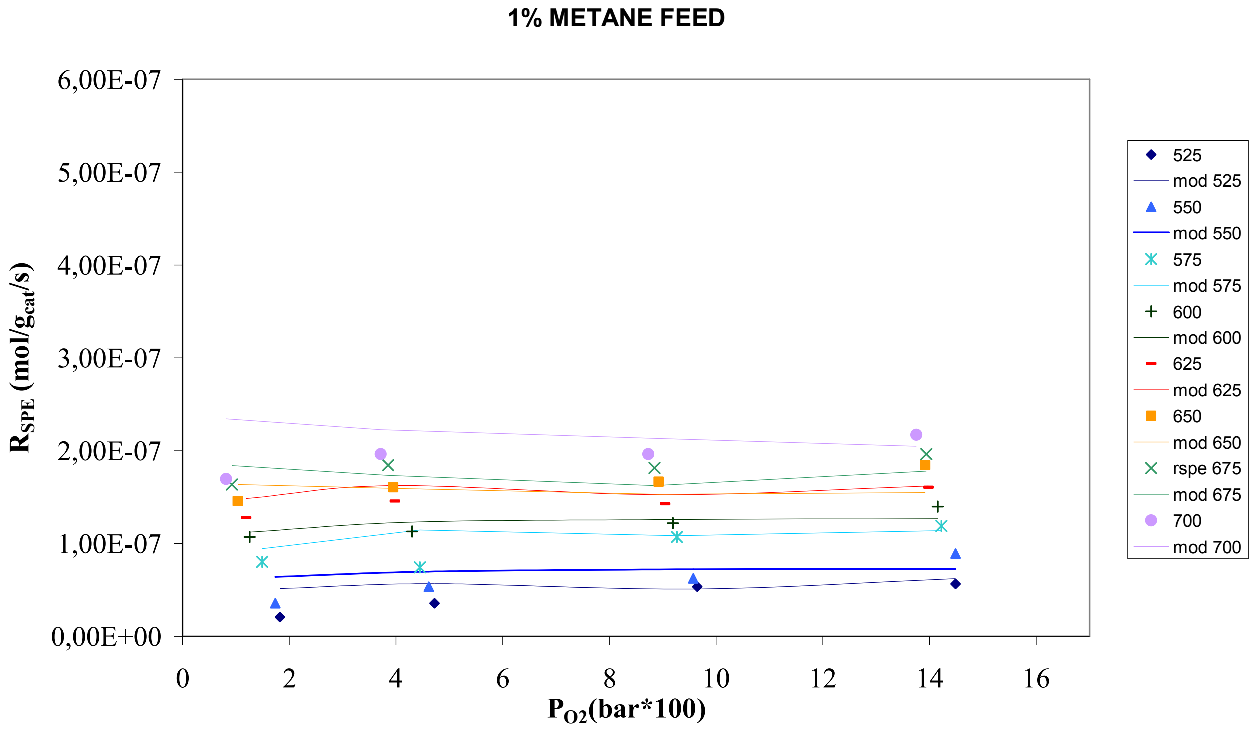

Figure 42: Reaction rate on $LaMnO_3/2ZrO_2$ vs inlet oxygen pressure at a fixed inlet methane molar fraction of 1%

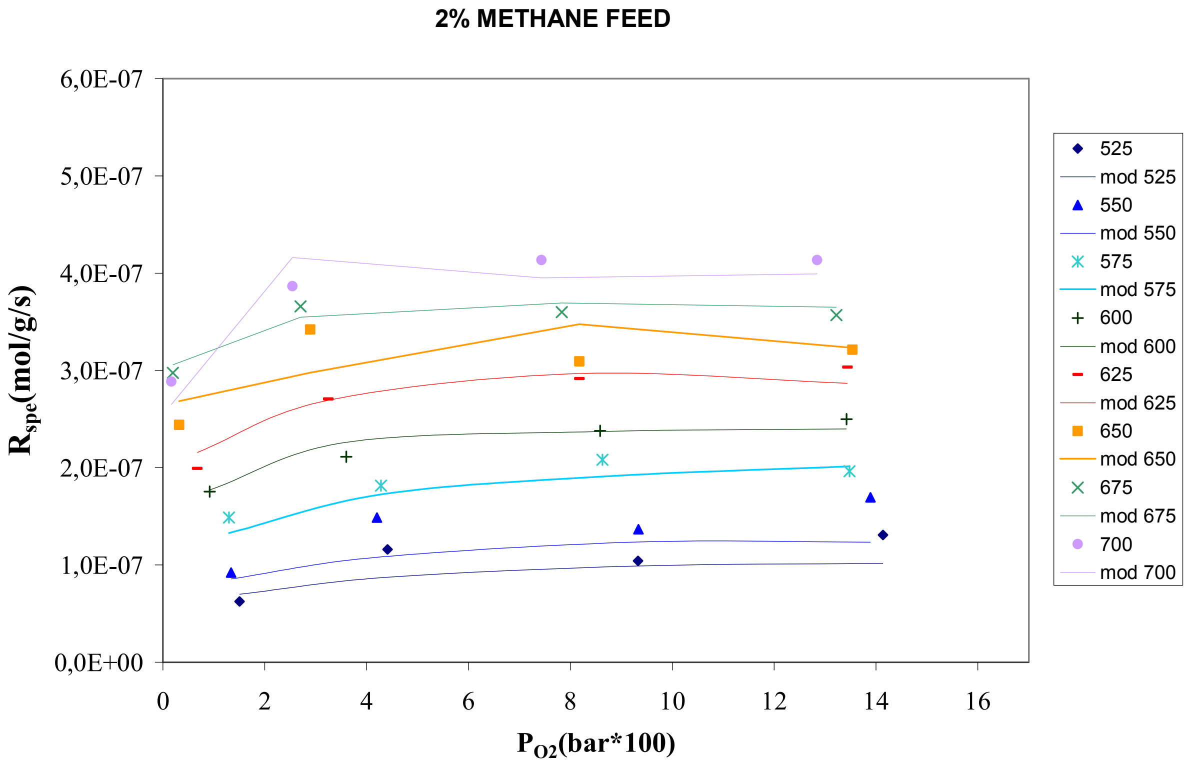

Figure 43: Reaction rate on $LaMnO_3/2ZrO_2$ vs inlet oxygen pressure at a fixed inlet methane molar fraction of 2%

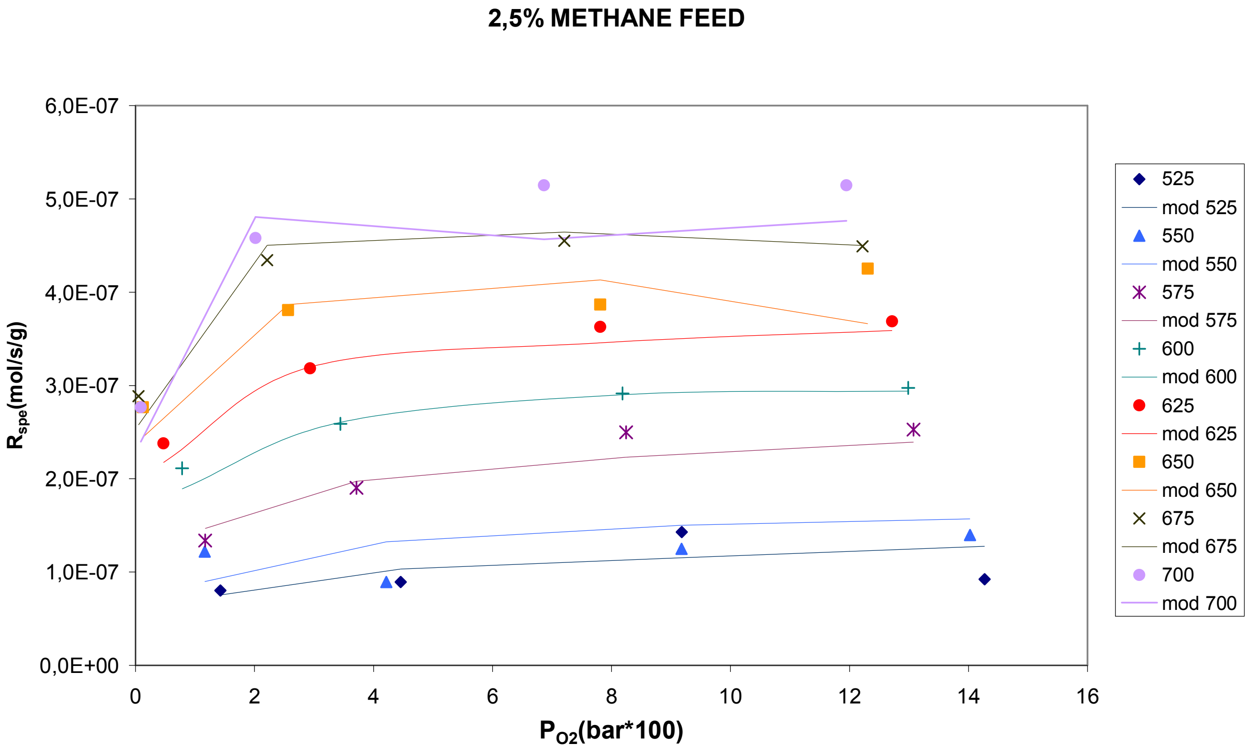

Figure 44: Reaction rate on $LaMnO_3/2ZrO_2$ vs inlet oxygen pressure at a fixed inlet methane molar fraction of 2,5%.

8.3.3 Palladium doped plots

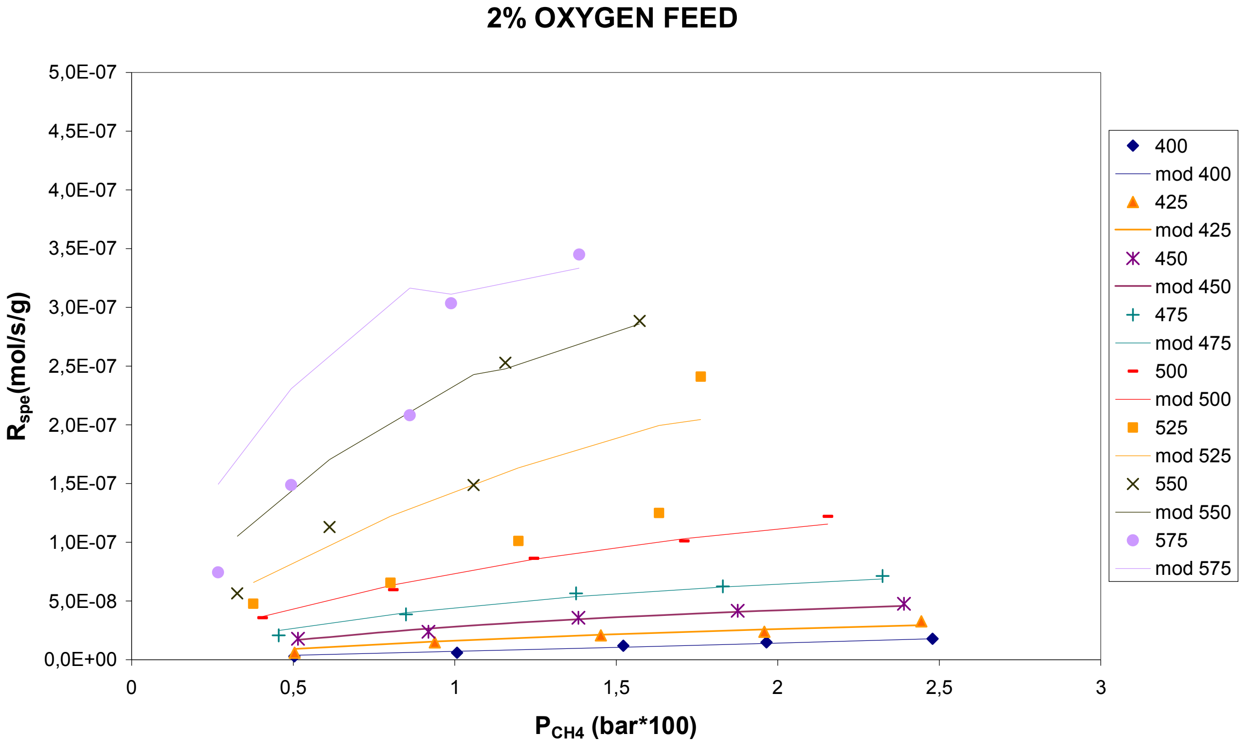

Figure 45: Reaction rate on $Pd/LaMnO_3/2ZrO_2$ vs inlet methane pressure at a fixed inlet oxygen molar fraction of 2%

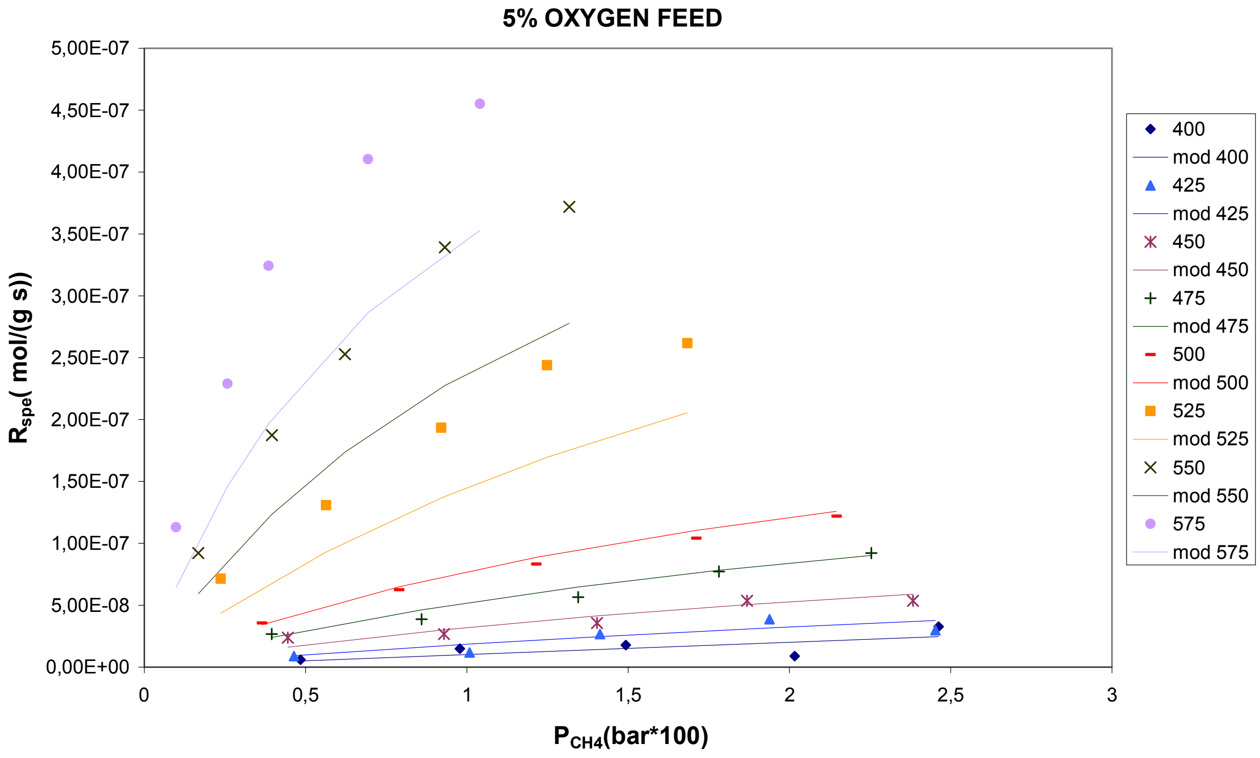

Figure 46: Reaction rate on Pd/LaMnO$_3$/2ZrO$_2$ vs inlet methane pressure at a fixed inlet oxygen molar fraction of 5%

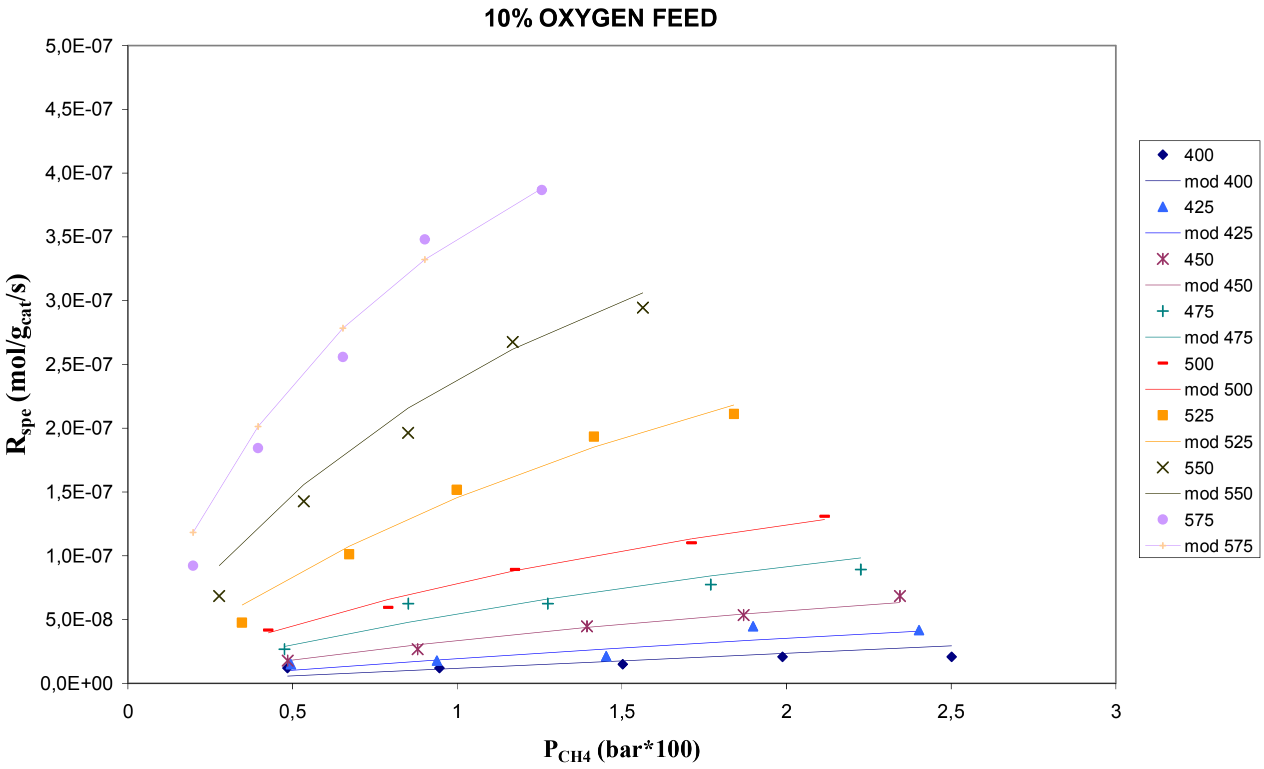

Figure 47: Reaction rate on Pd/LaMnO$_3$/2ZrO$_2$ vs inlet methane pressure at a fixed inlet oxygen molar fraction of 10%

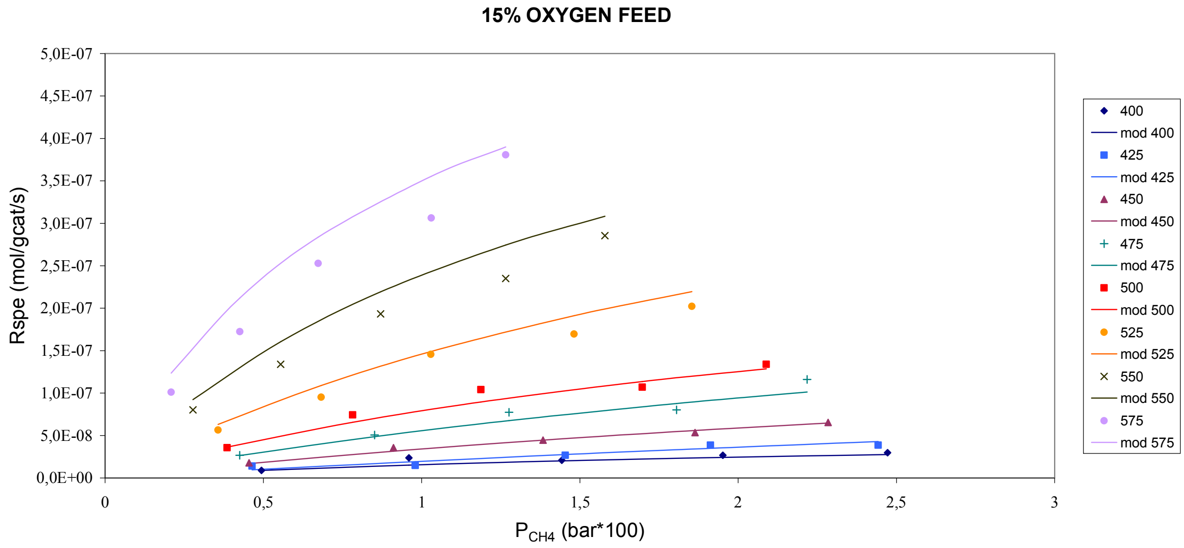

Figure 48: Reaction rate on $Pd/LaMnO_3/2ZrO_2$ vs inlet methane pressure at a fixed inlet oxygen molar fraction of 15%

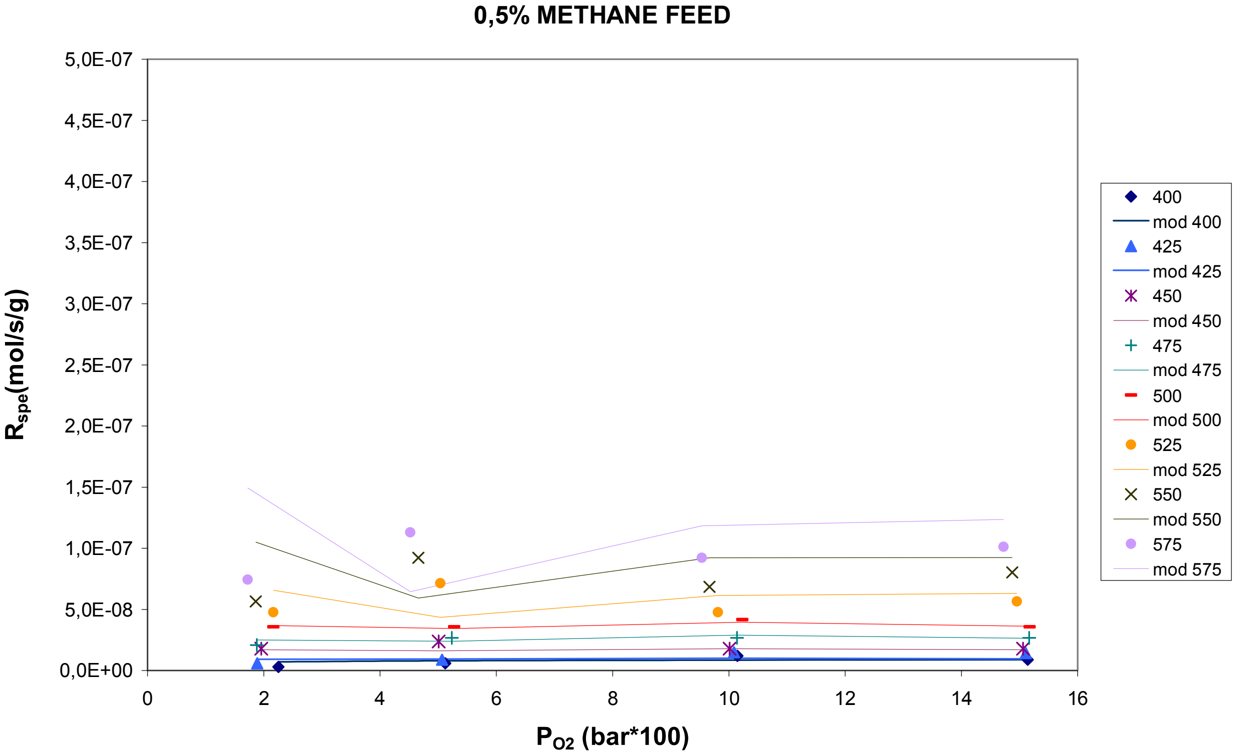

Figure 49: Reaction rate on $Pd/LaMnO_3/2ZrO_2$ vs inlet oxygen pressure at a fixed inlet methane molar fraction of 0,5%

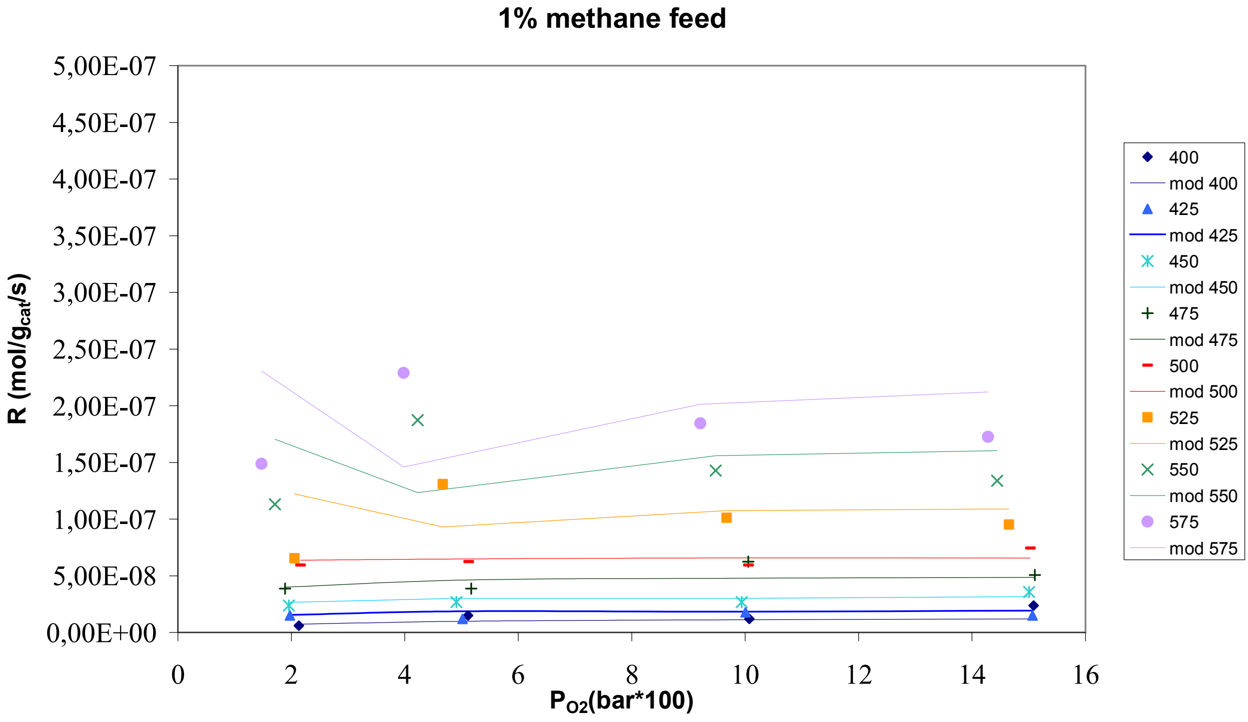

Figure 50: Reaction rate on Pd/LaMnO$_3$/2ZrO$_2$ vs inlet oxygen pressure at a fixed inlet methane molar fraction of 1%

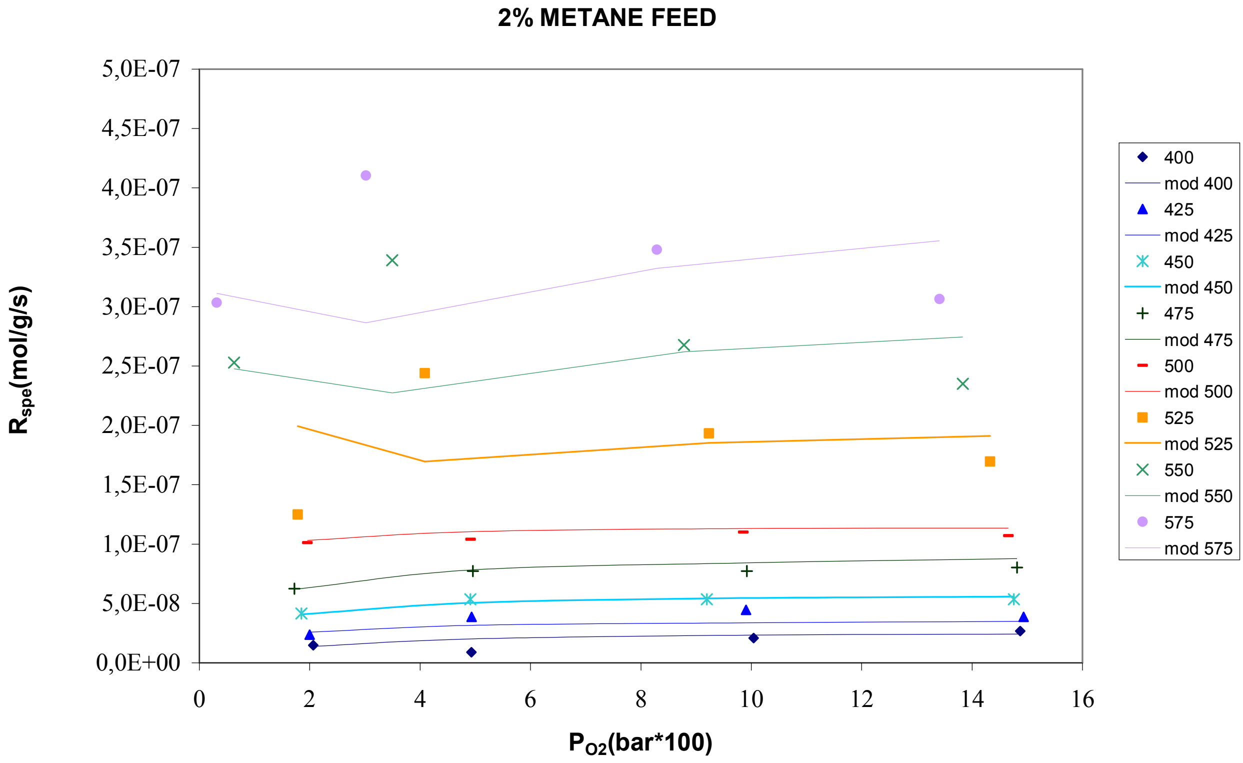

Figure 51: Reaction rate on Pd/LaMnO$_3$/2ZrO$_2$ vs inlet oxygen pressure at a fixed inlet methane molar fraction of 2%

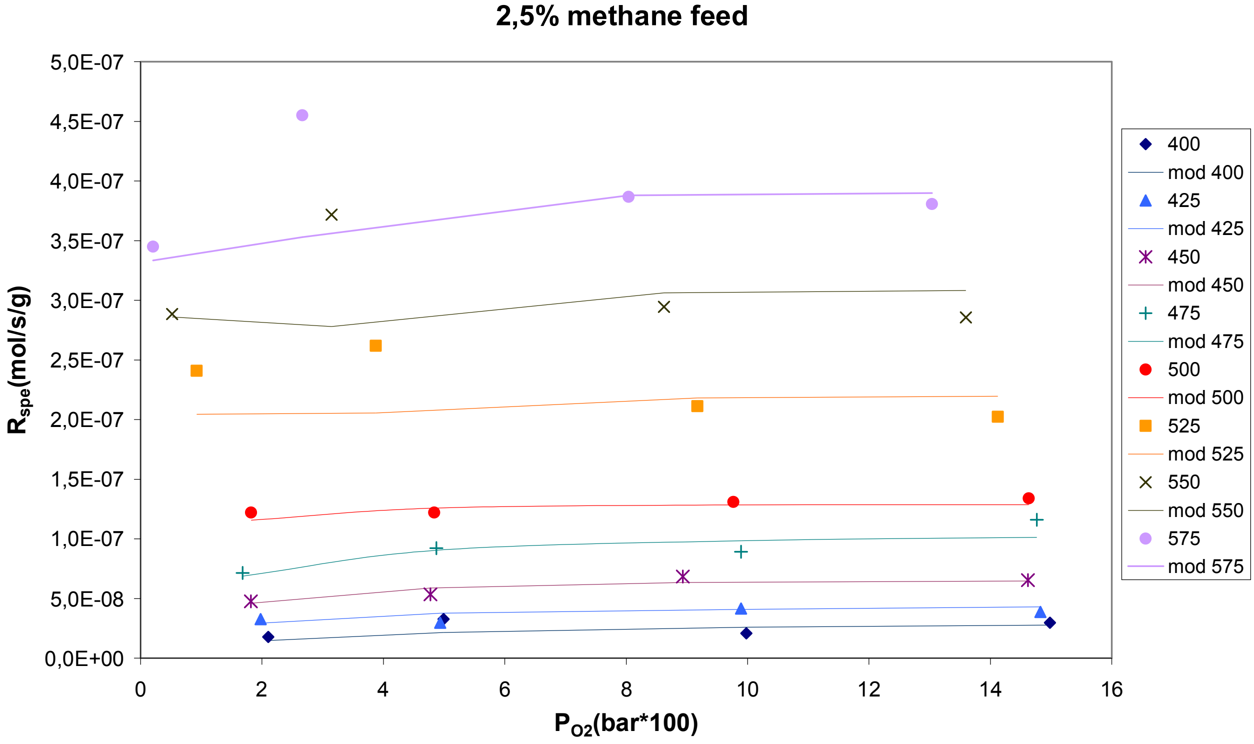

Figure 52: Reaction rate on Pd/$LaMnO_3$/$2ZrO_2$ vs inlet oxygen pressure at a fixed inlet methane molar fraction of 2,5%

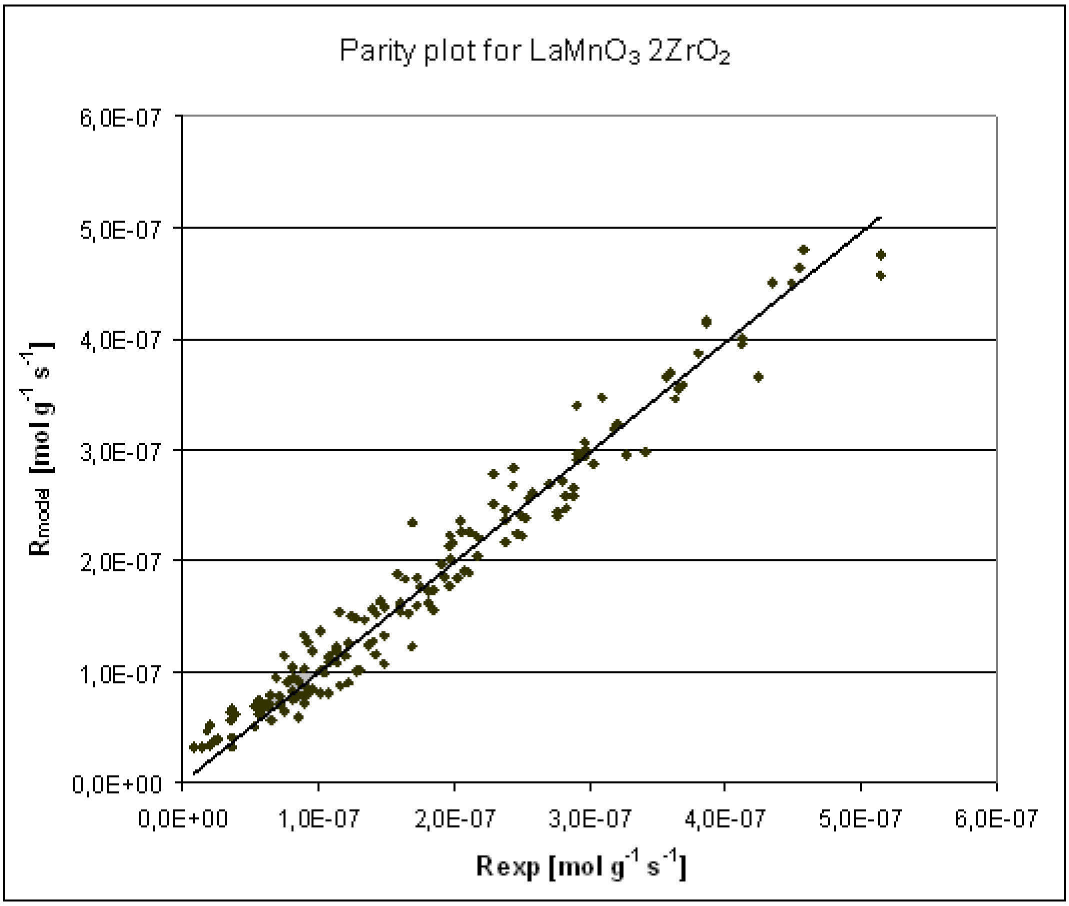

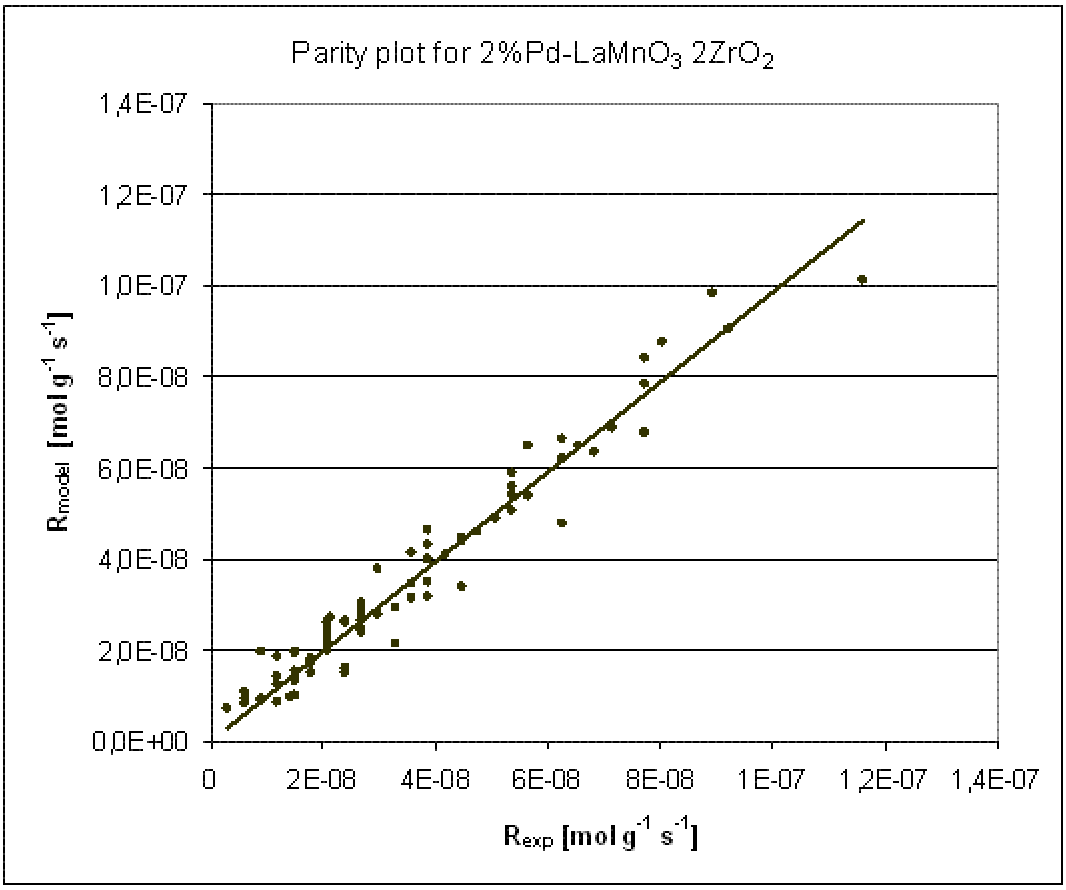

Figure 53: Parity plot used as a final check for the quality of the fitting

References for chapter 8

1. Magdalena Bosomoiu , Grigore Bozga , Daniela Berger , Cristian Matei: "*Studies on combustion catalytic activity of some pure and doped lanthanum cobaltites*" Applied Catalysis B: Environmental 84 (2008) 758–765

2. E. Campagnoli, A. Tavaresb, L. Fabbrinia, I. Rossettia,Yu.A. Dubitskyb, A. Zaopob, L. Fornia: "*Effect of preparation method on activity and stability of* $LaMnO_3$ *and* $LaCoO_3$ *catalysts for the flameless combustion of methane*" Applied Catalysis B: Environmental 55 (2005) 133–139

3. R.A.M. Giacomuzzi,M. Portinari, I. Rossetti, L. Forni, *"A new method for preparing nanometer-size perovskitic catalysts for* CH_4 *flameless combustion"* Stud. Surf. Sci. Catal. 130A (2000) 197

4. Rossetti, L. Forni, Appl. Catal. B: Environ. *"Catalytic flameless combustion of methane over perovskites prepared by flame–hydrolysis"* 33 (2001) 345.

5. J. Liu, Z.-Y. Wen, Z. Gu, M.W.Z. Lin, J. Electr. Soc. "*synthesis by anEDTA based soft chemistry route and charachterization of nanosized* $LiCoO_2$ cathode matherials"149 (11) (2002) A1405–A1408.

6. Simon Ifrah, Akim Kaddouri, Patrick Gelin, Didier Leonard: "*Conventional hydrothermal process versus microwave-assisted hydrothermal synthesis of* $La_{1-x}Ag_xMnO_{3\pm\delta}$ *(x = 0, 0.2) perovskites used in methane combustion*" C. R. Chimie 10 (2007) 1216-1226

7. Kaddouri, S. Ifrah : *“Microwave-assisted synthesis of $La_{1-x}B_xMnO_{3.15}$ (B= Sr, Ag; x = 0 or 0.2) via manganese oxides susceptors and their activity in methane combustion”* Catalysis Communications 7 (2006) 109–113

8. N. Gunasekaran S. Rajadurai, J.J. Carberry , N. Bakshi , C.B. Alcock : “*Surface characterization and catalytic properties of $La_{1-x}A_x$ MO, perovskite oxides.Part II. Studies on $La_{1-x}Ba_x MnO_3$ ($0 < x < 0.2$) oxides”* Solid State Ionics 81 (1995) 243-249

9. G. Ch. Kostogloudis, N. Vasilakos & Ch. Ftikos: “*Preparation and Characterization of $Pr_{1-x} Sr_x MnO_{3\pm\delta}$ (x = 0, O-15, O-3, 0.4, 0.5) as a potential SOFC Cathode Material Operating at Intermediate Temperatures (500-700)”* Journal of the European Ceramic Society 17 (1997) 1513-1521

10. Luca Marchetti, Lucia Forni: *“Catalytic combustion of methane over perovskites”* Applied Catalysis B: Environmental 15 (1998) 179-187

11. Guido Saracco, Francesco Geobaldo, Giancarlo Baldi *“Methane combustion on Mg-doped LaMnO3 perovskite catalysts”* Applied Catalysis B: Environmental 20 (1999) 277±288

12. Marco Daturi, Guido Busca , Gianpiero Groppi, Pio Forzatti: *"Preparation and characterisation of $SrTi_{1-x-y} Zr_xMn_yO_3$ solid solution powders in relation to their use in combustion catalysis”* Applied Catalysis B: Environmental 12 (1997) 325-337

13. Civera, G. Negro, S. Specchia, G. Saracco, V. Specchia: “*Optimal compositional and structural design of a LaMnO3/2ZrO2/Pd-based catalyst for methane combustion”* Catalysis Today 100 (2005) 275–281

14. Beguin, B.; Garbowski, E.; Primet, M. *“Stabilization of alumina by addition of lanthanum.”* Appl. Catal. 1991, 75, 119.

15. McCarty, J. G. *“Kinetics of PdO combustion catalysis”.* Catal. Today 1995, 26, 283.

16. Kleykamp, K. *“Freie Bildungsenthalpie von Palladiumoxid”.* Z. Phys. Chem. N.F. 1970, 71, 142.

9 CFD modelling of catalytic micro-combustors

9.1 Literature about catalytic combustion devices

The use of powdered catalysts is little applied aside from academic use because powders tend to pack into dense structures with a quite high pressure drop; on the other hand, pelletized catalyst has lower gas-diffusion performances if used inside very small scale reactors so the need for large scale items of an engineered support becomes evident.

Recent literature [1,2] has presented the benefits of fluid dynamics calculation in the field combustion technology to understand and reduce both NO_X and soot formation issues in the studied combustors.

In particular, once the model is set up and well working, it is very simple to launch many runs trying in silico many geometry variants that would be difficult and expensive to try in reality.

Another important feature is that virtually any important parameter of the analyzed system can be evaluated without perturbing the studied device (a very important feature when modelling a micro-device).

Literature so far proposed mainly two kinds of innovative homogeneous burners: the fibrous catalytic burners [3,4] and the catalyzed monolith

The catalyzed monolith is a technology derived from automotive industry that allows chemical reactions to be operated with minimum pressure drop: in this case the fluid dynamics plays a major role because the catalytic material is only on monolith's walls and reagents have to diffuse until they reach them before reacting: more over [5] have established that the heat developed by the catalytic combustion may be enough to sustain homogeneous combustion whose kinetics is altered by the presence of the walls [6].

Di Benedetto [7] wrote that with some combinations of external insulation, gas velocities, monolith's wall thickness and thermal conductivity of the solid phase the heat generated by a started combustion can reheat the inlet gases up to sustain a stable reaction.

The typical dimensions of channels featuring good heat recirculation is 1-2 mm: one of this devices was tested in [8] with a monolith of silicon carbide which, without any catalysts, was able to burn methane at an inlet temperature of about 450°C.

Di Benedetto and Di Sarli published some interesting papers in which they used CFD to understand wall and bulk phenomena occurring inside a catalyzed monolith with the appropriate simplifications modelling both 2D and 3D domains [5,7,9]; however they neglected phenomena occurring at the inlet and at the outlet of the channel.

Also [10] and published recently study on the topic: they focused on hetero-homogeneous mechanism using CHEMKIN® solver for chemical species while the fluid dynamic was treated by a 2D code developed by researchers which included irradiative heat transfer in their model..

They further focused on the sensitivity of their model at varying geometrical parameters, inlet velocity, pressure and solid thermal conductibility .

The model treated in this article, instead, took into account the flow distortion caused by the geometry of the real micro combustor described in [8].

9.2 Modelling of a micro-combustor using a preliminary bi-dimensional model

At first, because just a preliminary model was developed, the combustor was modelled as a simple axisymmetric 2D geometry that features a single circular channel restriction whose diameter was selected be cause of a compromise between the need of simplicity (at that time only a dated desktop was available for simulations) and the need of still capturing flow accelerations and distortions occurring at the inlet and the vortex placed beside the outlet of the micro combustor (in the end this compromise was chosen arbitrarily).

As seen in Figures 54-55 the reactor channel had 5 mm radius, the SiC wall is 0,25 mm thick while the inner channel representing the SiC monolith had 2 mm radius: this meant that the monolith was treated as a single circular shape.

The vermiculite insulation was considered as a perfectly which was treated as a perfectly adiabatic zone and therefore it wasn't drawn in the mesh used for C.F.D.

Geometry creation and meshing was performed with Gambit® while the fluid dynamics solution was obtained with Fluent 6.3.22®

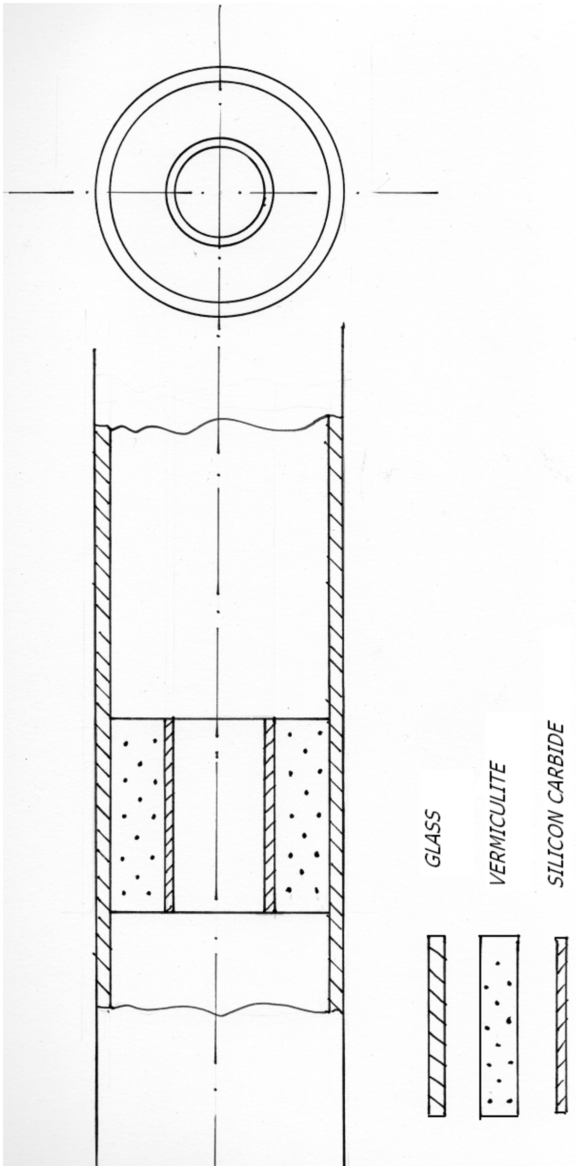

Figure 54: Scheme used for axialsimmetric modelling (marking differently vermiculite, silica glass, and silicon carbide)

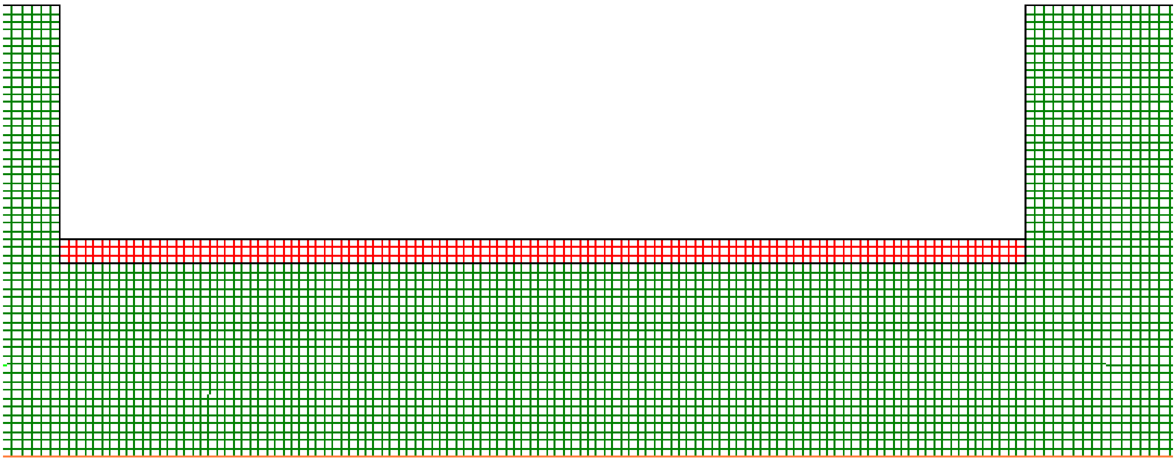

Figure 55: Detail of the channel zone as Fluent models it:red color highlights the silicon carbide layer inside the modelled domain

The reaction implemented to simulate catalytic methane combustion was taken from [11,12] which describes a Pd/$Ce_{0,33}Zr_{0,66}O_2$ catalyst with a theoretical loading of 5% on weight basis; the formula of the Mars-van Krevelen mechanism applied is:

$$R = \frac{k_1 p_{CH4} k_2 p_{CH4}}{2k_1 p_{CH4} + k_2 p_{CH4}} * \left(1 - \frac{k_1 p_{O2}}{k_3}\right) \qquad (10)$$

Fitted with these parameters

E_1	31.9 kJ mol^{-1}	k^{∞}_1	2.95 mol g^{-1} s^{-1} bar^{-1}
E_2	23.77 kJ mol^{-1}	k^{∞}_2	0.726 mol g^{-1} s^{-1} bar^{-1}
E_3	5.4 kJ mol^{-1}	k^{∞}_3	$2.66*10^{-3}$ mol g^{-1} s^{-1}

Table 10: Kinetic parameters for Mars van Krevelen model 3

During computer simulation it became clear that this kind of Mars van Krevelen model had some problem predicting the catalytic reaction rate when challenged with gas concentrations different from the ones used during kinetics assessment tests.

This was caused by the fact that the equation featured a subtraction that could led to negative reaction rates; to overcome this obstacle another kinetic equation was implemented

$$R = \frac{k_1 p_{CH4} k_2 p_{CH4}}{2k_1 p_{CH4} + k_2 p_{CH4} + k_1 p_{CH4} k_2 p_{CH4} / k_3} \qquad (11)$$

Fitted with these parameters

E_1	24.4 kJ mol^{-1}	K^{∞}_1	0.375 mol g^{-1} s^{-1} bar^{-1}
E_2	33.8 kJ mol^{-1}	K^{∞}_2	23.1 mol g^{-1} s^{-1} bar^{-1}
E_3	8.89 kJ mol^{-1}	K^{∞}_3	$2.21*10^{-4}$ mol g^{-1} s^{-1}

Table 11: Kinetic parameters for Mars van Krevelen model 4

This equation was chosen because it was the second best fitting one and was reliable beyond experimentation field as well.

Given the high temperature reached by the gas near walls it was very likely that also homogeneous oxidation happened and for this reason the homogeneous mechanism taken from [6] was implemented inside the model

$$R = k \cdot c_{CH_4}^{\ 0.96} \qquad (12)$$

The parameters of this model are a pre exponential constant of 4.532.300 kmol/s and an activation energy of 130.66 kJ/mol.

The inlet composition has been fixed as very lean 1,7% weight basis of methane in air and mass flux was set at $1*10^{-3}$ g/sec that ensured a peak velocity of about 0,4 m/s at 900K

Simulations were performed at various inlet temperatures ranging from 700K to 900K oven temperatures, used for the evaluation of the heat transfer between gas and the silica tube, were modified accordingly ; pressure was set to 1 bar; in order to initialize the calculation both a cold flow and a high temperature pre-calculated solutions; reactions were disabled while computing this initialization points.

9.2.1 Numerical considerations

When the CFD code has to be run the user must consider and solve supplementary issues arising from the additional parameters the program needs to converge.

Fluid dynamic model was chosen laminar because the small Reynolds number (about 65) inhibits turbulence, the gradient calculation was set to node based because of its higher accuracy while the pressure term was kept as standard default owing the low pressure gradients.

For what concerns the interactions between pressure and velocity the coupled pressure based solver was chosen because of the speed up given to the solution of the rear side laminar vortex and because the bi-dimensional simulation was still enough light to be run.

In order to capture the right species concentration field, the gas was modelled as a true multi-component stream and the ideal gas method was chosen for density calculation to take into account the thermal expansion that accelerates the burning gas flow.

Surface chemistry was modelled employing a user defined function (UDF) because the default reaction model used by Fluent accepted only power law kinetics.

The most important parameter influencing convergence speed was the energy equation's under-relaxation factor: when the default energy equation's under-relaxation factor was used this led to an unstable scheme caused by Fluent overestimating methane combustion rate.

This inaccuracy was so high that in the following step a negative methane concentration was computed and, although the solver clipped methane concentration back to zero, the wrong reaction rate was still applied inside the heat equation and in some cells temperature overshot up to 5000 K (even more than adiabatic combustion temperature!) .

Challenged with sudden shock waves of pressure and heat, both coupled, uncoupled and also density based fluid motion solvers crashed after some tenths of iterations.

After many attempts of tuning the pressure velocity coupling solver it was realized that, despite crashes happened in that section of the code, the source of instability lied elsewhere.

Quickly it was found that changing the energy equation's under-relaxation factor from the default value of 1.0 to 0.9997 led to a strong solver stability but further lower values slowed convergence time significantly by "freezing" the temperature profile.

From run analysis (Figure 56) it can be hypothesized that when a under relaxation factor less than 1 was given Fluent switched to completely different heat and chemical kinetics routines which proved to be very robust.

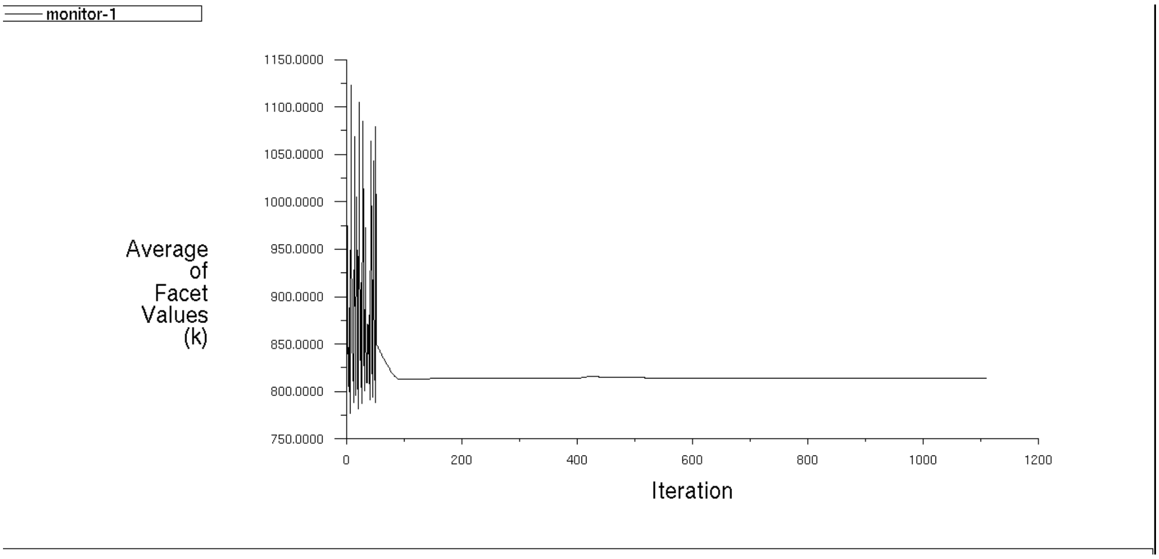

Figure 56: Sudden solution stability transition occurs when energy under-relaxation factor is modified from 1 to 0,9997

9.2.2 Results and discussion

Modelling results showed that the simulated flow speeds reached grid independence at about 30,000 square cells: starting from this point, the catalytic combustion kinetic and the homogeneous one were included in the model, first separately, then altogether.

When just the catalytic reaction model is activated as shown in figure 57 there's a temperature increase on reactive wall because of catalytic combustion but it is strongly limited by the diffusion of methane and so it's overall conversion is small.

Figure 60 shows that, when inlet temperature is 900 K and the homogeneous model is activated alone, the system shows two possible steady states.

In facts if initialized to inlet temperature the simulation gives 910 K of peak temperature, if gas temperature was patched to 1150 K the peak temperature decreased again but if gas temperature was initialized to 1300 K then the micro-combustor lighted on and peak temperature reached 1425 K; in this case almost all methane was burnt because CH_4 mass transfer was not the limiting factor (figure 58).

What appeared to stabilize this lean combustion was the heat recirculation from the burning zone to the first part of the micro-combustor which acted as an heat exchanger preheating the inlet mixture up to ignition temperature: it is very significant that a so lean stable combustion is unobtainable with just a free flame.

Figure 59 finally shows a complete model in which both mechanisms were activated: when simulation was started from 890 and 900 K the surface reaction was able to heat the mixture enough to make the homogeneous reaction start; after that the main oxidation mechanism becomes the combustion in the bulk of the gas.

Despite a forced high temperature of initialization, if gas inlet and tube walls are set to 700 K the simulation converges to an off steady state solution and shows only a modest surface reaction as main oxidation mechanism.

Finally in Figure 61 that shows velocity vectors is clear that the outer vortex plays a little role in defining what happens inside the channel: so it makes sense to disregard the outlet zone when approaching the 3D model.

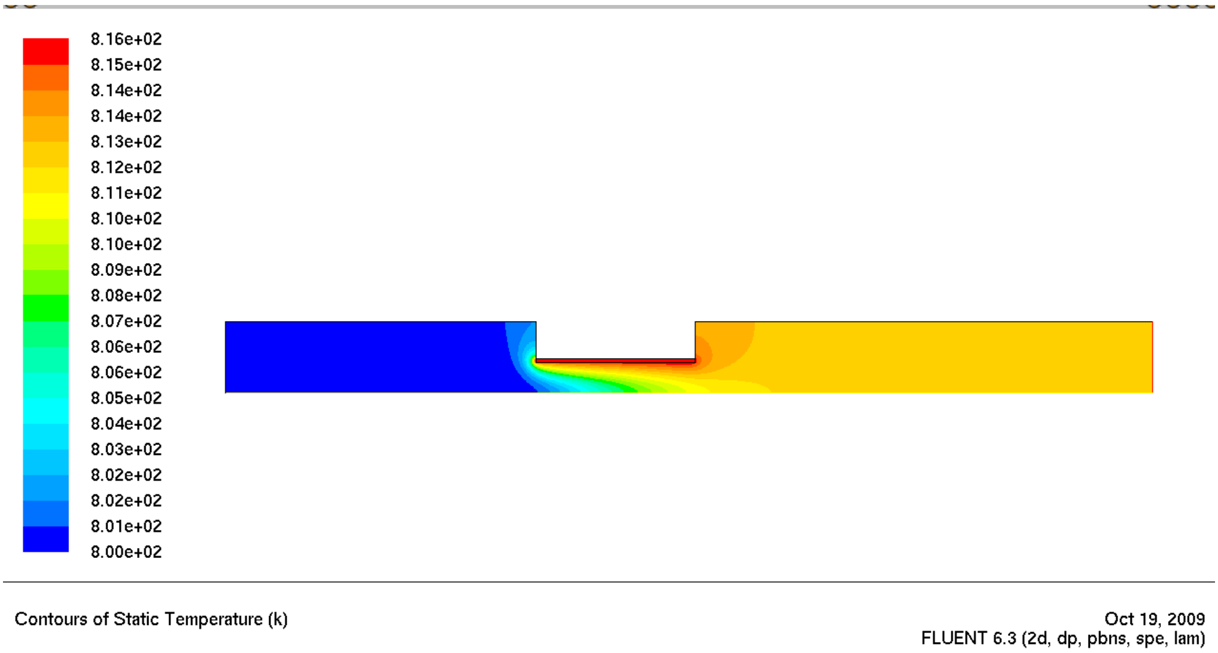

Figure 57: Contours of temperature during catalytic combustion

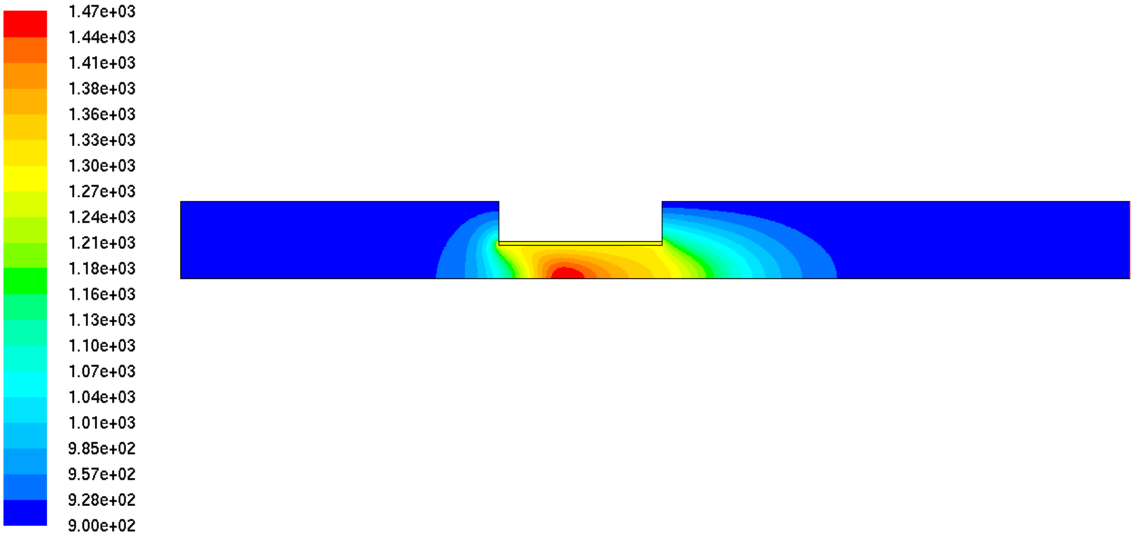

Figure 58: Contours of temperature during homogeneous combustion

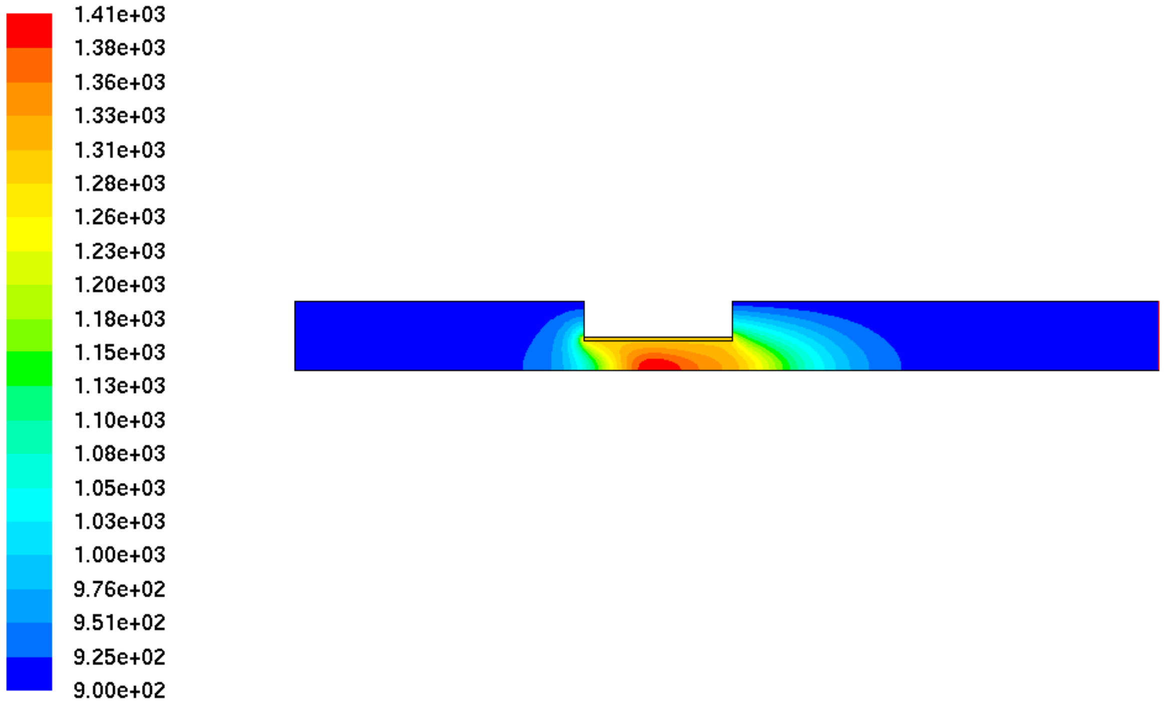

Figure 59: Contours of temperature with both homogeneous and catalytic combustion kinetics activated

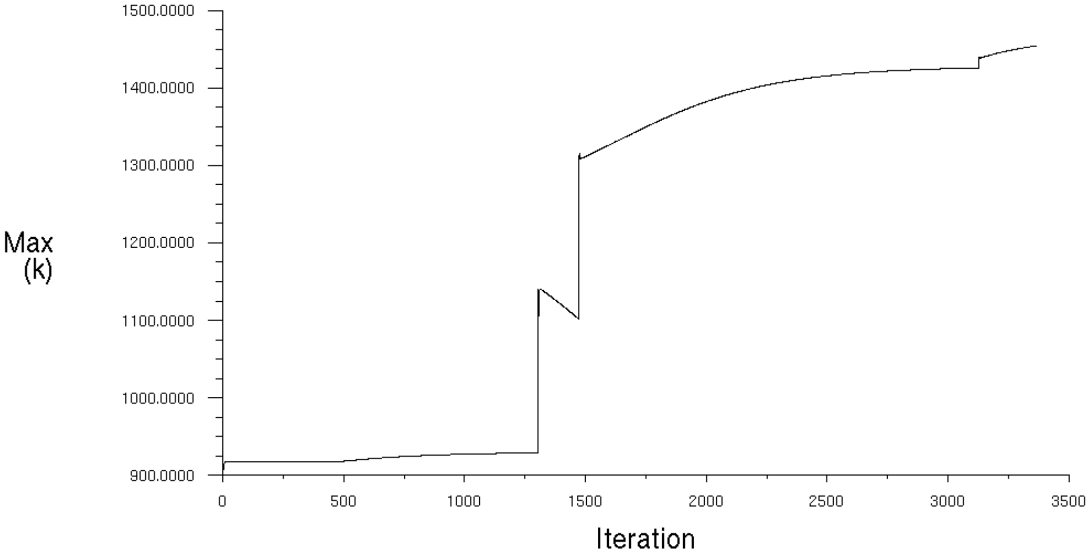

Figure 60: Convergence history of peak temperature for various initialization temperatures

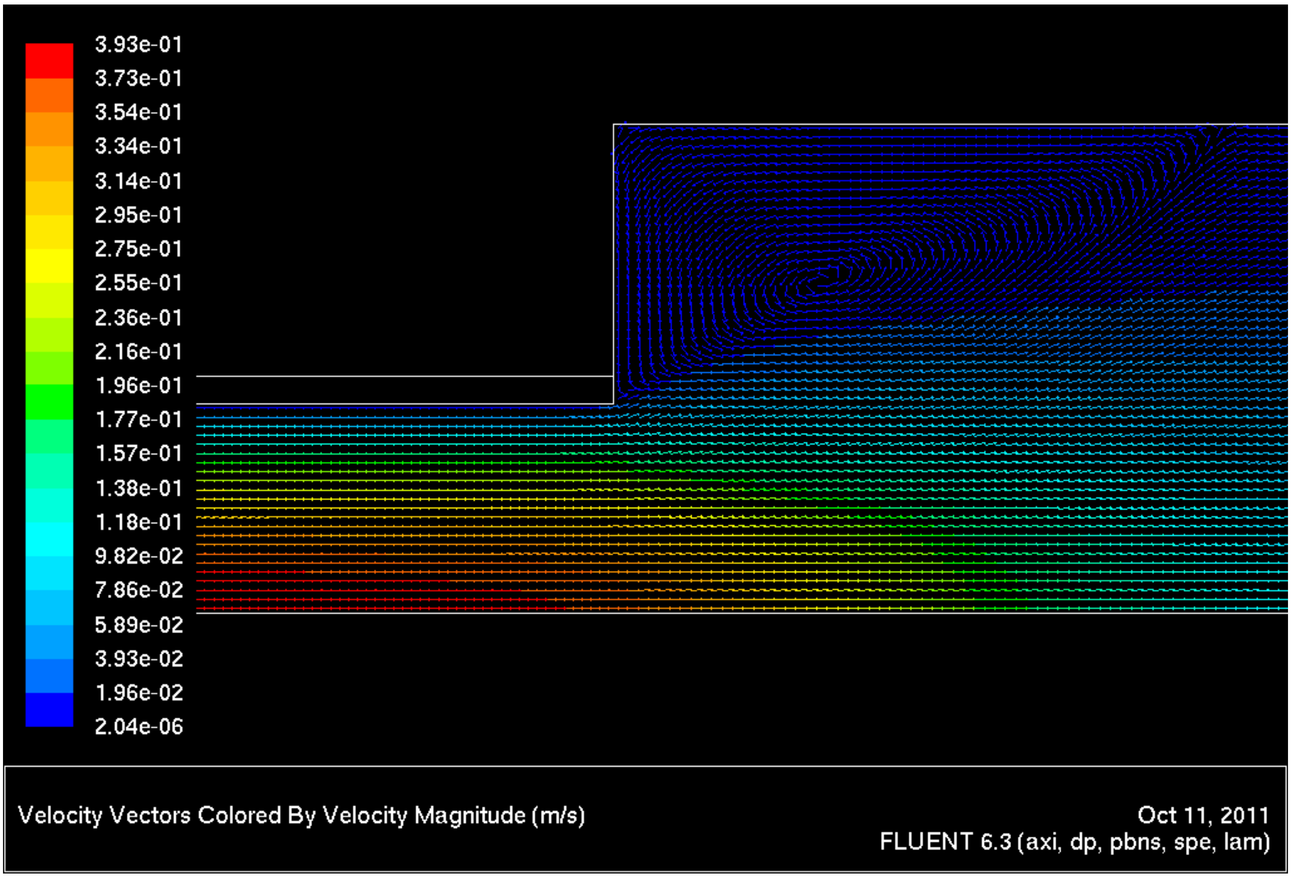

Figure 61: Backflow vortex has no influence on what happens inside the reactors channel

9.3 Modelling of the micro-combustor using a more complete 3D model

Finally the last goal of this thesis can be chased: to create a 3D CFD model in order to evaluate the thermal and fluid dynamics occurring in an experimental real reactor.

The CFD model is based on the fluid dynamics of the device reported in Figure 62

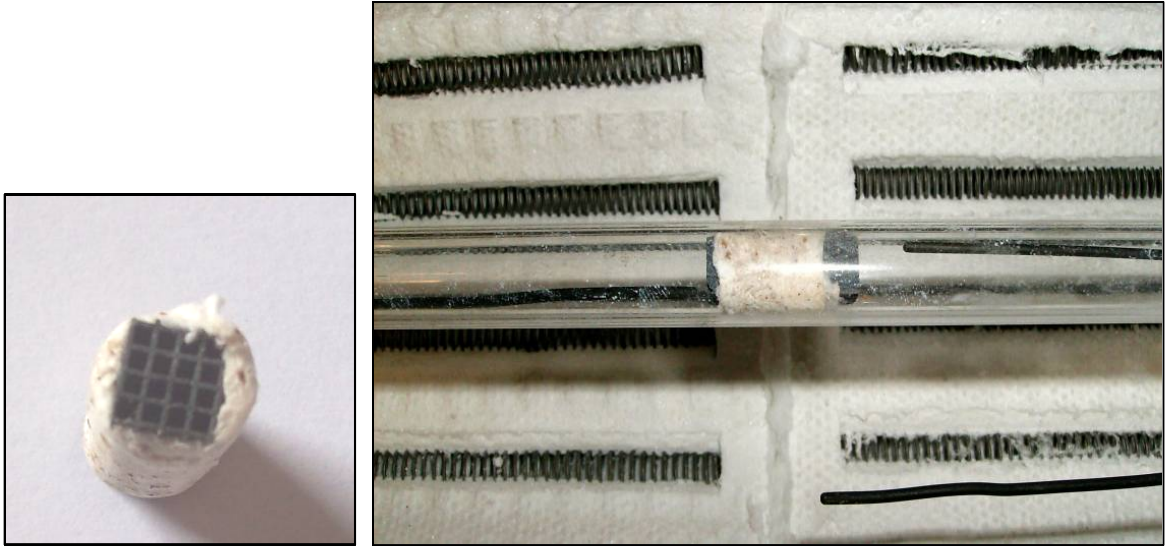

Figure 62: SiC monolith enveloped in vermiculite (left) and inside the furnace (right)

The combustion system is fed with two mass flows sending air and methane: gas flows are 191,6 Nml/min and 10 Nml/min respectively.

The geometry of the micro-combustor consists in a square Silicon Carbide monolith 5,5 mm wide and 25 mm long; 16 square channels arranged in a 4X4 square grid, each channel is 1,25 mm wide and each SiC wall is 0,1 mm thick.

The reactor assembly is completed by a vermiculite layer which keeps the monolith heat inside and prevents the combustible mixture to bypass externally the microreactor.

The vermiculite layer has a variable thickness to fill and seal the space between the square monolith and the fused silica tube whose inner diameter is 1 cm: when vermiculite is heated its dramatic expansion improves sealing.

After having solved the conceptual problems that lied behind the fluid dynamical modelling of a simple combustor, moving this expertise to a more realistic 3D geometry was a minor task related mainly to choosing the proper mesh.

As it was demonstrated in the previous chapter, the vortex circulating behind the monolith plays a minor role in defining the combustion properties of the monolith.

It was still open the question whether the "inlet" part of the mesh was important in defining the velocity profiles of the simulated micro-combustor, so it was meshed a geometry consisting of the inlet zone and the channels.

The whole geometry was divided into four parts by orthogonal axes of symmetry but even with this simplification the mesh was a cumbersome 1,2 milion cells: for this reason only a constant density simulation based on air was performed.

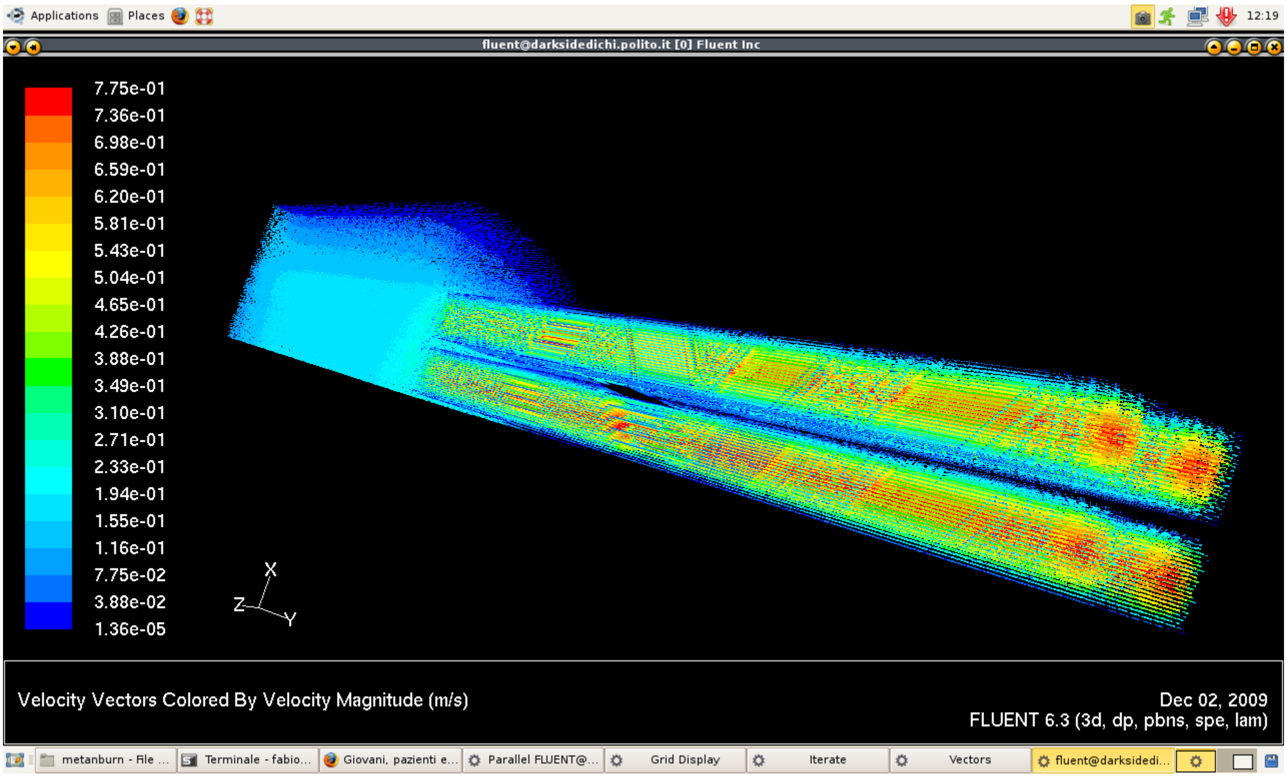

Figure 63: velocity vectors for a simulation with an inlet zone included

Result showed in Figure 63 confirms the fact that the same amount of gas moves between the channels so a further mesh simplification could be made without affecting combustion phenomena; on the other hand the computational complexity that had been removed left room for analyzing the heat transfer between the monolith to the external quartz tube by means of conduction through the vermiculite coating.

9.3.1 Mesh geometry and model implementation

The meshes created were based on a the following geometry

Length	25 mm
Width	5.5 mm
Number of channels	16
Silicon carbide layer thickness	0.1 mm
Internal silica glass tube diameter	10 mm

Table 12 monolith's main dimensions

When building the model of the micro-combustor we took into consideration that a square has 4 planes of symmetry that can be used to reduce the number of cells in the model; in our case, only the two median axes were chosen for geometry reductions because if diagonals had been used they would have introduced oblique faces that would have distorted channel meshes(figure 64).

The first mesh was made with 654000 cells and the vermiculite zone was meshed with the simple (and easier to be implemented) pave scheme(Figure 65).

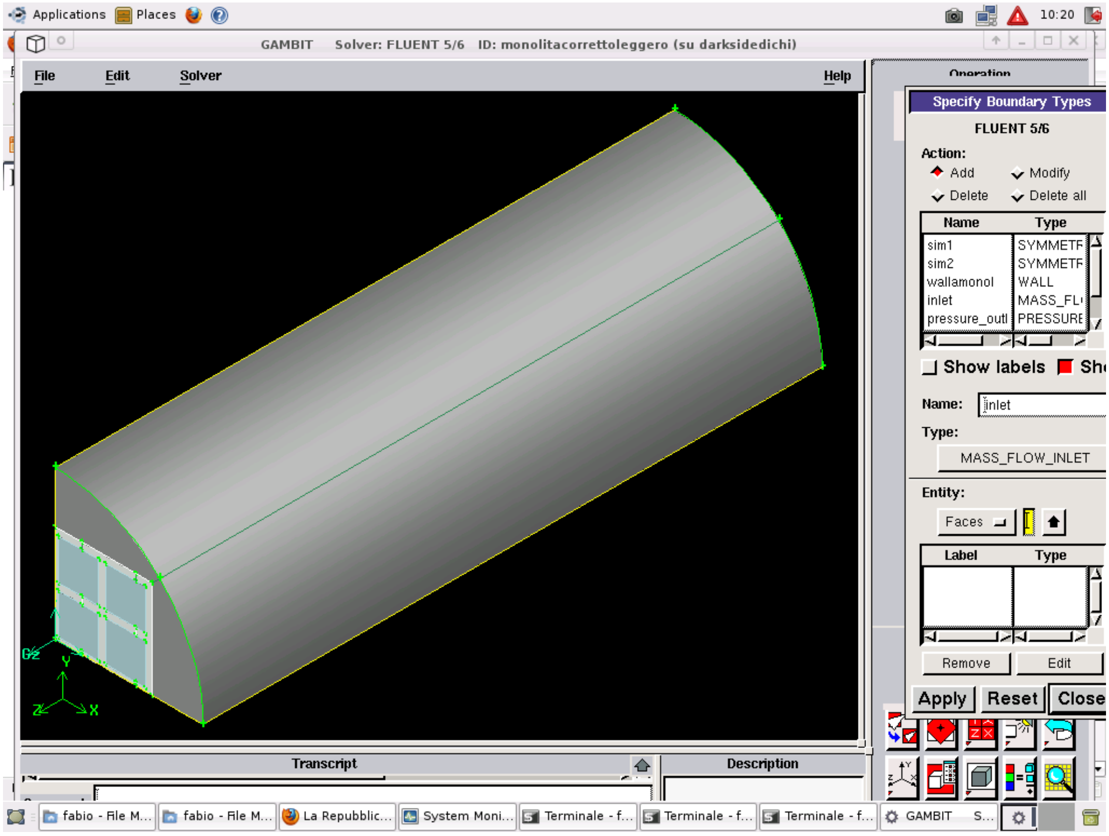

Name	Type
sim1	SYMMETF
sim2	SYMMETF
wallamonol	WALL
inlet	MASS_FL
pressure_outl	PRESSURE

Name: inlet

Type: MASS_FLOW_INLET

Entity: Faces

Figure 64: Gambit® drawing of simulated domain

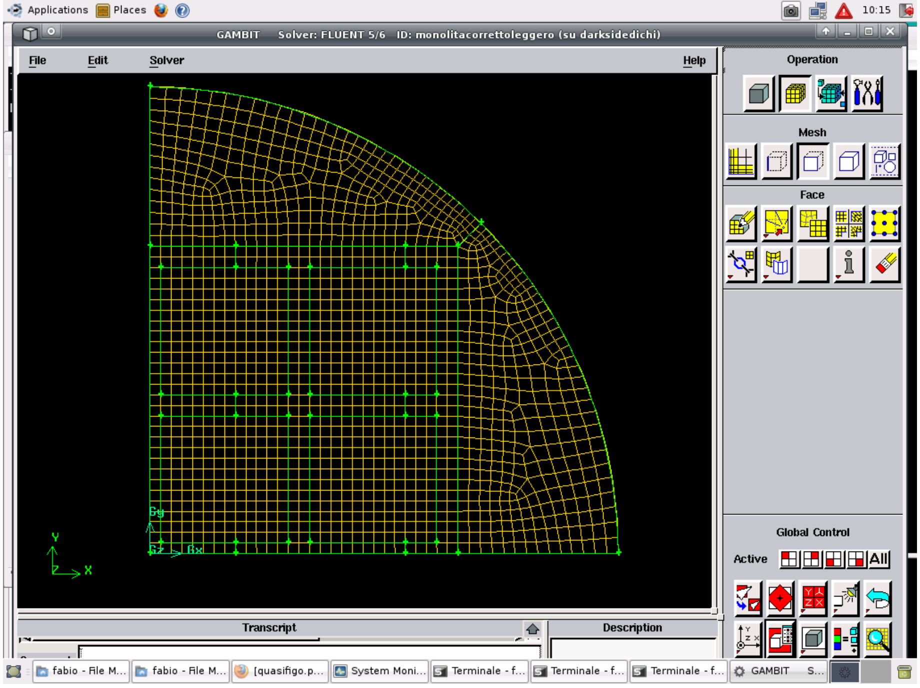

Figure 65: Frontal view of the first mesh

To use this new geometry the thermal conductivity of the vermiculite layer and the heat transfer at the silica wall had to be known: available literature data offered somewhat scattered heat conduction values for vermiculite ranging between 0.006 and 0.01W/m^2/K [13]

The value of 0.006 W/m^2/K was chosen because it is known that thermal expansion caused by temperature dramatically improves vermiculite insulation capacity.

In order to consider the heat escaping through external silica tube towards wall conduction boundary it was used a radiation model based on the Stephan-Boltzmann law.

$$\overset{\circ}{Q} = \varepsilon\sigma * A * \left(T_w^4 - T_{ov}^4\right) \tag{13}$$

Where T_w and T_{ov} are the temperature of the silica wall and of the oven respectively; σ is the Boltzmann constant 5,6696 * 10^{-8} [W * m^{-2} *K^{-4}]; ε is the specific emissivity of the material.

To specify the right emissivity over a wide range of condition an UDF was written to interpolate between known values of emissivity introducing also a lower and an upper emissivity limit in order to keep the linear interpolation inside physical constraints.

$$\sigma = 0,0007 * T + 1,1877 \tag{14}$$

The high and low temperature caps used were respectively:

$\sigma = 0.95$ if $T < 340$ K
$\sigma = 0.1$ if $T > 1550$ K

Preliminary simulation were run to estimate thermal phenomena by flowing hot air while keeping walls cold.

Results showed that the heat escaping from the monolith as a whole was significant but at the same time the SiC monolith was much more conductive than vermiculite so that the 4 channels were almost in the same thermo-chemical state.

If the assumption of adiabatic condition could be made, one channel simulation would be enough detailed to describe the system; this is not the case anyway the uniformity effect between the channels due to SiC helps data gathering so the results obtained from one channel can be applied to the others.

This results are reported in the following 2 figures.

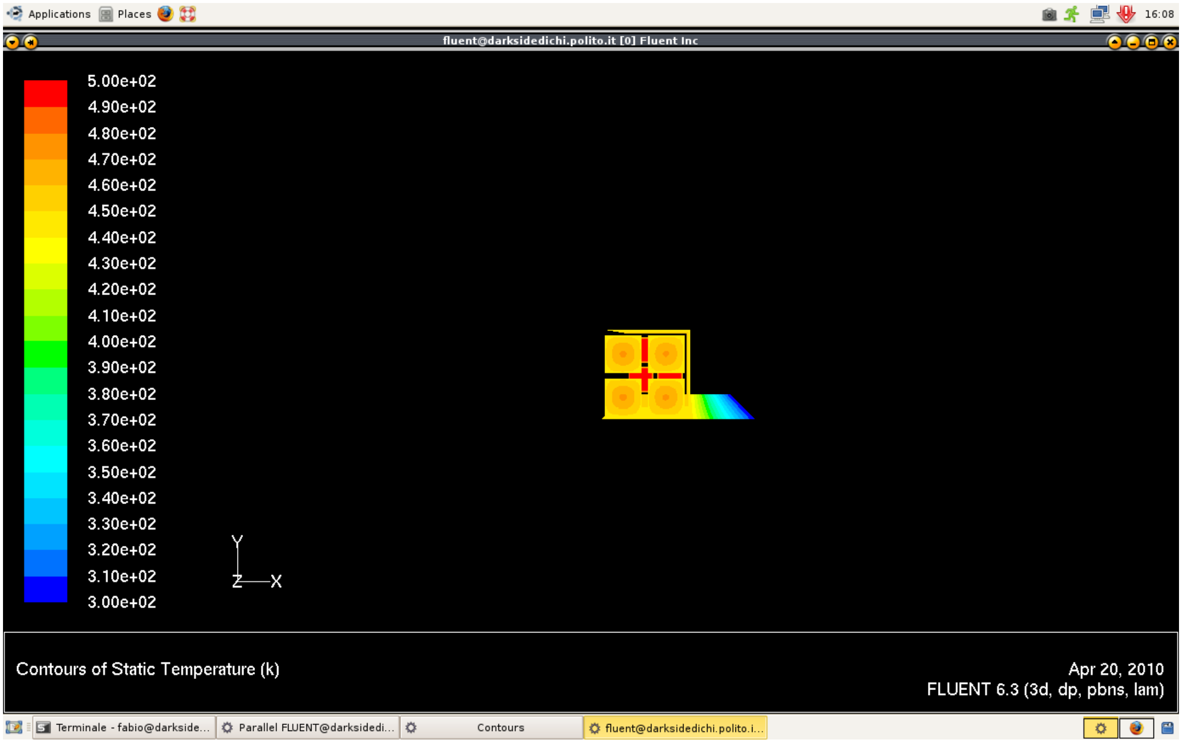

Figure 66: Frontal view of heat dissipation virtual experiment: channels are equal.

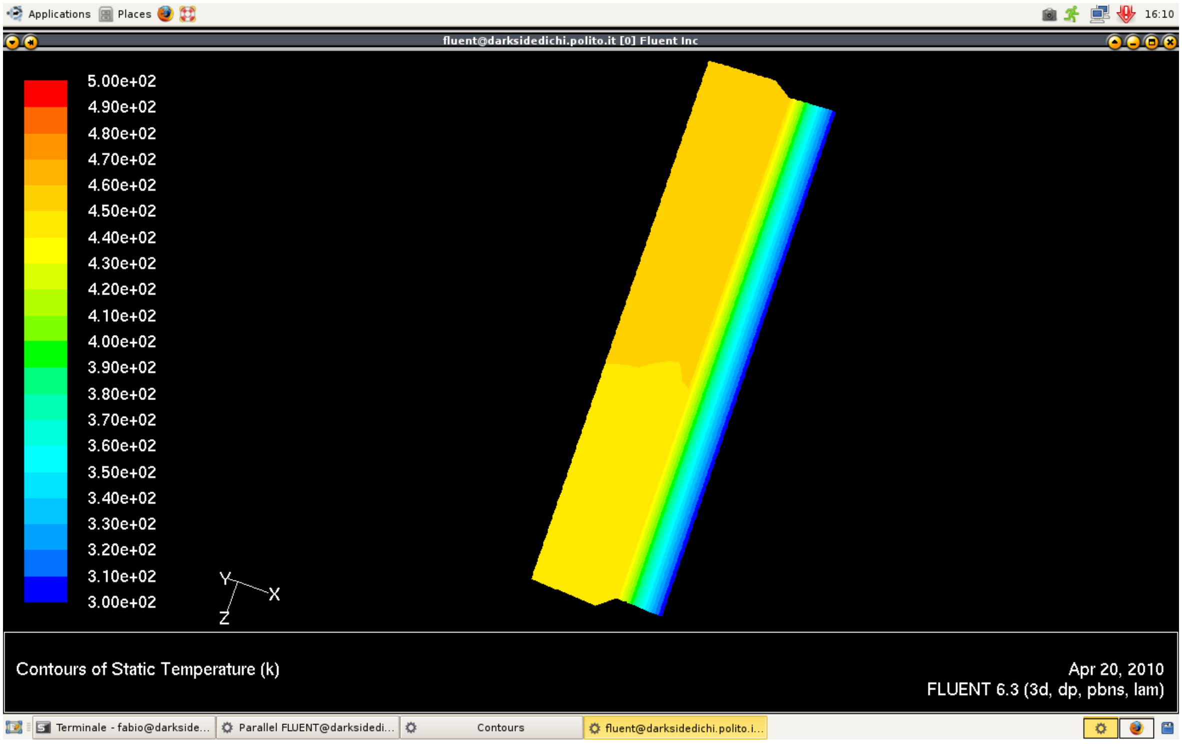

Figure 67: Side view of heat dissipation experiment showing vermiculite thermal gradient and constant temperature inside SiC

For what concerns the reaction kinetics Mars van Krevelen model 4 (which includes a slow desorption mechanism for products) was chosen.

$$R = \frac{k_1 p_{CH4} k_2 p_{CH4}}{2k_1 p_{CH4} + k_2 p_{CH4} + k_1 p_{CH4} k_2 p_{CH4} / k_3} \qquad (15)$$

This model was fitted with these parameters:

E_1	24.4 kJ mol^{-1}	k^{∞}_1	0.375 mol g^{-1} s^{-1} bar^{-1}
E_2	33.8 kJ mol^{-1}	k^{∞}_2	23.1 mol g^{-1} s^{-1} bar^{-1}
E_3	8.89 kJ mol^{-1}	k^{∞}_3	$2.21*10^{-4}$ mol g^{-1} s^{-1}

Table 13: Kinetic parameters for Mars van Krevelen model 4

This equation was favoured over MvK3 model since the latter gave numerical quirks when a fitting was tried for temperatures and pressures different from the ones of the experimental kinetic tests; MvK4 was the second best fitting and was reliable beyond experimentation field as well.

Given the high temperature reached by the gas near walls it was very likely that, as occurred in the 2D case, also homogeneous oxidation happened and for this reason the homogeneous mechanism taken from [6] was implemented inside the model

$$R_{CH_4} = k \cdot c_{CH_4}^{\ \ 0.96} \tag{16}$$

The parameters of this model are a pre-exponential constant of 4532300 kmol/s and an activation energy of 130.66 kJ/mol.

The inlet composition was fixed as very lean: 2.82% weight basis of methane in air (that is 5% mole basis)and mass flux was set at $1*10^{-3}$ g/sec per channel which represent the gas inputs of a real monolith fed with that mixture: data obtained with the experimental apparatus will be confronted with the simulation results.

Data reporting is a special issue of 3D simulation because temperature and concentration fields develop in the space while the plots are just 2D objects: for this reason a choice of most important solution features must be done.

Building on the experience done with non reacting warm flows (figures 66,67) a virtual line was placed at the centre of a inner channel which was used as a support onto which the 3D solution could be evaluated.

9.3.2 Results of 3D simulation

As first the grid independence of our model was tested by running a simulation taking note of some important parameter and running a further simulation with a much higher cell count (cell pass was halved so in a 3D geometry cell count was multiplied by 8).

Using outlet temperature for comparison we noted that 654,000 cells was the minimum amount of cell acceptable because they give an error of about 8% that is the same order of magnitude of errors made with the experimental apparatus.

As seen in figure 69 and figure 70 the convergence history of the computational system when the surface reaction is turned on reaches steady state after some dampened ocillations but this does not mean that the real system is in an oscillating state (Figure refers to inlet gas and outer oven set at 750 °C).

Reaction rates were calculated by means of conversion at the end of the monolith; because gaseous profile had a parabolic profile a mass- weighted average scheme was adopted to evaluate exactly the mean methane flow.

$$\frac{CH'_{4\_in} - CH'_{4\_out}}{CH'_{4\_in}} = \eta_{CH4} \tag{17}$$

The results obtained are remarkable because the surface combustion kinetic calculated by analysing the Pd /CeZrO$_2$ powder is much higher than the one assessed by the experimental result.

Figure 68 shows that the methane conversion is considerably higher in the CFD simulation than in the real experiment.

The activity loss is a common outcome that occurs when the performance of a powdered catalyst is compared with the same catalyst deposited onto a surface: this happens because the monolith's surface (especially silicon carbide) inhibits spikes growth and this results in poorer specific area and poorer dispersion of the catalyst.

At higher temperatures the two curves of modelled and experimental conversion converge again and this is a sign that heat losses slow reaction rate:

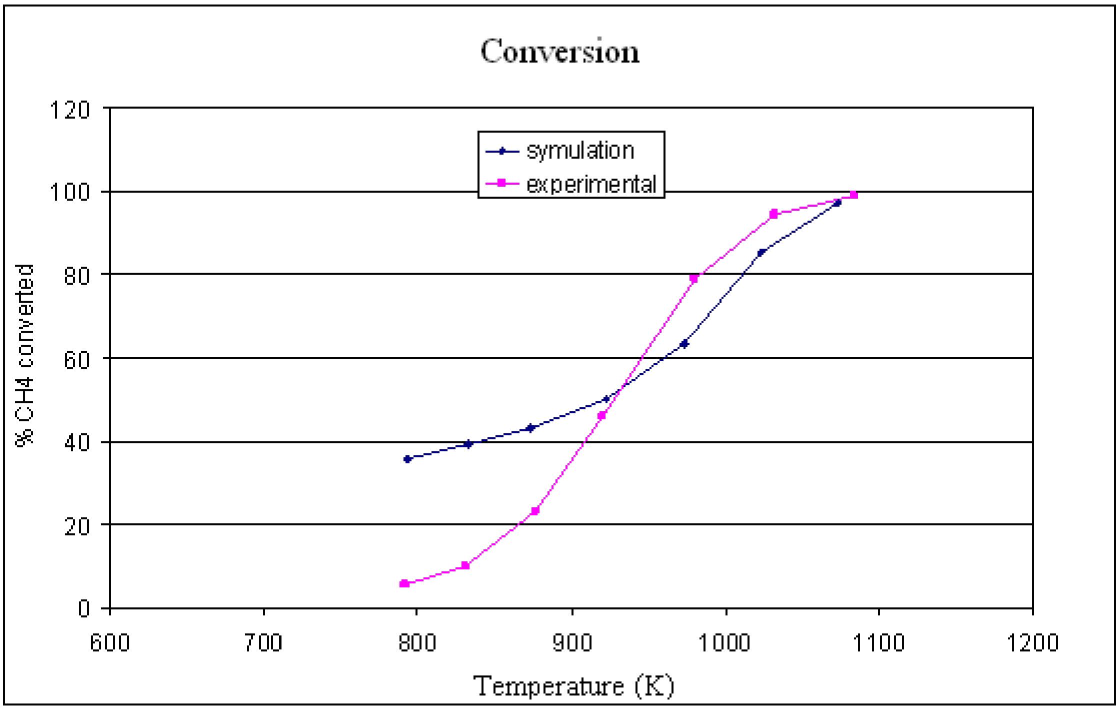

Figure 68: Methane conversion plot with CFD and experimental results

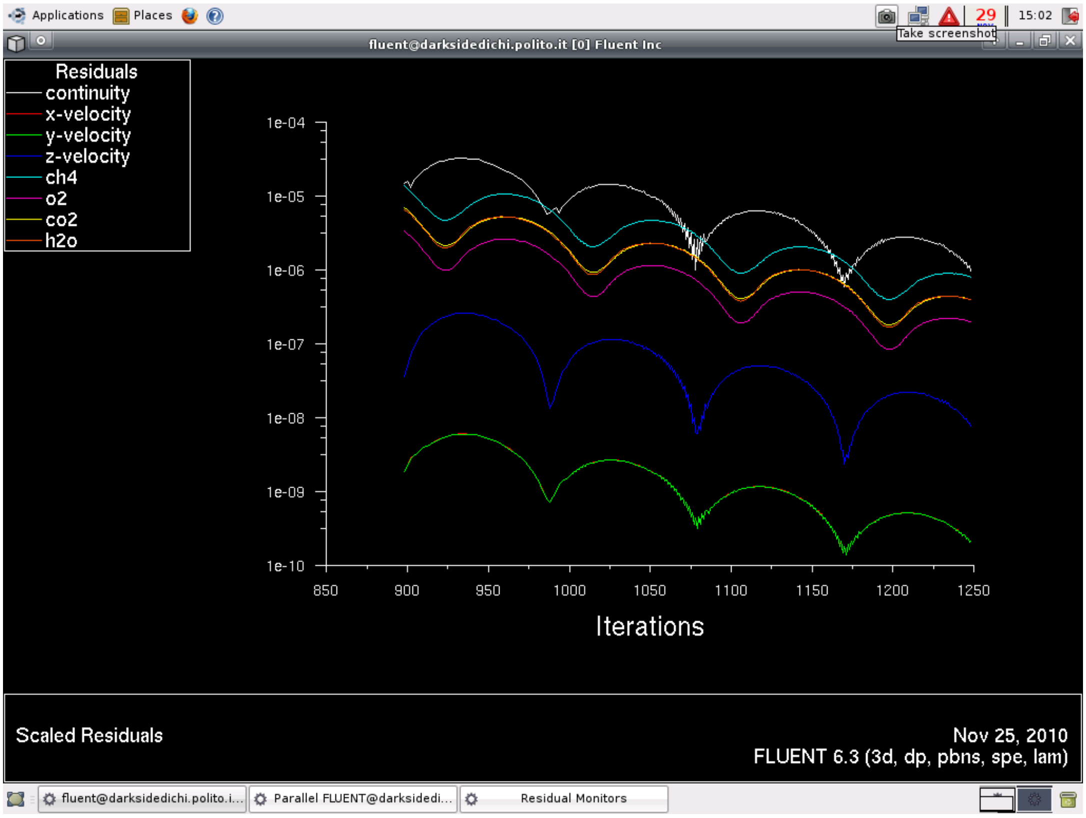

Figure 69: Under some circumstances Fluent reaches convergence through damped oscillations

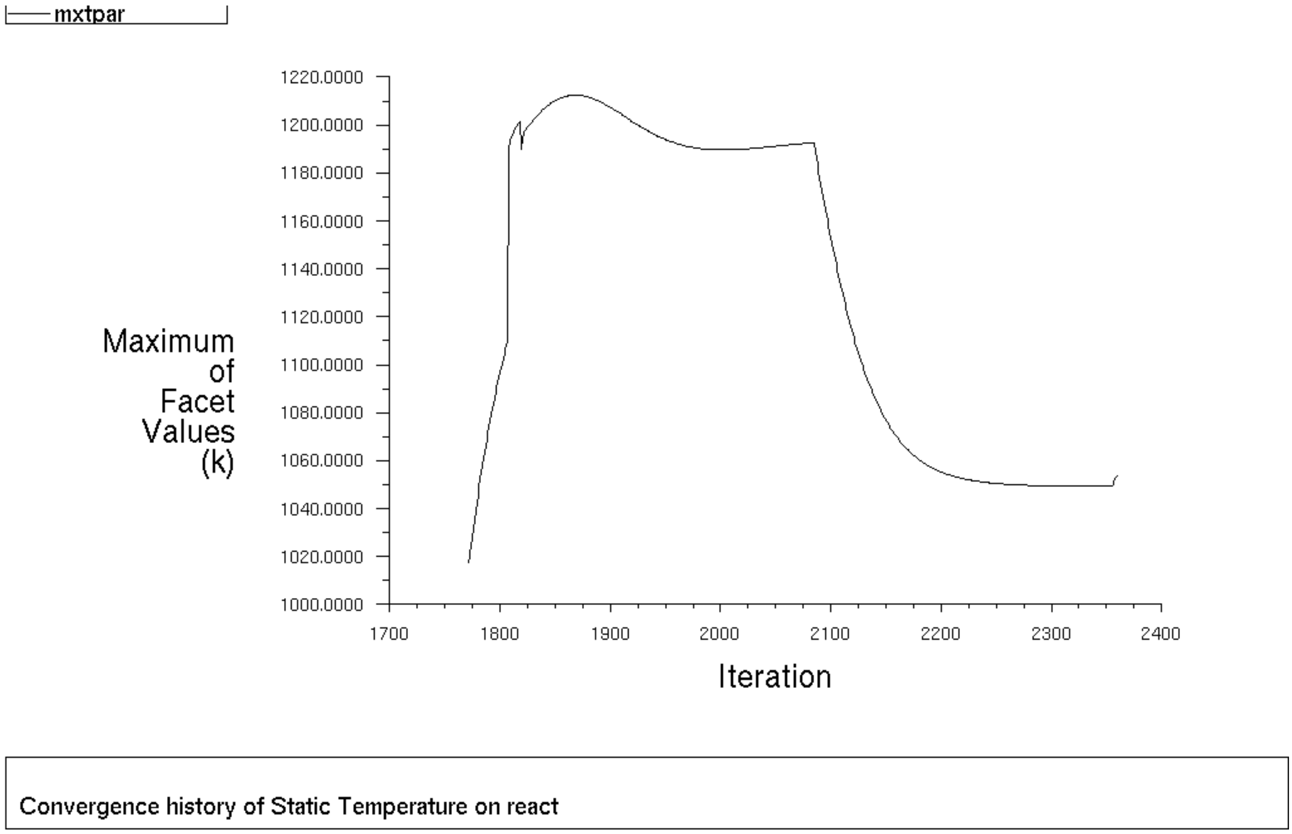

Figure 70: Plot of maximum wall temperature behaviour occurring when starting from a lit monolith surface catalysis is turned off

In figure 70 a particular simulation was performed: starting with the catalytic combustion model turned on the model converges to a lit state (90% methane burnt).

In the second part of the simulation the Surface Reaction Model is turned off keeping active only the homogeneous combustion mechanism: the result is that the temperature, not sustained by catalytic oxidation, drops to just 1060 K and combustion stops (more than 90% of methane doesn't react).

As a matter of facts, unlike the 2D model and the experimental apparatus, the 3D model doesn't feature a stable light state because computed heat losses through the vermiculite layer are higher than reality.

The most probable cause is that vermiculite increased a lot its insulating power during expansion so the thermal conductivity data found in literature and implemented inside the model were probably too high (they may refer crude vermiculite).

In order to verify this a new set of simulations was deployed turning the vermiculite conductibility to zero in order to virtually recreate the adiabatic conditions of the axial-symmetric simulations reported in the previous chapter.

The results again showed that, if all the heat produced is kept inside the micro-combustor, then combustion reactions are stable and occur in the first part of the reactor as shown in the following figures: (71 to 75)

For this reason a new study was carried on to asses the best fitting value thermal conductibility for vermiculite.

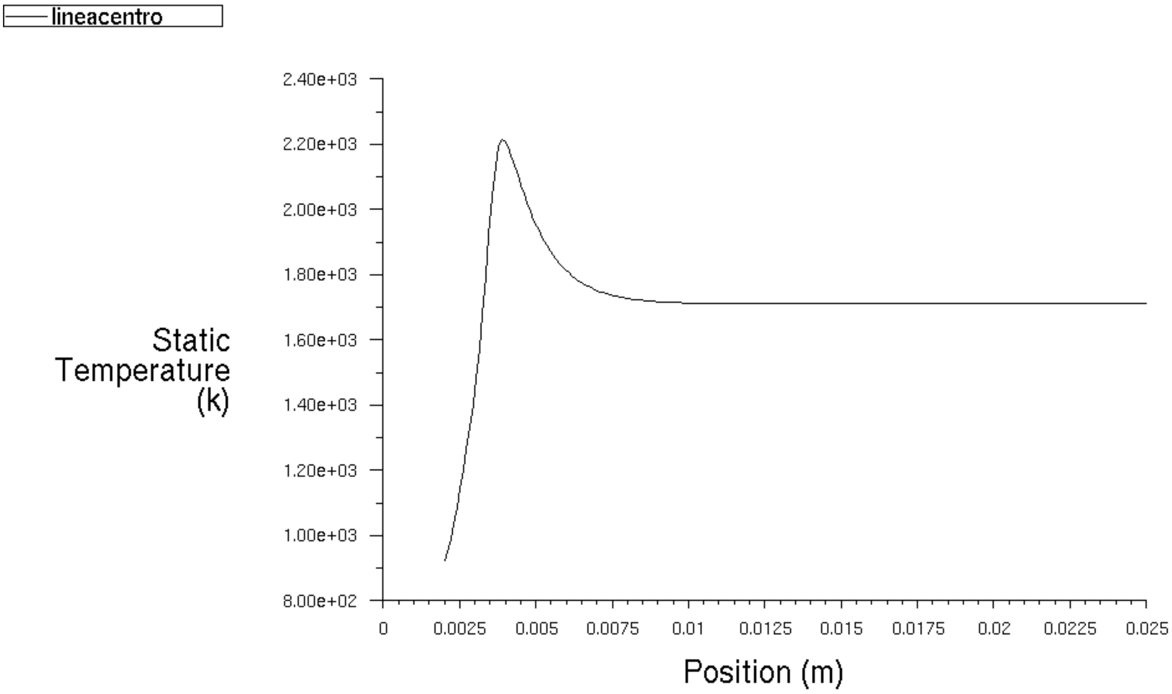

Figure 71: Plot of temperature profile along monolith length for adiabatic case.

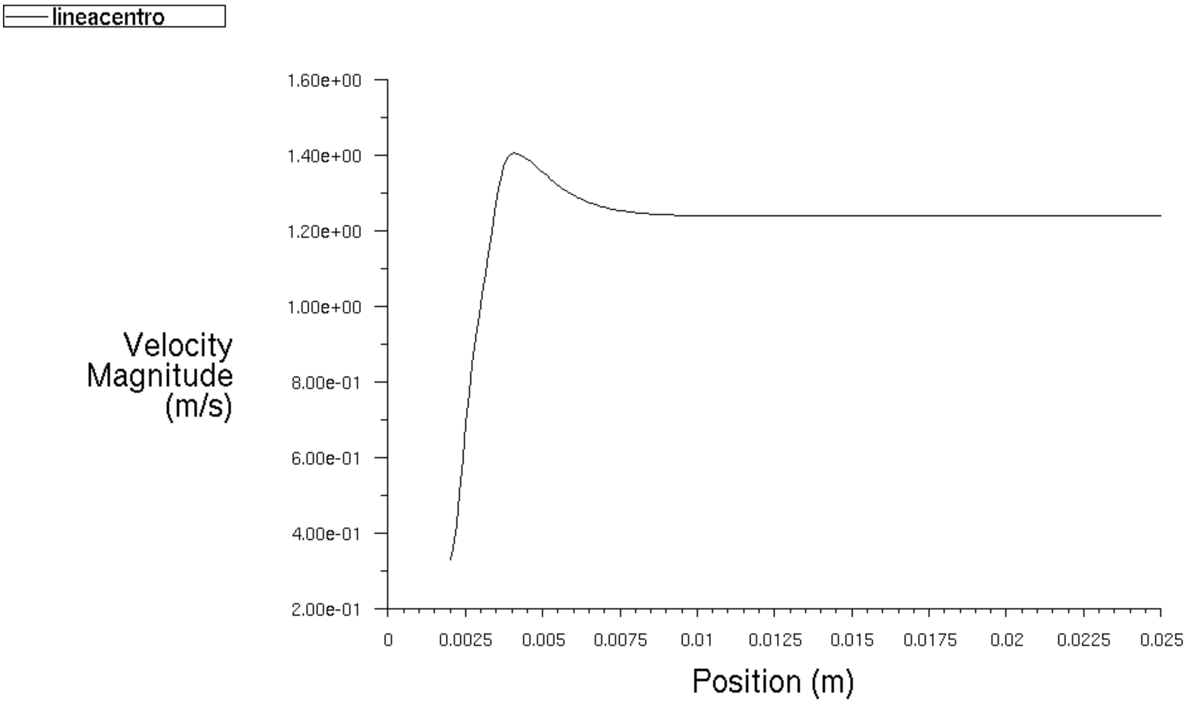

Figure 72: Plot of velocity profile along monolith length for adiabatic case.

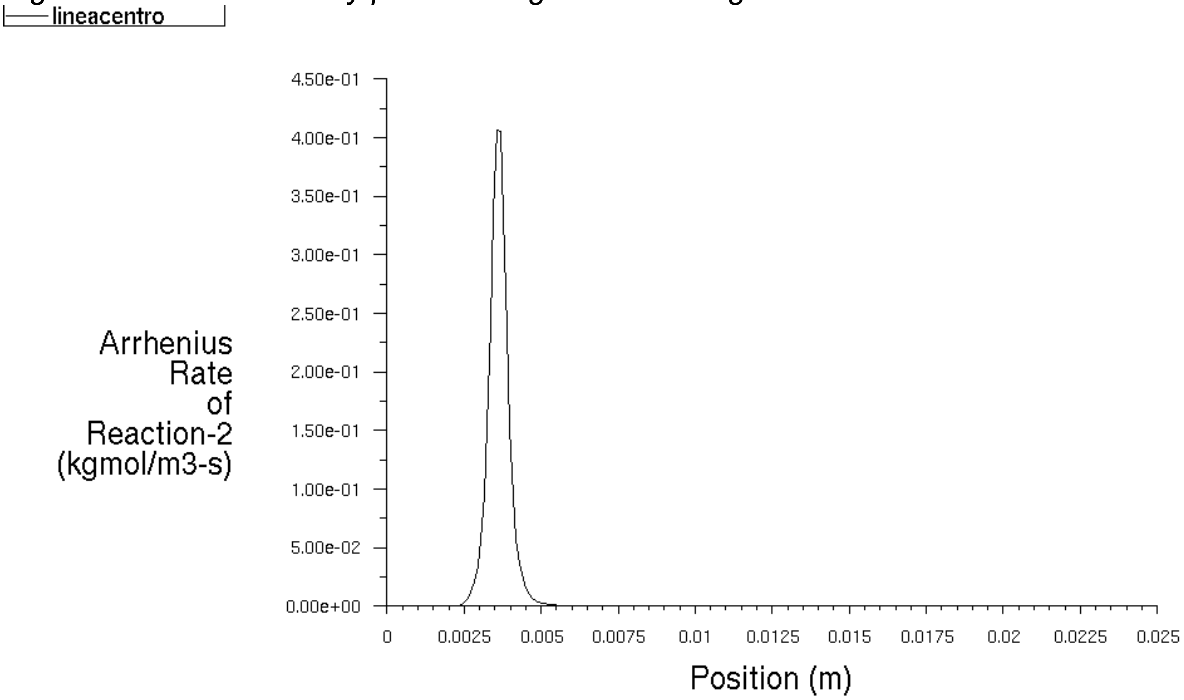

Figure 73: Plot of reaction rate profile along monolith length for adiabatic case.

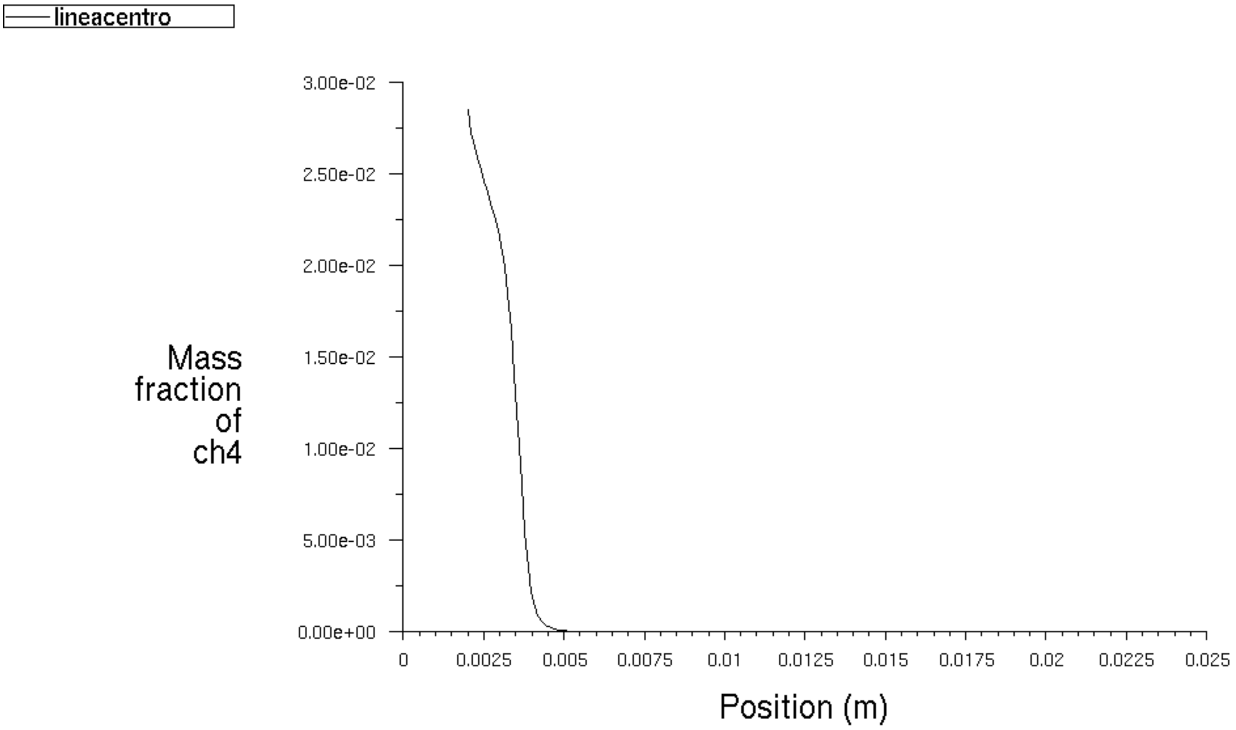

Figure 74: Plot of methane concentration profile along monolith length for adiabatic case

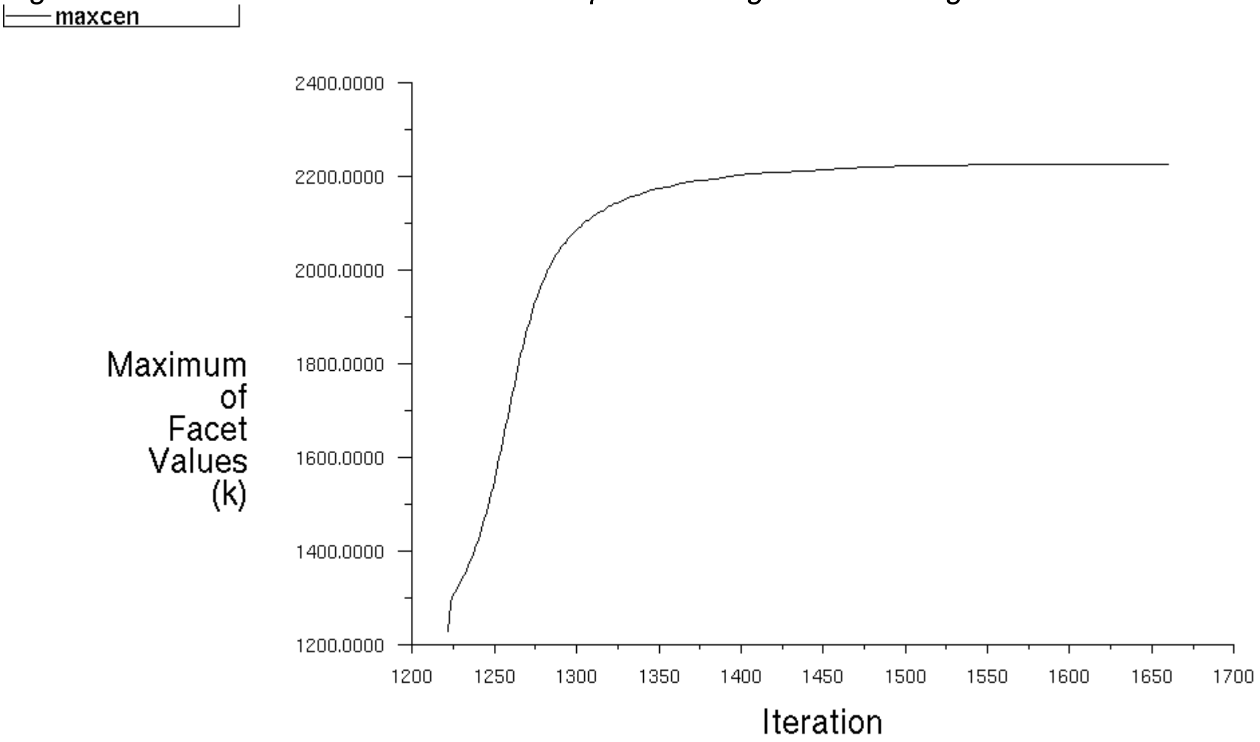

Figure 75: Plot of maximum temperature value at any iteration for adiabatic case.

9.3.3 Model tuning

Because an enhanced detail in conduction layer was needed, a new mesh was generated which was more detailed in the combustion zone and in the vermiculite layer: as seem in figures (76,77) this zone was remodelled using a structured approach and the outer vermiculite boundary was meshed unevenly in order to assure the maximum grid performance where the vermiculite layer was thinner (and the heat escape was obviously more relevant).

The resulting grid weighted a 933888 hexahedral Cells.

Test and simulations aimed at evaluating the best fitting vermiculite thermal conductibility were made on uncatalyzed monoliths to avoid the error caused by the activity loss occurring in the deposited catalyst: this decision removed a source of uncertainty.

As trial values came near a fair estimation of vermiculite heat conduction, the model behaves like it senses the presence of a lit quasi- solution in which cooling rate decreases sensibly; after a further cooling of about 100°C the monolith converges again normally as seen in figures 79,80.

Figure 78 shows how this quasi-solution is represented in the residual plot: after first instabilities the residuals seem to converge to a lit state although very slowly, then they start to rise again to a maximum which represents the combustion reaction blowing off; after this event, simulation converges very quickly as in a cold flow due to the practical absence of chemical reaction.

The best vermiculite heat conduction value was determined to be surprisingly low: 0.00025 W/m/K.

This fitting value is so low that some doubt arises about its physicalness because it indicates that when vermiculite expands, its insulating power should increase a lot making the monolith a quasi adiabatic system.

Taking the final simulation data with the necessary scepticism, once lit the monolith shows a behaviour that is in agreement with the experimental data in which combustion starts at 700°C and shuts down at 370 °C keeping a nearly complete combustion rate for almost all the temperature range in which is lit; computed cases instead feature shutdown at 400°C and lightoff at 600°C: these errors are referable to the relatively simple combustion model used (figure 86).

At 450 °C as shown by figures 81, 82, 83 oxidation completes within the first third of the monolith and explains why an experimental sawn monolith of half length is able to carry on the combustion and to obtain about the same performances of the full monolith.

On the other hand if simulation temperature is raised, combustion takes place earlier inside the monolith with temperature, reaction rate and CH_4 moving to the first part of the monolith.

However this simulation suggests that monoliths with length shorter than 10 mm will get evident lower performances.

Moreover simulations have shown that near the point of cold extinction combustion starts to be incomplete (some methane escapes as reported in figure 81)in the same way that happened to the experimental case.

The tests conducted to calculate the cold branch of the hysteresis plot showed that a slow homogeneous oxidation takes place; however this is sufficiently high to get a small device heating as showed by Figures 84 and 85 (inlet temperature 550°C).

In Figure 84 is reported the temperature field that passes through the monolith showing that all the thermal gradient is located in vermiculite

This phenomenon is even more evident inside a lit monolith and is caused by the great difference of thermal conductibility between SiC and vermiculite.

If the monolith material is changed from SiC to cordierite the difference of conductibility remains very large and this is why a cordierite monolith has a similar wide hysteresis both in the carried out experiments and in the run simulations.

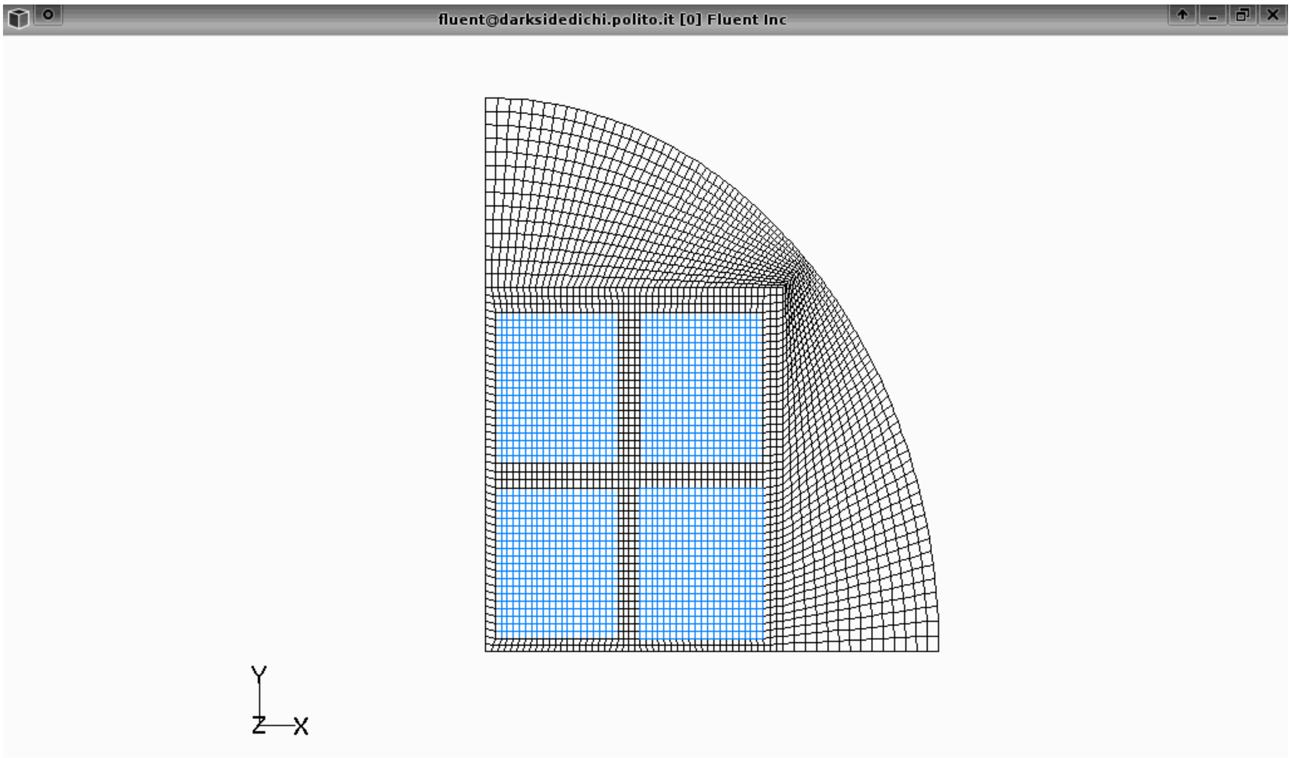

Figure 76: the definitive full structured mesh

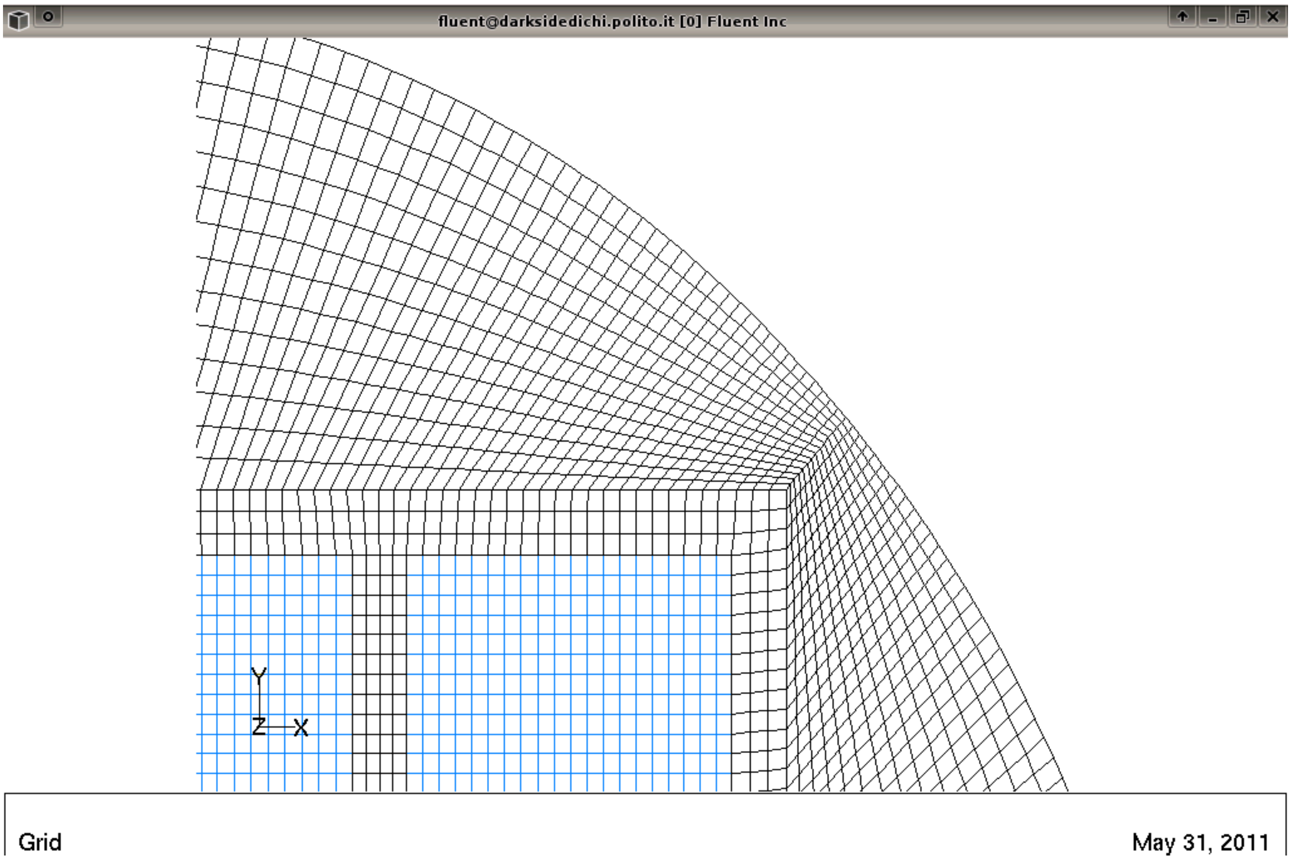

Figure 77: Detail focused on vermiculite thinner region.

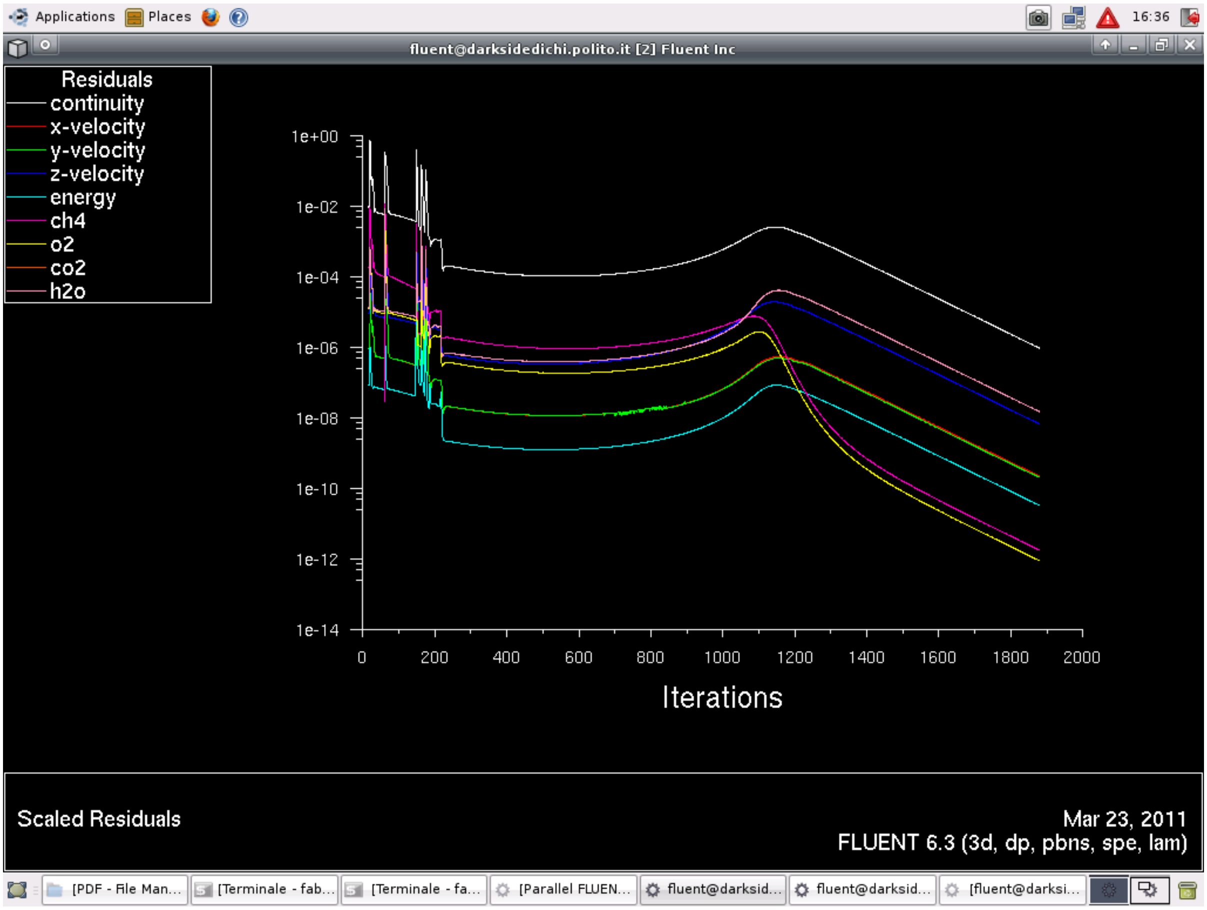

Figure 78: Residuals convergence for a blowing out reaction simulation

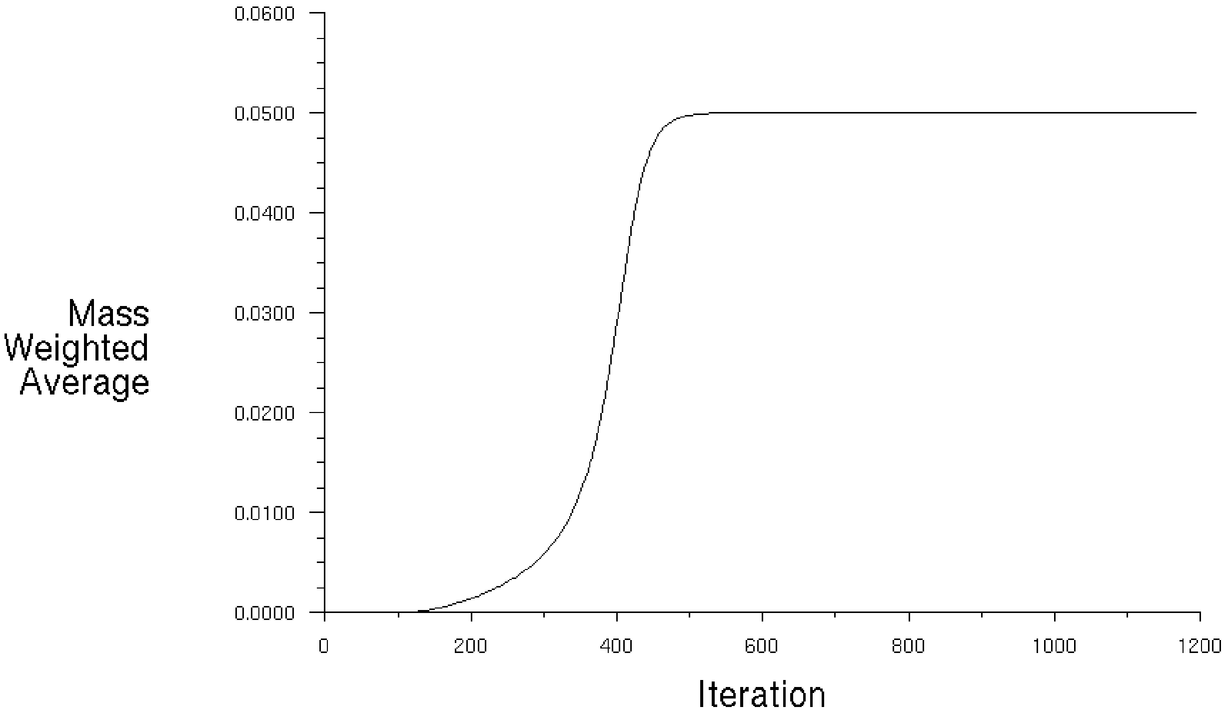

Figure 79: Solution evolution of methane escape for a blowing out reaction simulation

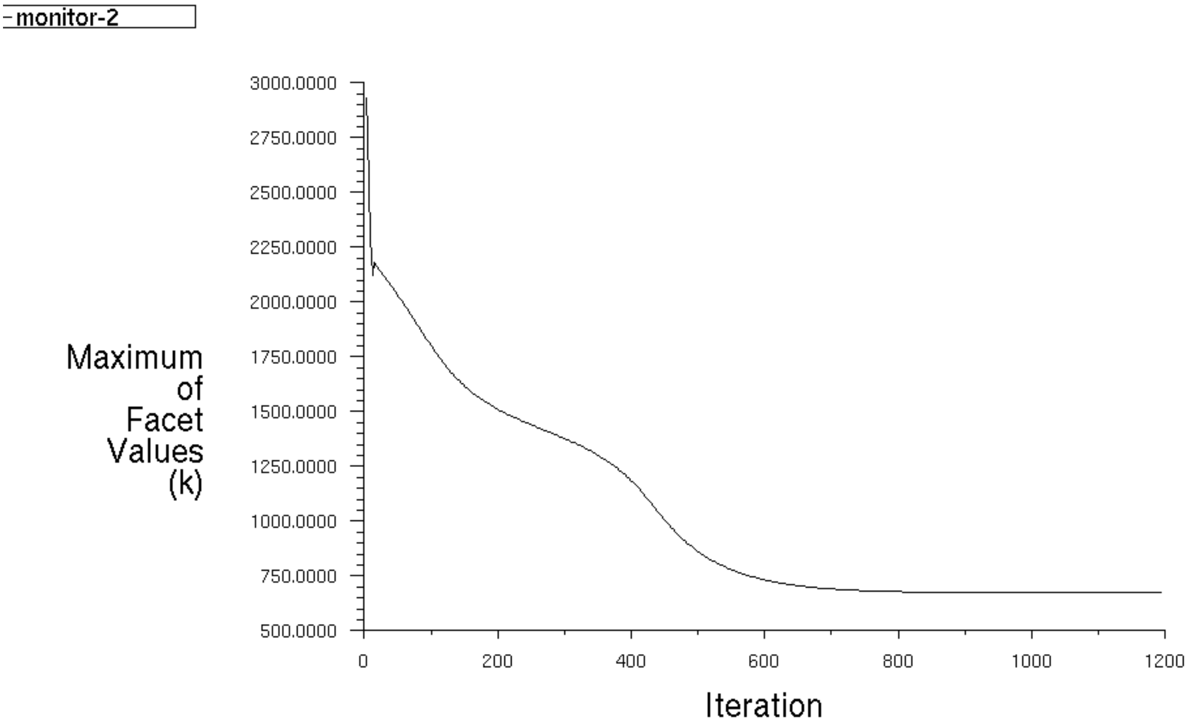

Figure 80: Solution evolution of central maximum temperature for a blowing out reaction simulation

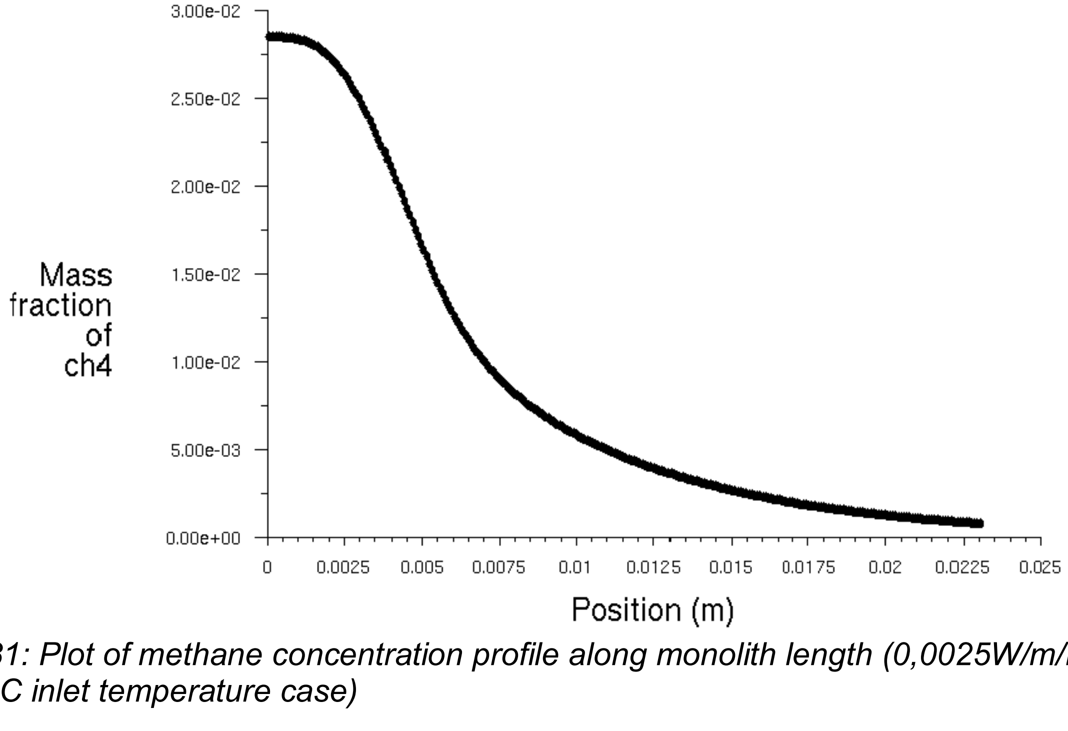

Figure 81: Plot of methane concentration profile along monolith length (0,0025W/m/K and 450 °C inlet temperature case)

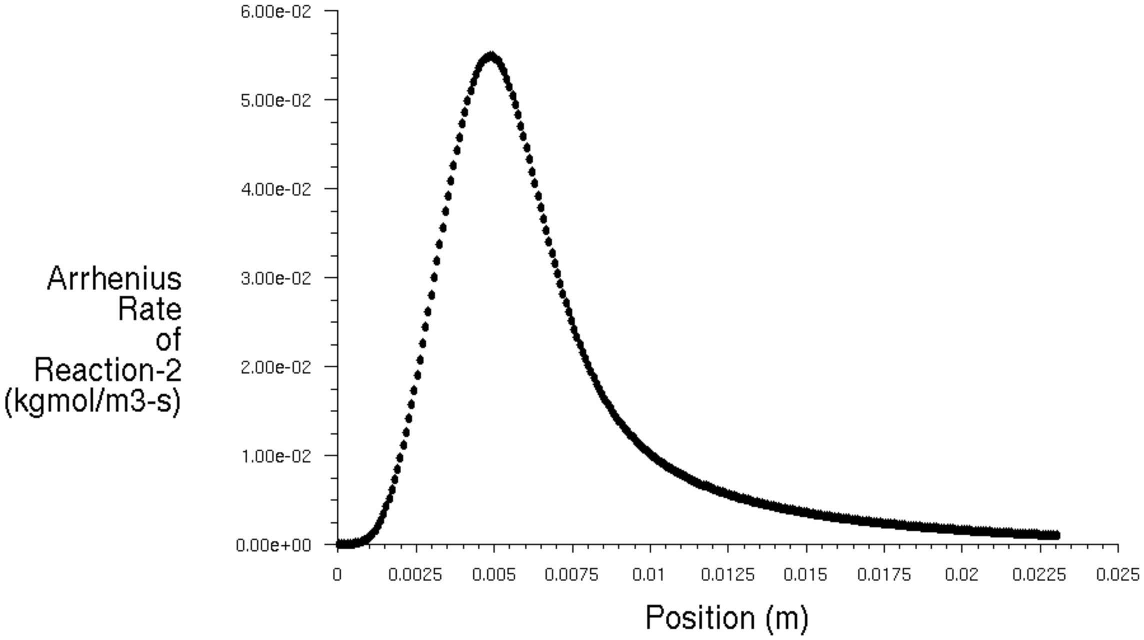

Figure 82: Plot of reaction rate profile along monolith length (0,0025W/m/K and 450 °C inlet temperature case)

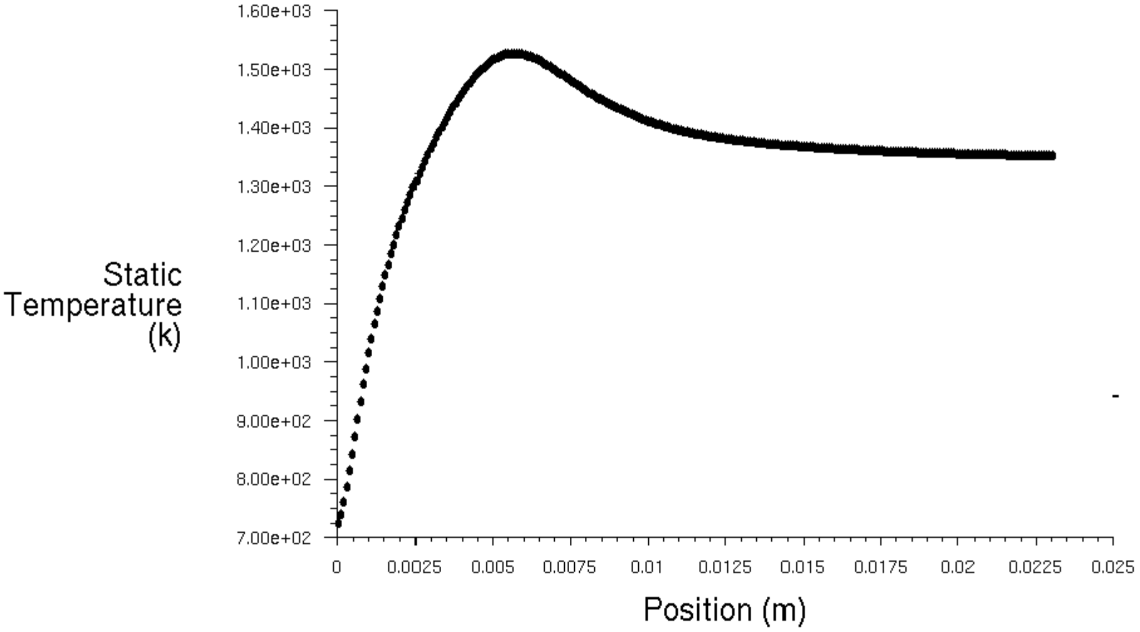

Figure 83: Plot of temperature profile along monolith length (0,0025W/m/K and 450 °C inlet temperature case)

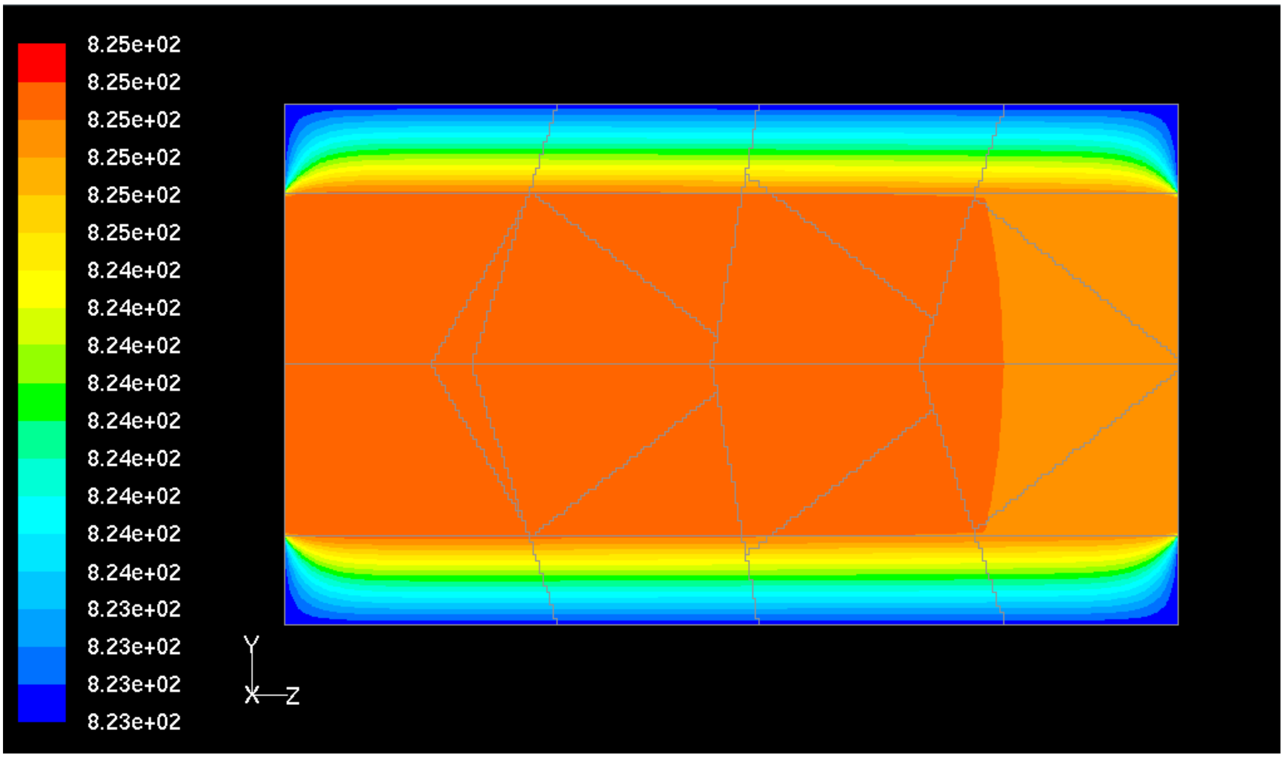

Figure 84: Temperature contours of monolith and vermiculite (middle section).

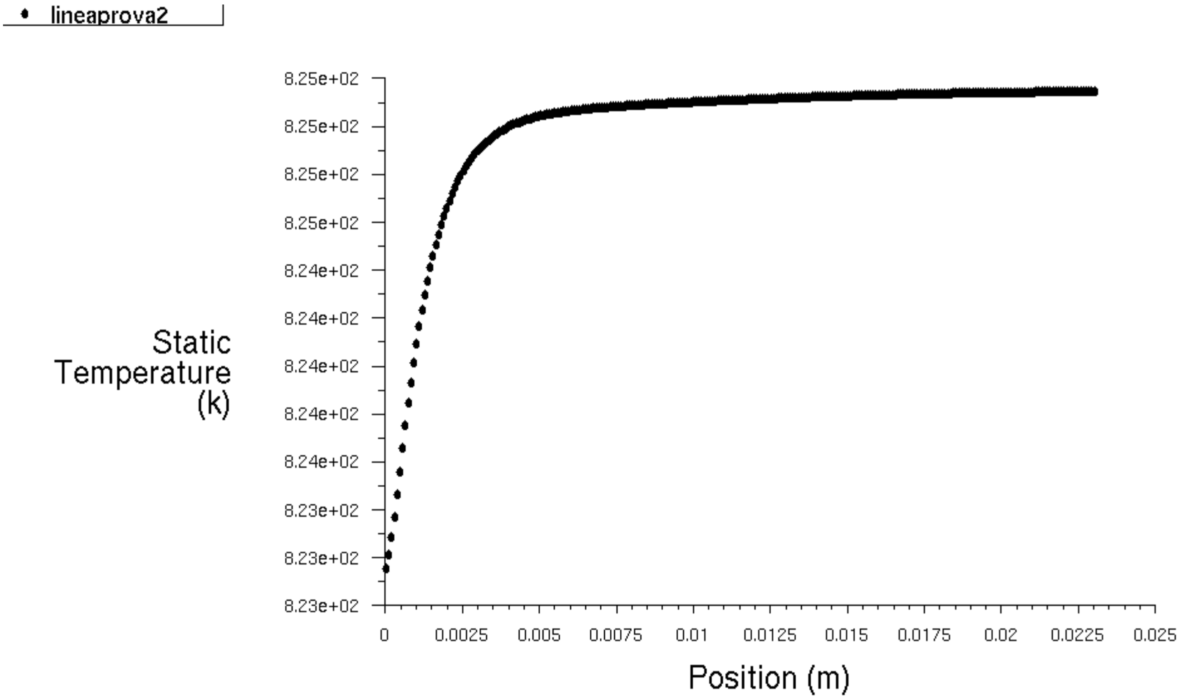

Figure 85: Channel centre temperature during off state (inlet temperature 550°C)

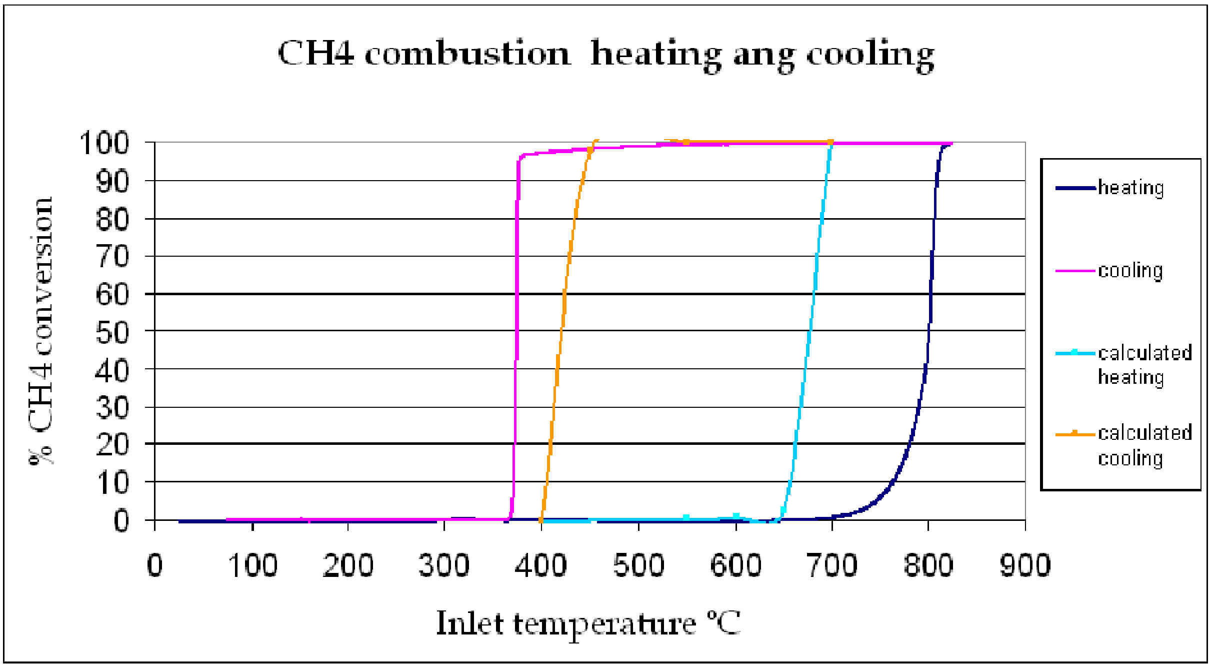

Figure 86: Simulated and experimental conversion hysteresis plot; catalyst considered was 2%Pd/$Ce_{0,33}Zr_{0,66}O_2$

9.3.4 Alternative hypothesis to explain micro combustor hysteresis

First of all it must be considered that the heat conduction value that reproduces at best the thermal hysteresis of the modelled micro combustor was about one order of magnitude lower than literature about vermiculite.

The first explanation of this phenomenon was that literature data were supposed to be sampled from unexpanded vermiculite: so vermiculite expansion was the cause of this sharp rise in performances.

But, at the end of the last year of PhD, a test carried on a micro monolith although in a different fluid dynamical configuration showed a free flame just after the monolith.

Depending on gas rates and oven temperature the flame leaned to the monolith at low flows or was free floating at about 1 cm after the monolith exit at high gas rates.

Test done using a catalyzed monolith showed no flame after the micro combustor (proving that methane was oxidized inside the device) but had their hysteresis blew off at higher temperatures.

So there is also the possibility that uncatalyzed micro combustor acts only as a physical support stabilizing the flame and preventing it from flashing back inside the quartz tube.

Under this hypothesis the CFD model initialized with the vermiculite thermal conductivity of 0,006 W/mK found in literature gave these two correct results:

- Catalytic combustion occurs inside the monolith
- Homogeneous reactions extinguish when microreactor inner walls aren't catalyzed

To complete this alternative explanation, a description of how the micro combustor hysteresis generates is hereinafter reported:

1. Gas mixture enters flammability limits during heating
2. As gas mixture reaches the auto ignition temperature, combustion starts.
3. The oven is turned off
4. Despite initial cooling, device continues burning because flammability limits are larger than auto ignition ones

5. Finally, when gas temperature is sufficiently low, gas mixture exits the flammability limits and blows off

References of chapter 9

1. D.L. Marchisio, A.A Barresi: *Chemical Engineering Science,* **64:** 294 (2009)
2. Han S. Kim, Vaibhav K. Arghode, Ashwani K. Gupta: *Int. Jou. of Hydrogen Energy*, **34**: 1045 (2009)
3. S. Specchia, M.A. Ahumada Irribarra, P. Palmisano, G. Saracco,V. Specchia: *Industrial & Engineering chemistry research,* **46**: 6666 (2007)
4. S. Specchia, A. Civera, G. Saracco, V. Specchia: *Catalysis Today*, **117**: 427 (2006)
5. A. Di Benedetto, V. Di Sarli, G. Russo *Catalysis Today,* **147S:** S156 (2009)
6. K.Gosiewski, A. Pawlaczyk, K. Warmuzinski, M. Jaschik: *Chemical Engineering Journal*: **154** (2009)
7. Di Benedetto, V. Di Sarli, *Ind. Eng. Chem. Res.*, **49:** 2130 (2010)
8. Stefano Tacchino, Luigi D. Vella, Stefania Specchia *Catalysis Today in press* (2010)
9. A. Di Benedetto, V. Di Sarli, G. Russo, *Catal. Today:* in press (2009)
10 Symeon Karagiannidis, John Mantzaras, Gregory Jackson,Konstantinos *Boulouchos "Hetero homogeneous combustion and stability maps in methane-fueled catalytic microreactors"*
11. F.Conti, A. Rossati, L.D. Vella, S.Specchia, V. Specchia: *Industrial & Engineering chemistry research in press* (2009)
12. F.Conti, A. Rossati, L.D. Vella, S.Specchia, V. Specchia: *XXXII Annual Meeting of the Combustion Institute Italian Section (Napoli (Italy))* pp.II-2-II-8 (2009) 14
13 Mosilia,Victor A.: *"La vermiculite: cenni storici, caratteristiche, proprietà":* Milano Hoepli, copyr. 1967 15

List of symbols and acronyms of chapter 9

A = Exchange area [m^2]
Q' = Rate of heat exchange [W]
T = Temperature [K]
ε = Emissivity
σ = Boltzmann constant 5,6696 * 10^{-8} [W * m^{-2} *K^{-4}]
E =Activation energy
R = Universal gas constant 8,314472 J K^{-1} mol^{-1}
R_x = Reaction rate of component x [mol/s]
k = Kinetical constant
p_x = Partial pressure of component x [Pa]
MVK = Mars van Krevelen kinetical model
η = Efficiency of conversion
CH_4' = methane flow (integrated from inlet -outlet surface data) [mol/s]

10 CONCLUSIONS

The non mechanical conversion of thermal energy to electrical power is a goal chased by many material's scientist: at present the maximum peak temperature a single stage thermoelectric device can sustain is 350°C.

Although some other technical artifices could be used to make a thermoelectric device work, if the design of a compact and portable device is needed (which is the final aim of this PhD thesis) only catalytic combustion can oxidize fuel at such low temperature; to minimize pressure drop during preheating and burning a honeycomb configuration was chosen.

Research efforts were made to improve catalysis and to obtain a deeper knowledge of the catalytic system: main research fields have been about Manganese perovskites and Ceria Zirconia mixed oxides.

For both catalyst Palladium doping gave substantial improvements especially for the Ceria zirconia support which was chosen for the experimental micro combustion.

For any catalyst ($Ce_{0,33}Zr_{0,66}O_2$, Pd / $Ce_{0,33}Zr_{0,66}O_2$, $LaMnO_3$-$2ZrO_2$ and Pd / $LaMnO_3$-$2ZrO_2$) a detailed kinetical analysis was performed highlighting that reaction kinetics generally followed a Mars van Krevelen mechanism.

The simulation of a methane micro-combustor showed that even the very simple 2D axial symmetric approximation was able to feature the multiple state behaviour typical of the real system while three-dimensional simulations are needed to deliver the exact ratio between the catalytic and homogeneous combustion mechanism.

On the other hand, this PhD thesis confirms the hypothesis assumed by the existing literature about the lesser role the inlet and the outlet zones play in determining the flow profile and therefore the reaction rate; at the same time combustion readily shuts down after it exits the monolith.

As a natural continuation work the heat dissipation through the insulation was modelled because the high thermal gradients arose some doubt on the insulating power of the vermiculite.

For this reason, a three dimensional approach was used to capture the combustion behaviour and the heat conduction through vermiculite better.

Cold flow simulation demonstrated that gas flow through the channels was well balanced so also the meshing of the inlet part could be neglected.

This allowed for a domain restriction that allowed the implementation of very fine meshes: the final mesh weighted 933888 hexahedral cells.

Simulation run considering a Pd / $Ce_{0,33}Zr_{0,66}O_2$ catalysed monolith showed that combustion kinetics calculated from powdered catalyst samples overestimated greatly the performances of the same catalyst deposited on the walls of the micro combustor.

Simulations run with a vermiculite thermal conductibility taken from literature and only homogeneous combustion activated weren't able to stay lit like the real experimental monolith

After some trials however it was found that to reproduce the same behaviour of the experimental apparatus a vermiculite heat conduction value of 0,00025 W/mK had to be inserted.

This is a quite small value in apparent contrast with known literature so in the future will be mandatory to asses if the uncatalysed micro monolith works through heat recycling (as assumed during modelling) or acts just as a physical support for a free flame.

11 APPENDIX: CODES

Code for best fitting kinetic values determination :

The fitting of best kinetic values has always been an hard problem since most physically sound models such as Langmuir-Hinshelwood or Mars-van Krevelen cannot be written in a linear form.

For this reason, before computing power became significative, kinetics for engineering purposes were evaluated using the linearizable power law formulation:

$$R_{rate} = k_{\infty} * e^{\frac{-E}{RT}} * A^{m} * B^{n} \qquad (18)$$

Applying logarithms becomes:

$$\ln(R_{rate}) = \ln(k_{\infty}) + \frac{-E}{RT} + m * \ln(A) + n * \ln(B) \qquad (19)$$

Because R (universal gas constant) ,T , A and B are known parameters and because $\ln(k_{\infty})$ can be expressed as a single unknown it can be noted that transformed equation is linear and can be resolved by a deterministic method showed in any book about numerical calculus.

When this is not possible the fitting of the parameters leading to the least square error must be done by an iterative method estimating time by time parameter correction

Unfortunately the equation to solve looked like the Rosenbrock's function which is defined by:

$$f(x,y) = (1-x)^2 + 100(y-x^2)^2. \qquad (20)$$

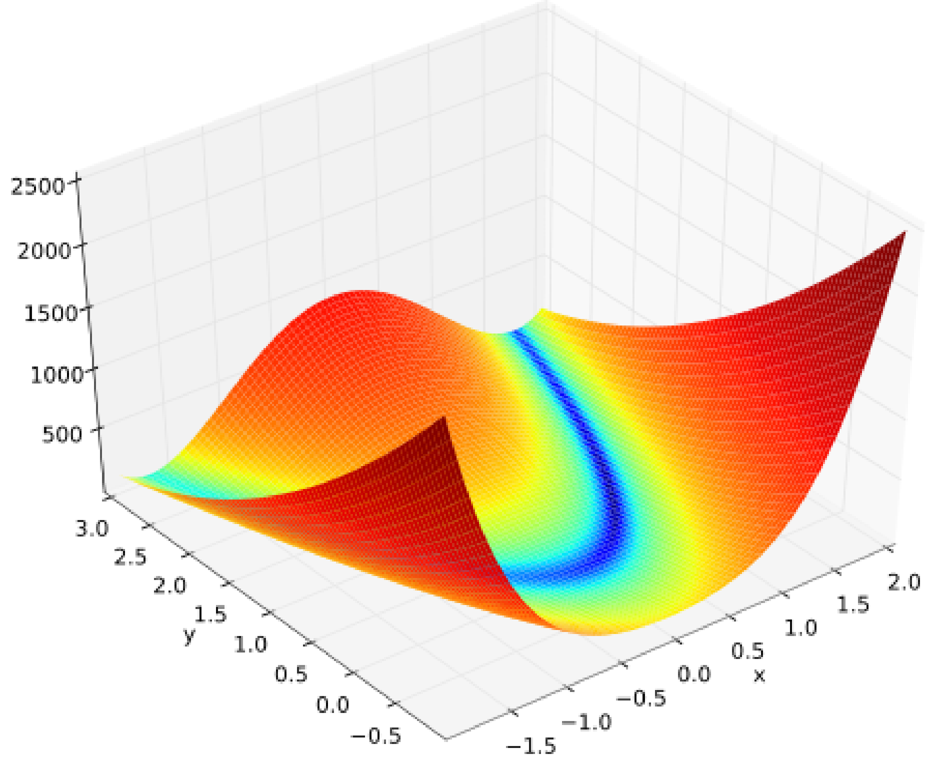

Figure 87: 3D plot of Rosenbrock's function

The global minimum is inside a long, narrow, parabolic shaped flat valley.

The standard, gradient-based, mathematical algorithms easily find a point inside the valley but, after that, the convergence to the global minimum, is difficult.

This happens because like in a true canyon a small gradient leads to the solution but in all other directions gradients are huge: this situation leads to the failure of every algorithm employing gradient calculation by finite differentiation.

This problem was easily spotted by launching a standard algorithm with starting different points observing that they converged every time in a different solution

For the fitting of the parameters so was elaborated a method employing random numbers to modify parameters little at time and confronting the results with the ones of the previous iteration: if the new parameters fitted better than the old ones they were accepted otherwise they were discarded

In order to assure that the kinetic constants remained in the R^+ domain, which is the only one that assures a physical sense to kinetics models, instead of simply summing a random number we operated this way:

$$k_{i+1} = k_i * (1 + P_{tuning} * rand) \tag{21}$$

P_{tuning} is a parameter that ranges between 0.01 and 0 and serves at tuning the searching field: it is recommended to start with a relatively large value and to decrease it when a minimum is identified or if the algorithm gets stuck inside a “canyon”.

Implementation of this algorithm has been done using Labview® software which allowed to dynamically see convergence behaviour and to correct P_{tuning} as needed.

Other Fluent parameters

Simulations were performed using the node based gradient calculation which offers better accuracy against an increase in computation time

In facts, φ_f can be computed by the arithmetic average of the nodal values on the face.

$$\overline{\phi}_f = \frac{1}{N_f} \sum_{n}^{N_f} \overline{\phi}_n \tag{22}$$

where N_f is the number of nodes on the face.

The nodal values, φ_n in Equation 21, are constructed from the weighted average of the cell values surrounding the nodes, following the approach originally proposed by Holmes and Connel [1] and Rauch et al. [2]. This scheme reconstructs exact values of a linear function at a node from surrounding cell-centered values on arbitrary unstructured meshes by solving a constrained minimization problem, preserving a second-order spatial accuracy.

The node-based averaging scheme is known to be more accurate than the default cell-based scheme for unstructured meshes, most notably for triangular and tetrahedral meshes.

Because the pressure gradients are small the standard pressure discretization coupling scheme proved to be effective.

The pressure-based solver algorithm

The pressure-based solver uses a solution algorithm where the governing equations are solved sequentially (i.e., segregated from each other). Because the governing equations are non-linear and coupled, the solution loop must be carried out iteratively in order to obtain a converged numerical solution.

Instead the segregated algorithm, the individual governing equations for the solution variables (e.g., *u, v, w, p, T, k, ε*, etc.) are solved one after the other. Each governing equation, while being solved, is "decoupled" or "segregated" from other equations, hence its name.

The segregated algorithm is memory-efficient, since the discretized equations need only to be stored in the memory one at a time. However, the solution convergence is relatively slow, inasmuch as the equations are solved in a decoupled manner.

With the segregated algorithm, each iteration consists of the steps illustrated in the left side of Figure 88 and outlined below:

1. Update fluid properties (e,g, density, viscosity, specific heat) including turbulent viscosity (diffusivity) based on the current solution.
2. Solve the momentum equations, one after the other, using the recently updated values of pressure and face mass fluxes.
3. Solve the pressure correction equation using the recently obtained velocity field and the mass-flux.
4. Correct face mass fluxes, pressure, and the velocity field using the pressure correction obtained from Step 3.
5. Solve the equations for additional scalars, if any, such as turbulent quantities, energy, species, and radiation intensity using the current values of the solution variables.
6. Update the source terms arising from the interactions among different phases (e.g., source term for the carrier phase due to discrete particles).
7. Check for the convergence of the equations.
8. These steps are continued until the convergence criteria are met.

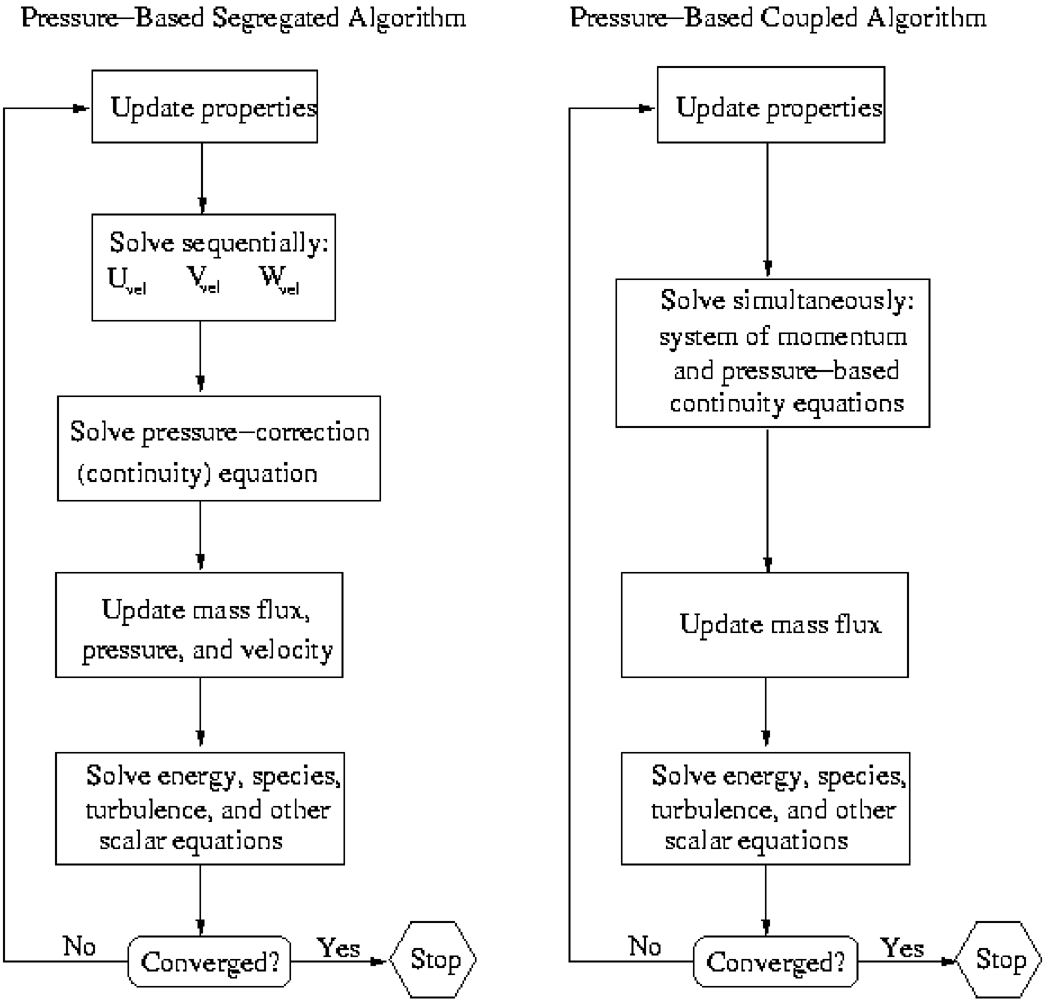

Figure 88: Overview of the Pressure-Based Solution Methods

Unlike the segregated algorithm described above, the pressure-based coupled algorithm (see right side of Figure 88) solves a coupled system of equations comprising the momentum equations and the pressure-based continuity equation. Thus, in the coupled algorithm, Steps 2 and 3 in the segregated solution algorithm are replaced by a single step in which the coupled system of equations are solved. The remaining equations are solved in a decoupled fashion as in the segregated algorithm.

Since the momentum and continuity equations are solved in a closely coupled manner, the rate of solution convergence significantly improves when compared to the segregated algorithm even if the time needed to calculate a single iteration is somewhat larger.

Moreover, the memory requirement increases by 1.5 - 2 times that of the segregated algorithm since the discrete system of all momentum and pressure-based continuity equations needs to be stored in the memory when solving for the velocity and pressure fields (rather than just a single equation, as is the case with the segregated algorithm).

However in run simulation the extra memory requirement was not a constrain thanks to the generous RAM amount of the 64 bit capable workstation used.

Appendix: udf code used to calculate catalytic reaction kinetic and radiative emissivity

```
#include "udf.h"
#include "mem.h"

/*Parametro kappa infinito:*/
#define KINFOX 23.1          /*OSSIGENO*/
#define KINFMET 0.357         /*METANO*/
#define KINFDISS 0.000212
 /*energie di dissociazione*/

#define EATOX 33800.0         /*OSSIGENO*/
#define EATMET 24400.0     /*METANO*/
#define EATDISS 8890.0



real arfunc( real k1, real enatt,real temp  )
{
 return k1*exp(-enatt*1000/(UNIVERSAL_GAS_CONSTANT*temp));
}
        DEFINE_SR_RATE(sleptrev,f,tf,r,my,yi,rr)
        {
#if !RPHOST
        int k;
            int n_spec=5;
    real moli[5];
    real molifrac[5];
    real molitot;
    real press;
    real tmpr;
    real met;
    real ox;
            real supp;
if (!strcmp(r->name, "reaction-1"))

            {
    molitot=0.0;
    for (k=0; k<n_spec; k++)
    {
        moli[k]=yi[k]/my[k];
        molitot +=moli[k];
    }
    for (k=0; k<n_spec; k++) molifrac[k]=moli[k]/molitot;
   press=F_P(f,tf);
            press /=101325.0;

    tmpr= F_T(f,tf);
    met= press* molifrac[0]*arfunc(KINFMET,EATMET,tmpr);
    ox= press* molifrac[1]*arfunc(KINFOX,EATOX,tmpr);
```

```
        supp=(met*ox/arfunc(KINFDISS,EATDISS,tmpr));

  *rr=0.022510355*(met*ox/(2.0*met+ox+supp)); /*costante di fitting*/
        }
#endif

      }

/* profilo di costante di irraggiamento*/
DEFINE_PROFILE(radg, t, i)
{
#if !RPHOST
        face_t f;
        real temper;
        real radio;
        begin_f_loop(f,t)
                {
                temper = F_T(f,t);
                radio = -0.0007*temper+1.1877;
                if (radio>0.95) radio = 0.95;
                if (radio<0.1) radio = 0.1;
                F_PROFILE(f,t,i) = radio;
                }
        end_f_loop(f,t)
#endif
    }
```

References for the Appendix

1. D. G. Holmes and S. D. Connell. *"Solution of the 2D Navier-Stokes Equations on Unstructured Adaptive Grids"* Presented at the AIAA 9th Computational Fluid Dynamics Conference, June, 1989.

2. R.D. Rauch, J.T. Batira, and N.T.Y. Yang. *"Spatial Adaption Procedures on Unstructured Meshes for Accurate Unsteady Aerodynamic Flow Computations."* Technical Report AIAA-91-1106, aiaa, 1991.